Abstract

Piezo-Brillouin Electro-Optomechanics with High-Overtone Bulk Acoustic Resonators

Taekwan Yoon

2023

Bulk acoustic resonators support robust, long-lived mechanical modes, capable of coupling to various quantum systems. In separate works, such devices have achieved strong coupling to both superconducting qubits, via piezoelectricity, and optical cavities, via Brillouin interactions.

In this thesis, we discuss piezoelectric and Brillouin interactions between phonons and microwave/optical photons, as well as microwave and bulk acoustic resonators that enable the interactions. Based on the understanding of these elements, we then present a novel hybrid microwave/optical platform that exploits resonantly enhanced Brillouin interactions and piezoelectric couplings to efficiently access phonons within a variety of bulk crystalline materials (quartz, CaF_2, Si, etc) using tunable microwave and optical cavities.

The high optical sensitivity and ability to apply large resonant microwave field in this system offer a new tool for probing anomalous electromechanical couplings, which we demonstrate by investigating (nominally-centrosymmetric) CaF_2 and revealing parasitic piezoelectricity of 83 am/V. Additionally, we attempt to probe electromechanical response in Si, where we are able to provide an upper bound to its parasitic piezoelectricity.

We further show how this device functions as a bidirectional electro-opto-mechanical transducer using a piezoelectric crystal, x-cut quartz, with transduction efficiency exceeding 10^{-8} and lay out a feasible path towards unity conversion efficiency. Such studies are important topics for emerging quantum technologies and highlight the

versatility of the new hybrid platform introduced in this thesis.

Piezo-Brillouin Electro-Optomechanics with High-Overtone Bulk Acoustic Resonators

A Dissertation
Presented to the Faculty of the Graduate School
of
Yale University
in Candidacy for the Degree of
Doctor of Philosophy

by
Taekwan Yoon

Dissertation Directors: Prof. Robert J. Schoelkopf, Prof. Peter T. Rakich

May 2023

Contents

Acknowledgments

This thesis is a summary of work done over the past seven years, which would not have been possible without the assistance and guidance of many people.

I would like to begin by expressing my sincerest gratitude to my co-advisors, Prof. Peter Rakich and Prof. Robert Schoelkopf. Rob, I am grateful for all the support you have given me during my time at Yale and for allowing me to freely pursue collaborative areas of study. Every time we have meetings, your insights have always inspired me in numerous ways and have forged me to think, question, and grow as a scientist. Peter, thank you for welcoming me as a part of the lab and enlightening me in the fields of optics and acoustics that I was previously ignorant of. I deeply appreciate you being mostly available when I need your guidance, having in-depth discussions on research, and sharing invaluable insights. With your kindness and thoughtfulness, you motivate me to become not only a better scientist but also a better person.

I would like to thank Prof. Leonid Glazman, Prof. Jack Harris, and Prof. Yiwen Chu for taking the time and effort to be on my dissertation committee, and for their teaching and mentorship over the years.

Not just me, but every person working on the 4^{th} floor of Becton owes a huge thanks to Luigi Frunzio, who not only has very interesting stories to tell every time we speak but also seems to have solutions for every problem we encounter in the lab. Without you, the entire 4^{th} floor Becton lab won't function properly. Thank you for always being willing to help, and being one of the most enthusiastic and passionate

people I have ever known.

It has been such an unexpected privilege and pleasure to work with multiple lab groups. I thank all the past and present RSL, Rakichlab, and qulab members that I had worked and interacted with: William Renninger, Freek Ruesink, David Mason, Hagai Diamandi, Prashanta Kharel, Eric Kittlaus, Nils Otterstrom, Shai Gertler, Royce Luo, Yishu Zhou, Naijun Jin, Margaret Pavlovich, Haotian Cheng, Yanni Dahmani, Yiwen Chu, Serge Rosenblum, Benjamin Chapman, Chan U Lei, Vijay Jain, Max Hays, Nick Frattini, Lev Krayzman, Christopher Wang, Jaya Venkatraman, Suhas Ganjam, Spencer Diamond, James Teoh, Alex Read, Neel Thakur, Parker Henry, and Kaicheng Li.

I especially want to thank Yiwen Chu, Prashanta Kharel, Vijay Jain, and David Mason, who were my mentors throughout my PhD. With their help, I was able to not only learn scientific knowledge but also become the scientist I am now.

Having an incredibly welcoming and supportive administrative staff: Giselle Maillet, Maria Rao, Nuch Graves, Theresa Evangeliste, Jessica Tefft, and Alex Bozzi always made coming to work more enjoyable and productive with all the free caffeine provided. I will miss the conversations we had over coffee/tea and am grateful for providing a sense of community and a morale boost to the whole Becton community.

I am very grateful to all of the collaborators I had during the years. Without the help of the cleanroom experts: Mike Power, Chris Tillinghast, Jim Agresta, Yong Sun, Sean Rinehart, and Kelly Woods, most of my fabrication work on acoustics would not have been possible. Without the help of the machine shop experts: Vincent Bernardo, Nicholas Bernardo, and Michael Nuzzo, who were willing to machine complicated designs with tricky materials that no other machine shops were open to trying, most of my cavity designs would not have been made into experiments. Through the hard work of an external collaborator, Liam Collins from oak ridge national lab, the results from some of my experiments were empowered as they gained much more context.

My experiences from researching back as an undergraduate still remain one of the most memorable moments in my life. I attribute my achievements in graduate school partly to the mentorship and lessons I learned as a college student in Schusterlab. Hence, I want to express gratitude to my undergraduate advisor, Prof. David Schuster, and the lab members who I still meet yearly in conferences and feel close connections to: David McKay, Alex Ruichao Ma, Srivatsan Chakram, Ge Yang, Ravi Naik, Gerwin Koolstra, Yao Lu, Nate Earnest, Clai Owens, Nelson Leung, Andrew Oriani, Victoria Norman, Sam Saskin, and Abigail Shearrow.

To my friends from New Haven and around the world: KyungDuk, Matt, Ryan, JD, Daryl, Amy, George, Andrew, Effy, Adam, Paul, Cesar, Jason, William, Larry, Arthur, 제형, 원주, 민수, and 현중, thank you for your friendships over the years

Finally, my supporting family, for providing me an opportunity to pursue my passion and always inspiring me to keep moving forwards. And Andi, thank you for your support and warm heart, making me feel at home anywhere we are together. I'm excited about our future together.

Chapter 1

Introduction

Mechanical resonators, in many different forms ranging from macroscopic to microscopic, are well-studied systems with a wide spectrum of applications from gravitational wave detection [1, 2] to consumer electronics to quantum applications. In particular, demonstrations of reaching the ground state of mechanical motion in micromechanical resonators [3–5], in addition to the emergence of quantum computing, have fueled many on-going efforts for using mechanical resonators as a quantum resource.

One example is an emerging subfield of circuit quantum acousto-dynamics (circuit QAD) [6] that studies hybrid systems with a mechanical resonator coupled to a superconducting qubit. In these systems, strong piezoelectric coupling between a mechanical resonator and a superconducting qubit has been shown, along with the creation of quantum states of mechanical motion and full quantum tomography of these states [7–9].

Another approach in using mechanical resonators as a quantum resource is to use them as a long-lived quantum memory element [10, 11]. Extremely long phonon lifetimes of over a second (Q-factor over 10^{10}) have been demonstrated in both optomechanical crystal (OMC) and nanostring-based acoustic resonators [12, 13]. Additionally, the slower speed of sound compared to that of light results in acoustic devices

that are more compact and scalable compared to their electromagnetic counterparts, which is a favorable trait for quantum memory devices.

Finally, the transduction of quantum information between the microwave and optical domain is a vital piece of technology in realizing a quantum network [14]. Mechanical vibrations are versatile in coupling to a variety of systems, which allows acoustic systems to efficiently mediate the conversion between optical and microwave domains. From this perspective, a wide range of mechanical resonator-based transducers are being explored.

One such system uses a mechanical membrane coupled through radiation pressure to a superconducting microwave resonator and a Fabry-Pérot optical cavity [15–17]. This system achieved the highest transduction efficiency (47%) for classical signals, with respectable added noise (3.2 photons), and even demonstrated integration with a superconducting qubit. Most effort in this design is put into working around a small transduction bandwidth and lowering the added noise, both a result of a low mechanical frequency ($\sim$MHz) of the membrane.

Another notable candidate for a phonon-based transducer is OMC-based devices [18–20]. Piezoelectric interaction between microwave and mechanical elements is combined with the well-studied OMC, leading to a direct conversion between microwave photons and phonons at GHz frequency which then detunes the optical field through photoelasticity and radiation pressure. With this transducer design, one can achieve low (< 1 photons) added noise due to the high mechanical frequency, and integration with superconducting qubits has been demonstrated. As OMCs are fabricated on-chip, they are usually made on the same chip as the microwave element (qubits), resulting in a scalable approach. However, this inevitably leads to complicated fabrication steps with low reliability and limited tunability of device parameters post-fabrication. Sufficient isolation of superconducting elements from the optical field, and efficient coupling in and out of the chip are additional challenges OMC-based

designs have to overcome.

Other phonon-mediated approaches utilize thin film acoustic resonators [21, 22] and bulk acoustic resonators [23]. Although it is out of the scope of this dissertation, it is important to note that many other paths towards transduction, besides phonon-mediated transduction, are being explored such as making use of magnons, rare-earth ions, and direct electro-optical (EO) coupling [24–26].

However, integrating acoustics with quantum circuits also comes with challenges. In order to fully harness the benefits of acoustics in quantum applications as listed so far in the introduction, the mechanical element has to be highly coherent, couple only to intended modes, and have features that are well understood. In reality, when a qubit is coupled to an acoustic element, there often exist unintended couplings to lossy acoustic modes or to a continuum of modes, resulting in acoustic radiation poisoning qubit lifetime. As a result, in devices integrating superconducting qubits with acoustic elements through piezoelectricity, qubit lifetimes can be up to two orders of magnitude lower than that of typical transmons [7, 8, 27–31]. There are works trying to understand these phenomena through coupling to a bath of lossy acoustic modes [32] and through observing qubit response in relation to controlled modifications of the acoustic density of states within substrates [33].

Even in superconducting qubits without coupling to an acoustic element, loss channel through acoustic radiation is potentially an important factor in understanding the fundamental limits of qubit lifetimes. Inversion symmetry of a crystal can be broken at the surface [34], defect sites [35], and under external stress [36,37], leading to piezoelectricity in non-piezoelectric materials. Several studies are done to understand the effects of such anomalous piezoelectricity in qubits [34, 38]. Moreover, the true nature of dielectric loss isn't fully understood. The energy lost due to dielectric loss is dissipated in the form of thermal radiation, which is equivalent to phonon radiation. Thus, exploring the unintended coupling between microwave and acoustics, possibly

due to anomalous piezoelectricity, may give us a hint towards understanding the nature of dielectric loss [39].

Anomalous piezoelectricity that can result in unintended electromechanical couplings is likely to be very weak, hence detecting such an effect may require an extremely sensitive phonon spectroscopy tool more sensitive than conventional means of piezo-detection. Mechanical resonators in the past have been utilized in sensitive sensing of forces [40], masses [41], and even a single electron spin [42]. In our implementation of phonon-sensing, we will harness the strong optomechanical coupling enabled through Brillouin scattering.

Brillouin interaction is a great candidate for sensitive phonon spectroscopy. It is a phase-matched optomechanical three-wave mixing process in a bulk medium, where an optical pump photon scatters off of an acoustic phonon through photoelasticity [43, 44]. Brillouin scattering has been used in applications such as optical amplifiers [45] and lasers [46], and has been demonstrated in a wide range of media, including liquids [47, 48], gases [49], crystalline materials [50], fibers [51], and on-chip devices [45, 46]. Since photoelastic coupling is ubiquitous, Brillouin scattering should theoretically be observable in all crystals. It is well established in high-overtone bulk acoustic resonators (HBAR) [52,53], which include bare wafers, making it highly compatible with the type of material required for qubit fabrications. Brillouin scattering in HBARs (any piece of wafer one wants to characterize can be considered an HBAR) also experiences minimal laser heating in the mechanical modes for transparent media due to the large volume-to-surface ratio and good thermal anchoring [54, 55]. A phase-matching condition that Brillouin interaction requires typically sets the acoustic frequency and the optical frequency shift in the microwave range, making it a natural interface between the microwave and optical domains. When combined with cavity-optomechanics, Brillouin interactions have been shown to be very sensitive to phonons [54, 55] by reaching high optomechanical cooperativities through optical

pump-induced parametric enhancement.

Brillouin optomechanical systems with HBARs are also good candidates for microwave-to-optical transduction. Several of the requirements for efficient transduction such as strong optomechanical coupling [54, 55] and strong electromechanical coupling to a superconducting qubit [7] have recently been demonstrated in systems incorporating an HBAR. Long acoustic lifetime [56], good thermal properties, efficient external optical couplings [54, 55], good optical mode matching [52], and ease of fabrication of HBARs [53] are additional advantages of such a system. However, combining electromechanical coupling with Brillouin optomechanical coupling has not yet been demonstrated.

1.1 Outline of this thesis

In this dissertation, we will present a novel piezo-Brillouin design simultaneously integrating piezoelectric and Brillouin interaction in a resonantly enhanced configuration constituted of a variety of bulk crystalline materials and tunable optical/microwave cavities. This platform paves the way for the use of Brillouin interaction and long-lived phonons for efficient microwave-to-optical transduction and sensitive material spectroscopy.

- In Chapter 2, we start by introducing Brillouin scattering theory in the context of coherent phonons, as we are mostly interested in working with relatively long-lived phonons at cryogenic temperatures. Using Hamiltonian formalism, we analyze the optomechanical coupling rate. Then we show how we measure this coupling rate in systems with an optical single-pass configuration and with a resonantly enhanced configuration utilizing an optical cavity. For the latter case, we perform an optomechanically induced transparency (OMIT) measurement.

- In Chapter 3, we lay out the framework for the piezoelectric effect in our systems.

We begin with deriving the piezoelectric coupling rate using a Hamiltonian framework. In particular, we discuss how the distribution of piezoelectricity - either throughout the bulk or concentrated on the surface - influences the coupling properties. In order to achieve coherent piezoelectric couplings between microwave photons and acoustic phonons, we consider coupling a 3D microwave cavity to an HBAR. We provide several design choices for 3D microwave cavities used. Furthermore, we discuss the situation where a superconducting qubit is made on a piezoelectric substrate, which leads to a piezoelectrically induced spontaneous radiation of a qubit. We provide a model based on Fermi's golden rule, through which piezo-limited qubit lifetime can be approximated.

- In Chapter 4, we focus on HBARs. We summarize the loss mechanisms in acoustic systems that are of relevance to our devices. Then, we describe the fabrication process of our on-chip HBAR devices based on prior works [53], and describe several notable observations. A list of some of the quartz and Si devices made along the course of this work is provided, along with a discussion about some of our findings that allowed further improvements of the devices.

- In Chapter 5, we introduce a novel hybrid cavity platform for piezo-Brillouin operation. This is a type of hybrid microwave/acoustic/optical cavity system that simultaneously harnesses HBAR-mediated optomechanical and piezoelectric interactions through a fully resonant operation. We walk through the experimental apparatus and characterize each of the elements. We also provide a theoretical background, called a state space model, for understanding the hybrid system. This work is based on reference [57].

- In Chapter 6, we demonstrate an application of our piezo-Brillouin platform as a highly sensitive piezo-sensor. With the ability to conduct precision spectroscopy of GHz phonons with single-quanta sensitivity, we present a detection

of anomalous piezoelectricity in CaF_2, which is beyond the detection limit of some of the other conventional piezo-detection schemes. We also show an intermediary result in Si, providing a bound in possible anomalous piezoelectricity. The development of such a material characterization tool is of importance in material science as it allows further evaluation of substrate purity, solid-state defects, and surface properties. Moreover, in relation to quantum technologies, it can provide insight into the fundamental limits of qubit lifetimes and explain the possible origins of dielectric loss. This work is based on reference [57].

- In Chapter 7, we explore the hybrid piezo-Brillouin platform from the perspective of quantum transduction, which is a key quantum information technology enabling quantum network/internet. Several properties of our hybrid system, including high (~ 0.5) microwave and optical coupling efficiencies, optomechanical cooperativity exceeding 1, a wide frequency tuning range as a result of its modular design, and robust thermal properties, are key advantages when adapting the system into a quantum transducer. We demonstrate a transduction efficiency of our hybrid system comparable to other piezo-optomechanical systems, with a feasible optimization path towards unity efficiency. This work is based on reference [57].

Chapter 2

Brillouin scattering theory

2.1 Introduction

After the initial discussion of inelastic light scattering by Lord Rayleigh, Larmor, and Raman [58–60], Brillouin scattering was first proposed theoretically by Brillouin in 1922 [43] and separately by Mandelstam in 1926 [61]. Then it was experimentally verified in organic liquids in 1930 [47]. During this time, spontaneous Brillouin scattering was observed, which is an interaction where incident light scatters off thermal phonons.

The invention of the ruby laser in 1960 [44] providing a bright, coherent light source, was a remarkable feat enabling numerous scientific experiments that were previously impossible. Studies in Brillouin scattering also benefited from this invention, such as the first experimental demonstration of stimulated Brillouin scattering (SBS) in quartz and sapphire by Chiao, Townes, and Stoiche in 1964 [50]. Further discoveries of SBS in liquids [48] and gas [49] soon followed. Unlike spontaneous Brillouin scattering, SBS occurs when incident lasers electrostrictively drive phonons, which then scatter light to a shifted frequency.

Immediately after optical fibers were developed, it was noticed that SBS can set

a limit to the optical power handling capabilities of optical fibers. The longer the light travels in fiber, the stronger the light-sound interaction, leading to a depletion of the optical signal and a massive back reflection. Indeed, SBS in fibers was soon observed [51], and so were the limits in optical power handling of optical fibers [62,63]. Suppressing SBS in optical fibers is an active area of research still in these days [64,65].

Brillouin interaction has also been explored in integrated circuits [66]. Optical components utilizing Brillouin-active integrated photonic circuits include lasers [46], amplifiers [45], notch filters [67], acousto-optic modulators, isolators [68], and many more. More of the history and insightful perspectives of Brillouin scattering can be found in Ref. [69], and applications in Ref. [66, 70]

Brillouin scattering is a type of inelastic scattering of light, where optical waves photoelastically scatter off acoustic waves in a medium, Doppler-shifting the frequencies of the optical waves. In other words, it is a three-wave mixing process between optical and acoustic waves. It is analogous to another type of inelastic light scattering, Raman scattering, where light scatters off optical phonons. The difference is that Brillouin scattering results in a frequency shift in the order of 10s of GHz, while Raman scattering results in that of 10s of THz.

Conventionally, applications of Brillouin scattering are based on SBS. In SBS, one provides a pump and a probe light to drive acoustic waves, which then scatter the pump light into the probe light, thus resulting in a stimulated process. For our purposes, we will instead consider a spontaneous process. This is a process in which there is no optical probe. In the absence of an optical probe, phonons are no longer driven optically. Instead, we will allow another mechanism, such as electromechanical coupling, to drive phonons in the system. In this chapter, we will explain the Brillouin optomechanical process through which we read out phonons from our system, whereas the electromechanical process that drives phonons will be introduced in the following chapter.

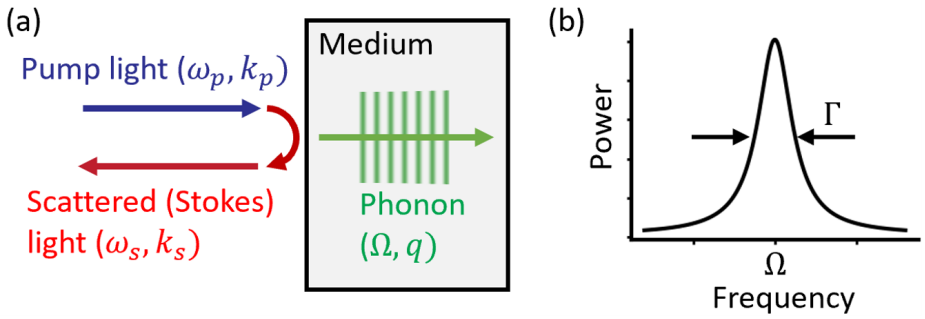

Figure 2.1: **Sketch of Brillouin scattering** (a) In an acoustic medium, a strain field creates a refractive index modulation through a photoelastic effect. Propagation of this pattern acts as a moving Bragg mirror, Doppler shifting the incident pump light field. Illustrated in the figure is a Stokes process, where the pump light is scattered into a lower-frequency light. (b) Power spectrum of the scattered signal has a characteristic Lorentzian lineshape with linewidth Γ at frequency Ω detuned from the pump.

2.2 Brillouin frequency

Throughout the thesis, we focus on optomechanical Brillouin interaction between standing wave phonons and photons. To get a basic understanding of phase matching and energy conservation considerations that determine the frequency where the optomechanical coupling occurs, it is useful to step back and view the interactions as a continuous system with traveling wave phonons. Additionally, we only consider backward Brillouin scattering that involves counter-propagating waves to maximize the optomechanical interaction length. As Brillouin scattering is a phase-matching interaction, it occurs around a set frequency determined by the material properties of the system in consideration. This frequency is called Brillouin frequency.

In an acoustic medium, strain fields (acoustic waves) can create a periodic variation in the refractive index of the material through photoelasticity. This acts as a Bragg mirror to the incoming light field, propagating at the acoustic velocity of the medium in forward and backward directions. The frequency of the reflected light is then Doppler-shifted, given as,

$$\Delta\omega = \pm\frac{2v_{\mathrm{m}}}{c/n}\omega_0, \tag{2.1}$$

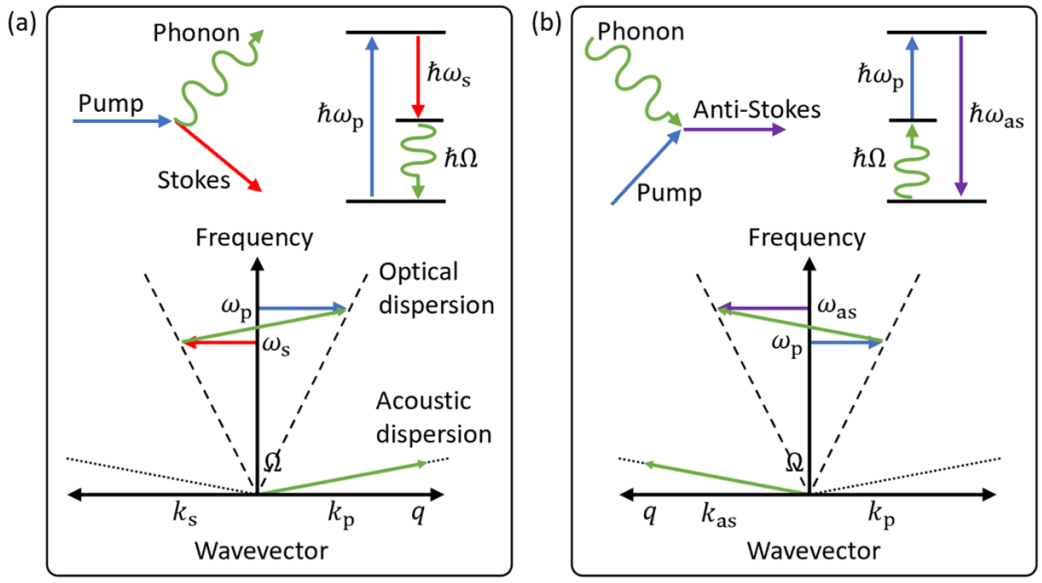

Figure 2.2: **Phase matching and energy conservation conditions for Brillouin scattering.** Illustrations of (a) Stokes scattering and (b) anti-Stokes scattering. Within each of the boxes, the top left figure is a particle analogy where (Stokes process) pump photon is annihilated to create a Stokes photon and a phonon or (anti-Stokes process) pump photon absorbs a phonon to create an anti-Stokes photon. The top right figure shows the energy conservation condition. The bottom figure describes optical and acoustic linear dispersion diagrams and the corresponding phase-matching conditions.

where ω_0 is the initial light frequency, v_m is the acoustic velocity, and n is the refractive index of the medium. Redshift of light ($\Delta\omega$ with a negative sign) occurs when light scatters off a sound wave propagating in the same direction as the light, while blueshift ($\Delta\omega$ with a positive sign) occurs when light scatters off a sound wave propagating in the opposite direction. The former is referred to as a Stokes process, and the latter an anti-Stokes process. See figure 2.1(a) for a simplified illustration of the Stokes process occurring inside an acoustic medium.

Alternatively, Brillouin scattering can also be understood as a phase-matched three-wave mixing process between optical photons and acoustic phonons (figure 2.2). A forward propagating optical pump photon with frequency ω_p and wavevector k_p can scatter into a forward propagating phonon $(\Omega_\mathrm{s}, q_\mathrm{s})$ and a backward propagating Stokes photon $(\omega_\mathrm{s}, k_\mathrm{s})$. In the case of the anti-Stokes process, a forward propagating

optical pump photon absorbs a backward propagating phonon ($\Omega_{\rm as}, q_{\rm as}$) and becomes a backward propagating anti-Stokes photon ($\omega_{\rm as}, k_{\rm as}$). Both processes have to satisfy energy conservation and phase-matching requirements. For the Stokes process, such requirements are,

$$\begin{aligned} \hbar\omega_{\rm p} &= \hbar\Omega_{\rm s} + \hbar\omega_{\rm s} \\ k_{\rm p} &= q_{\rm s} - k_{\rm s}, \end{aligned} \tag{2.2}$$

Meanwhile, the phase matching and energy conservation requirements in the anti-Stokes process are,

$$\begin{aligned} \hbar\omega_{\rm p} + \hbar\Omega_{\rm as} &= \hbar\omega_{\rm as} \\ k_{\rm p} - q_{\rm as} &= -k_{\rm as}. \end{aligned} \tag{2.3}$$

Note that the phase-matching condition implies that the acoustic wavelength should approximately match half of the optical wavelength in the medium. Combining the phase-matching and energy conservation conditions with the assumed linear dispersion relation $\omega = (c/n)k$ ($\Omega = v_{\rm m}q$) of optical (acoustic) waves, we can obtain the required frequencies of phonons for Stokes process where $c/n \gg v_{\rm m}$,

$$\frac{\omega_{\rm p}}{c/n} = \frac{\Omega_{\rm s}}{v_{\rm m}} - \frac{\omega_{\rm p} - \Omega_{\rm s}}{c/n} \tag{2.4}$$

$$\Omega_{\rm s} = \frac{2\omega_{\rm p}}{\frac{c/n}{v_{\rm m}} + 1} \sim \frac{2\omega_{\rm p} v_{\rm m}}{c/n}, \tag{2.5}$$

while for anti-Stokes process, where $c/n \gg v_{\rm m}$,

$$\frac{\omega_{\rm p}}{c/n} - \frac{\Omega_{\rm as}}{v_{\rm m}} = -\frac{\omega_{\rm p} + \Omega_{\rm as}}{c/n} \tag{2.6}$$

$$\Omega_{\rm as} = \frac{2\omega_{\rm p}}{\frac{c/n}{v_m} - 1} \sim \frac{2\omega_{\rm p} v_{\rm m}}{c/n}. \tag{2.7}$$

The frequency given in equations 2.1, 2.5 and 2.7 is the same ($\omega_0 = \omega_{\rm p}$), and is defined as Brillouin frequency ($\Omega_{\rm B}$). Note that the ± 1 in the denominator of equations

2.5 and 2.7 can play a role in distinguishing Stokes and anti-Stokes process through dispersive symmetry breaking [52]. Typically in a crystal, the Brillouin frequency is in the range of 10∼50 GHz.

2.3 Brillouin scattering from standing wave phonons

At room temperature, acoustic phonons have low spatial coherence in the range of Brillouin frequency previously discussed (see chapter 4 for discussions on sources of dissipation). In this case, phonons in a heavily damped medium can be represented as traveling waves. At low temperatures on the other hand, phonons in crystalline substrates can have extremely long lifetimes with appropriate designs and optical acoustic mode engineering [12, 13, 56]. In the optomechanical systems we study, it is advantageous to harness this long acoustic coherence, as it significantly extends the optomechanical interaction length. With long coherences, phonons reflect from the boundaries of a mm-scale resonator, creating well-defined and discrete macroscopic phonon modes. In the limit where a mechanical response is no longer local, we have to treat phonon modes as standing wave cavity modes, leading to a non-conventional expression for the interaction. In particular, we need to characterize the optomechanical coupling rate and cooperativity.

In this section, we first consider the integration of an optical cavity with an acoustic cavity with standing wave phonon modes to further enhance the Brillouin optomechanical response. We treat the system from the perspective of cavity optomechanics to characterize the coupling properties. Then, we make appropriate modifications to understand the single-pass case, where there is no optical cavity, making the light field pass through the crystal and interact with the acoustic field only once.

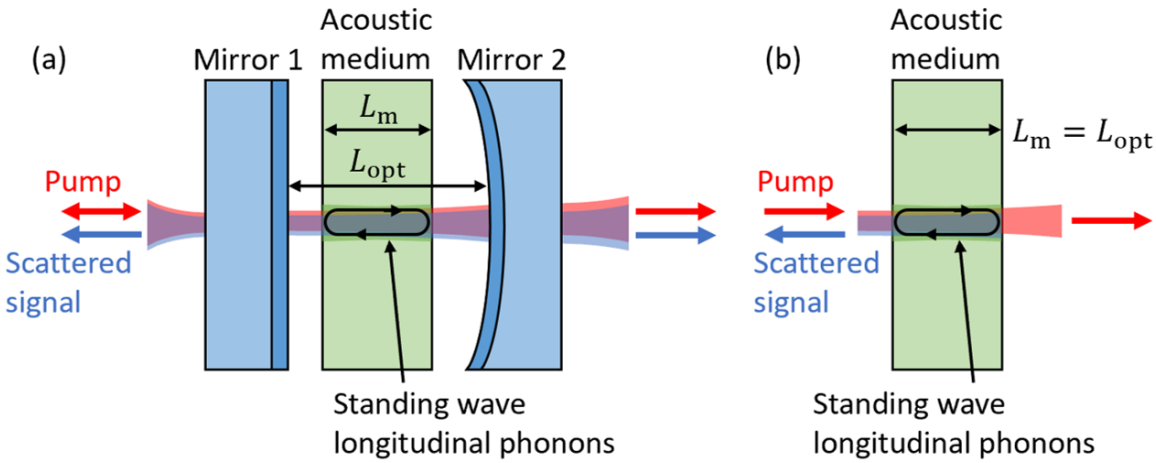

Figure 2.3: **Sketch of cavity optomechanics with Brillouin interaction** At low temperatures, phonons form standing wave modes inside a bulk acoustic medium. Note that the figure illustrates the case shown in section 2.3, where anti-Stokes interaction is considered, thus the scattered signal (blue) is blue-shifted from the pump (red). (a) The interaction between acoustic modes and light can be enhanced by placing an optical cavity around the acoustic substrate. In the figure, we consider a Fabry-Pérot optical cavity with dielectric mirrors. The pump enters from the left side and both the pump and the scattered signal exit from both sides of the optical cavity. (b) Illustration for the single-pass case without an optical cavity. Due to the low reflection of light at the dielectric surface, we can assume that the light only makes a single pass through the substrate, hence achieving lower interaction compared to the case in (a).

2.3.1 Cavity optomechanical coupling rate

Here, we derive the Brillouin optomechanical coupling rate, closely following prior studies [52, 54]. Specifically, we consider a phase-matched photoelastic coupling between optical Fabry-Pérot modes and longitudinal bulk acoustic resonances (see figure 2.3a). The electric field profile of the j-th optical cavity mode is given by

$$E_j(r,z,t) = E_{j,0} e^{-r^2/r_{\mathrm{opt}}^2} \sin(k_j z)(a_j(t) + a_j^\dagger(t)) \tag{2.8}$$

where $E_{j,0}$ is the zero-point field, r_{opt} is the optical mode waist, k_j is j-th optical wavevector, a_j is the annihilation operator for j-th optical mode, and sin term is from the boundary condition. Note that for simplicity, this model neglects modifications

of the optical field due to the combined vacuum/dielectric composition of the cavity. Full modeling of the optical mode profile, in the presence of this dielectric interface, is possible through use of a transfer matrix model [54]. The zero-point field, $E_{j,0}$, can be obtained from the normalization of electromagnetic fields in the ground state,

$$\int \frac{\epsilon_0 \epsilon_r E_j^2}{2} dV + \int \frac{B_j^2}{2\mu_0 \mu_r} dV = \frac{\hbar \omega_j}{2}, \tag{2.9}$$

where B_j is the magnetic field profile of the j-th optical cavity mode, ω_j is the j-th optical cavity mode frequency, ϵ_0 (ϵ_r) is vacuum (relative) permittivity, and μ_0 (μ_r) is vacuum (relative) permeability. Since the energy is equally distributed between electric and magnetic fields, we have,

$$\int \frac{\epsilon_0 \epsilon_r E_j^2}{2} dV = \frac{\hbar \omega_j}{4}. \tag{2.10}$$

Substituting electric field profile (E_j) from equation 2.8,

$$\begin{aligned} &\frac{\epsilon_0 \epsilon_r E_{j,0}^2}{2} \int e^{-2r^2/r_{\text{opt}}^2} dA \int \sin^2(k_j z) dz \\ &= \frac{\epsilon_0 \epsilon_r E_{j,0}^2}{2} \left(\frac{\pi r_{\text{opt}}^2}{2} \right) \left(\frac{L_{\text{opt}}}{2} \right) \\ &= \frac{\hbar \omega_j}{4}, \end{aligned} \tag{2.11}$$

where L_{opt} is optical cavity length. Thus, we obtain the zero-point field, $E_{j,0}$,

$$E_{j,0} = \sqrt{\frac{2\hbar\omega_j}{\epsilon_0 \epsilon_r \pi r_{\text{opt}}^2 L_{\text{opt}}}} = \sqrt{\frac{2\hbar\omega_j}{\epsilon_0 \epsilon_r A_{\text{opt}} L_{\text{opt}}}}, \tag{2.12}$$

where $A_{\text{opt}} = \pi r_{\text{opt}}^2$ is optical mode area.

As for the acoustic modes of an HBAR, we can write the displacement of the i-th

longitudinal mode,

$$U_i(r,z,t) = U_{i,0} e^{-r^2/r_{\mathrm{m}}^2} \cos(q_i z)(b_i(t) + b_i^\dagger(t)), \tag{2.13}$$

where $U_{i,0}$ is the zero-point displacement, r_{m} is the acoustic mode waist, q_i is i-th acoustic wavevector, b_i is the annihilation operator for i-th acoustic mode, and cos term is from the boundary condition of strain fields. We assume that the crystal begins precisely at $z = 0$ (i.e. coincident with the mirror). The zero-point displacement, $U_{i,0}$, can be obtained from the normalization of acoustic energy in the ground state,

$$\frac{1}{2}\int \left(\rho \dot{U_i}^2 + \rho v_{\mathrm{m}}^2 \left(\frac{\partial U_i}{\partial z} \right)^2 \right) dV = \frac{\hbar \Omega_{\mathrm{m}}}{2}, \tag{2.14}$$

where ρ is the crystal density and Ω_{m} is the i^{th} acoustic mode frequency (note that index i is omitted for simplicity). Assuming energy is equally distributed between the kinetic energy and the potential energy, let us re-write the relation in terms of the potential energy,

$$\frac{1}{2}\int \rho v_{\mathrm{m}}^2 \left(\frac{\partial U_i}{\partial z} \right)^2 dV = \frac{\hbar \Omega_{\mathrm{m}}}{4}. \tag{2.15}$$

From equation 2.13, above relation becomes,

$$\begin{aligned} &\frac{1}{2}\rho v_{\mathrm{m}}^2 q_i^2 U_{i,0}^2 \int e^{-2r^2/r_{\mathrm{m}}^2} dA \int \sin^2(q_i z) dz \\ &= \frac{1}{2}\rho v_{\mathrm{m}}^2 q_i^2 U_{i,0}^2 \left(\frac{\pi r_{\mathrm{m}}^2}{2} \right) \left(\frac{L_{\mathrm{m}}}{2} \right) \\ &= \frac{\hbar \Omega_{\mathrm{m}}}{4}, \end{aligned} \tag{2.16}$$

where L_{m} is the acoustic cavity length (crystal thickness). Solving for the zero-point displacement, we get,

$$U_{i,0} = \sqrt{\frac{2\hbar}{\rho \Omega_{\mathrm{m}} \pi r_{\mathrm{m}}^2 L_{\mathrm{m}}}} = \sqrt{\frac{2\hbar}{\rho \Omega_{\mathrm{m}} A_{\mathrm{m}} L_{\mathrm{m}}}}, \tag{2.17}$$

where $A_{\mathrm{m}} = \pi r_{\mathrm{m}}^2$ is acoustic mode area.

Assuming we are using a flat-flat (as opposed to plano-convex) crystal for the acoustic resonator, our acoustic mode waist is not independently determined by the crystal geometry, but rather defined by the optical mode waist. Specifically, $r_{\mathrm{m}} = r_{\mathrm{opt}}/\sqrt{2}$, so that $A_{\mathrm{m}} = A_{\mathrm{opt}}/2$.

The photoelastic interaction Hamiltonian is given by

$$H_{\mathrm{int}} = \frac{1}{2}\epsilon_0 \epsilon_r^2 p_{13} \int \left(\frac{\partial U_i}{\partial z}\right) E_j E_{j+1} dV, \tag{2.18}$$

where p_{13} is the relevant photoelastic constant. In anticipation of the phase-matching requirement from light and acoustic fields having parallel wavevectors, we will consider intermodal coupling involving the j and $j+1$ optical modes with wavevectors/frequencies which satisfy $q_i = k_{j+1} + k_j \approx 2k_j$ and $\Omega_{\mathrm{m}} = \omega_{j+1} - \omega_j$. This yields the Brillouin phase-matching condition from before ($q_i = 2n\omega_j/c$). Plugging in the appropriate mode definitions from equations 2.8 and 2.13, and making the rotating wave approximation, the interaction Hamiltonian becomes,

$$\begin{aligned} H_{\mathrm{int}} = \frac{1}{2}\epsilon_0 \epsilon_r^2 p_{13} \int dV\, q_i U_{i,0} E_{j+1,0} E_{j,0} e^{-\frac{r^2}{r_{\mathrm{m}}^2}} e^{-\frac{r^2}{r_{\mathrm{opt}}^2}} e^{-\frac{r^2}{r_{\mathrm{opt}}^2}} \\ \sin(q_i z)\sin(k_{j+1} z)\sin(k_j z)(a_{j+1}^\dagger a_j b_i + H.C.). \end{aligned} \tag{2.19}$$

Although we have assumed that the crystal begins precisely at $z = 0$ (i.e. coincident with the mirror), in reality, the longitudinal component of this overlap integral will depend sensitively on the position of the acoustic standing wave within the optical standing wave. Additionally, we are neglecting the transverse spatial variation in both optical and acoustic modes inside the crystal, treating them as uniform Gaussian modes over the interaction length of a chip. These approximations, as well as the choice to neglect optical field redistribution due to the dielectric interface, constitute the main sources of uncertainty in predicting the cavity optomechanical coupling rate.

However, as shown in [54], the approach we take here offers a good estimate of the maximum possible coupling rate.

The interaction Hamiltonian can be alternatively written in terms of the single-photon coupling rate, $g_{\mathrm{om},0}$, as follows,

$$H_{\mathrm{int}} = \hbar g_{\mathrm{om},0}(a_{j+1}^{\dagger} a_j b_i + H.C.). \tag{2.20}$$

Combining Equation 2.19 and 2.20, we obtain the single-photon coupling rate in the presence of an optical cavity,

$$\begin{aligned}\hbar g_{\mathrm{om},0} = \frac{1}{2}\epsilon_0 \epsilon_r^2 p_{13} \int dV q_i U_{i,0} E_{j+1,0} E_{j,0} e^{-\frac{r^2}{r_{\mathrm{m}}^2}} e^{-\frac{r^2}{r_{\mathrm{opt}}^2}} e^{-\frac{r^2}{r_{\mathrm{opt}}^2}} \\ \sin(q_i z)\sin(k_{j+1} z)\sin(k_j z),\end{aligned} \tag{2.21}$$

$$g_{\mathrm{om},0} = \frac{\omega_j^2 n^3 p_{13}}{2c}\sqrt{\frac{\hbar}{\Omega_{\mathrm{m}} \rho A_{\mathrm{m}} L_{\mathrm{m}}}}\frac{L_{\mathrm{m}}}{L_{\mathrm{opt}}}, \tag{2.22}$$

where optomechanical mode-matching condition ($r_{\mathrm{m}} = r_{\mathrm{opt}}/\sqrt{2}$) and parallel optical/acoustic wavevectors are assumed to maximize the coupling rate. Note that $g_{\mathrm{om},0}$ is given within the acoustic substrate ($0 < z < L_{\mathrm{m}}$) and becomes 0 outside of the range.

Within an optical cavity, it is conventional to consider the cavity-enhanced coupling rate with a strong optical pump, provided the pump laser can be approximated as a pure coherent state. This is a well-established method to boost the coupling rate in systems, as long as the systems can handle high optical pump power and the added thermal noise is negligible. Referring back to the interaction Hamiltonian (equation 2.20), the expression can be linearized around a strong pump (j-th optical mode is the pump mode). Assuming that our optical pump is a perfect coherent state, we can replace a_j with α, where α has a magnitude $\sqrt{N_{\mathrm{p}}}$, N_{p} being the inter-cavity pump

photon number.

$$\begin{aligned} H_{\text{int}} &= \hbar g_{\text{om},0} a_{j+1}^{\dagger} a_j b_i \\ &\approx \hbar \sqrt{N_p} g_{\text{om},0} a_{j+1}^{\dagger} b_i \\ &= \hbar g_{\text{om}} a_{j+1}^{\dagger} b_i \end{aligned} \tag{2.23}$$

$$g_{\text{om}} = \sqrt{N_{\text{p}}} g_{\text{om},0}, \tag{2.24}$$

where g_{om} is the photon number-enhanced optomechanical coupling rate.

Another important metric in optomechanical interactions is the optomechanical cooperativity (C_{om}) [71]. It compares the optomechanical coupling rate to the dissipation rates of photons and phonons, and it is given as,

$$C_{\text{om}} = \frac{4 g_{\text{om}}^2}{\kappa_{\text{opt}} \Gamma}, \tag{2.25}$$

where κ_{opt} (Γ) is the dissipation rate of optical (acoustic) mode. Similarly, single-photon optomechanical cooperativity is expressed using single-photon optomechanical coupling rate ($C_{\text{om},0} = \frac{4 g_{\text{om},0}^2}{\kappa_{\text{opt}} \Gamma} = \frac{C_{\text{om}}}{N}$).

2.3.2 Single-pass optomechanical coupling rate

When we want to study phonon modes of acoustic resonators (e.g. for acoustic mode or material spectroscopy), it is useful to eliminate the complexity associated with the optical resonator. In this case, which we hereafter label as single-pass or free-space configuration, we might like to shine a laser beam through an acoustic resonator and observe the Brillouin scattering to characterize the phonon modes.

The Brillouin optomechanical coupling rate in the cavity optomechanics case (equation 2.22) can be modified to understand the single-pass case, where Brillouin optomechanical coupling occurs between traveling light waves and acoustic cavity modes (see figure 2.3b). Here, the effective optical cavity becomes the crystal, result-

ing in $L_{\mathrm{opt}} = L_{\mathrm{m}}$, and the corresponding coupling rate,

$$g'_{\mathrm{om},0} = \frac{\omega_j^2 n^3 p_{13}}{2c}\sqrt{\frac{\hbar}{\Omega_{\mathrm{m}}\rho A_{\mathrm{m}} L_{\mathrm{m}}}}. \tag{2.26}$$

Compared to equation 2.22, filling-factor term ($\frac{L_{\mathrm{m}}}{L_{\mathrm{opt}}} = 1$) is removed.

Free-space cooperativity of an optomechanical system with an acoustic cavity and without an optical cavity is defined in reference [52] as,

$$C_{\mathrm{om}}^{\mathrm{sp}} = \frac{P_{\mathrm{p}}}{\hbar\omega_{\mathrm{p}}}\frac{L_{\mathrm{m}}}{v_{\mathrm{g,p}}}\frac{L_{\mathrm{m}}}{v_{\mathrm{g,s}}}\frac{g'^2_{\mathrm{om},0}}{\Gamma}, \tag{2.27}$$

where P_{p} is the optical pump power and $v_{\mathrm{g,p}}$ ($v_{\mathrm{g,s}}$) is the group velocity of the pump (signal) light. Introducing group delay ($\tau = L_{\mathrm{m}} n/c$), and single-pass photon number ($N'_{\mathrm{p}} = P_{\mathrm{p}} L_{\mathrm{m}}/(\hbar\omega_{\mathrm{p}} v_{\mathrm{g,p}})$), the single-pass cooperativity can be re-written in a simpler form,

$$C_{\mathrm{om}}^{\mathrm{sp}} = \frac{g'^2_{\mathrm{om}}}{\Gamma\tau^{-1}}, \tag{2.28}$$

where $g'_{\mathrm{om}} = \sqrt{N'_{\mathrm{p}}}\, g'_{\mathrm{om},0}$.

2.4 Measurement of optomechanical coupling

2.4.1 Optomechanically induced transparancy (OMIT)

In cavity optomechanics, OMIT provides a convenient way of characterizing the optomechanical coupling rate and cooperativity [72]. OMIT is valuable since it allows the identification of optomechanical coupling rate and cooperativity by analytically solving a simple power dependant response with a minimum of fitting parameters. In our system, we have a Fabry-Pérot optical cavity with an HBAR between the mirrors. We first choose a pair of optical modes with mode spacing matching the Brillouin frequency of the HBAR crystal. We then send the pump/probe light into

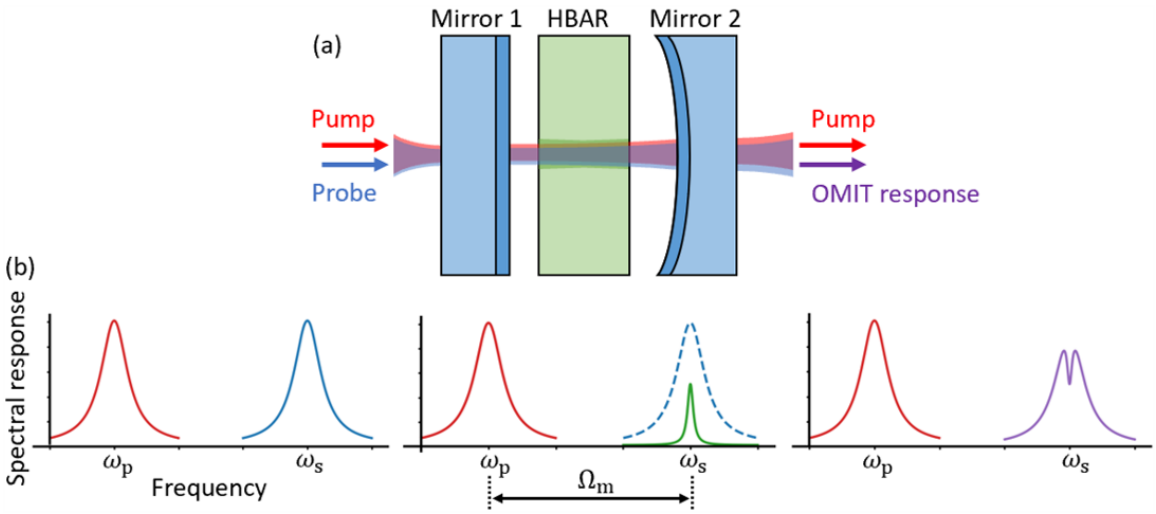

Figure 2.4: **Optomechanically induced transparency (OMIT) in an optical Fabry-Pérot / HBAR system** (a) Illustration of a setup with an optical Fabry-Pérot combined with an HBAR. The optical Fabry-Pérot cavity consists of two mirrors (mirror 1 and mirror 2). The pump tone and probe tone injected into the system are indicated as shaded red and blue. Driven phonon modes are shown as shaded green. (b) (From left to right) The transmission spectrum of pump mode at ω_p and probe mode at ω_s of an optical cavity are shown in red and blue. In the presence of driven phonons at $\Omega_m = \omega_s - \omega_p$, the pump is scattered into a sideband indicated in green. The probe mode interferes with this sideband, resulting in an OMIT response in purple.

the pair of optical modes, which electrostrictively drive phonons inside the HBAR. The driven phonons photoelastically scatter the optical pump, creating a sideband near the probe mode. This photoelastically-driven motional sideband optically interferes with the probe mode, modifying the spectral feature of the detected probe spectrum (see figure 2.4). Note that OMIT, characterized by a spectral dip in the detected spectrum, is observed in the anti-Stokes scattering process, whereas optomechanically induced amplification (OMIA), characterized by a sharp spectral peak, is observed in the Stokes process.

In order to understand the spectral features of OMIT, we will start from the Hamiltonian of an optomechanical system, given as,

$$H = \hbar\omega_p a_p^\dagger a_p + \hbar\omega_s a_s^\dagger a_s + \hbar\Omega_m b^\dagger b + \hbar g_{om,0}(a_p^\dagger a_s b^\dagger + a_p a_s^\dagger b), \tag{2.29}$$

where a_{p} is the annihilation operator for optical pump mode, a_{s} is the annihilation operator for optical probe (signal) mode, b is the annihilation operator for acoustic mode, and ω_{s} is the frequency of optical probe (signal) mode. By rotating in the frame of $H_0 = \hbar\omega_{\mathrm{p}} a_{\mathrm{p}}^{\dagger} a_{\mathrm{p}} + \hbar\omega_{\mathrm{p}} a_{\mathrm{s}}^{\dagger} a_{\mathrm{s}}$ and by linearizing around an undepleted pump, we obtain an effective Hamiltonian,

$$H_{\mathrm{eff}} = \hbar\Delta_{\mathrm{opt}} a^{\dagger} a + \hbar\Omega_{\mathrm{m}} b^{\dagger} b + \hbar g_{\mathrm{om}} (a b^{\dagger} + a^{\dagger} b), \tag{2.30}$$

where $\Delta_{\mathrm{opt}} = \omega_{\mathrm{s}} - \omega_{\mathrm{p}}$ and $a = a_{\mathrm{s}}$ for convenience. The Heisenberg equations of motions from this Hamiltonian are,

$$\begin{aligned} \dot{a} &= (-i\Delta_{\mathrm{opt}} - \frac{\kappa_{\mathrm{opt}}}{2}) a - i g_{\mathrm{om}} b + \sqrt{\kappa_{\mathrm{opt,c}}} a_{\mathrm{in}} \\ \dot{b} &= (-i\Omega_{\mathrm{m}} - \frac{\Gamma}{2}) b - i g_{\mathrm{om}} a, \end{aligned} \tag{2.31}$$

where $\kappa_{\mathrm{opt,c}}$ is the optical cavity coupling rate and a_{in} is the external input field ($P_{\mathrm{in}}/\hbar\omega_{\mathrm{s}} = \langle a_{\mathrm{in}}^{\dagger} a_{\mathrm{in}} \rangle$). Solving the equations of motions in the frequency domain,

$$a(\Omega) = \frac{-\sqrt{\kappa_{\mathrm{opt,c}}} a_{\mathrm{in}}}{i(\Omega - \Delta_{\mathrm{opt}}) - \frac{\kappa_{\mathrm{opt}}}{2} + \frac{g_{\mathrm{om}}^2}{(i(\Omega - \Omega_{\mathrm{m}}) - \frac{\Gamma}{2})}}. \tag{2.32}$$

Note that Ω is the probe light frequency in the rotating frame ($\Omega = \omega_l - \omega_p$) and ω_l is the frequency of a tunable laser used as the probe, generated by frequency modulating the pump light at Ω. This frequency, Ω, also corresponds to that of phonons interacting with optical photons, as the phonons are driven via the beat tone between pump and probe light with frequency $\Omega = \omega_l - \omega_p$. Combining equation 2.32 with the input-output formulism ($a_{\mathrm{out}} = -\sqrt{\kappa_{\mathrm{opt,c}}} a$), we obtain the response of the output field (a_{out}),

$$a_{\mathrm{out}}(\Omega) = \frac{\kappa_{\mathrm{opt,c}} a_{\mathrm{in}}}{i(\Omega - \Delta_{\mathrm{opt}}) - \frac{\kappa_{\mathrm{opt}}}{2} + \frac{g_{\mathrm{om}}^2}{(i(\Omega - \Omega_{\mathrm{m}}) - \frac{\Gamma}{2})}} \tag{2.33}$$

In an OMIT measurement, we detect the power of transmitted signal light through heterodyne detection. The power spectrum at the detector is,

$$P_{\mathrm{out}}(\Omega) = \hbar\langle a_{\mathrm{out}}^{\dagger} a_{\mathrm{out}}\rangle = \left| \frac{\kappa_{\mathrm{opt,c}}}{i(\Omega - \Delta_{\mathrm{opt}}) - \frac{\kappa_{\mathrm{opt}}}{2} + \frac{g_{\mathrm{om}}^2}{(i(\Omega-\Omega_{\mathrm{m}})-\frac{\Gamma}{2})}} \right|^2 P_{\mathrm{in}} \tag{2.34}$$

The characteristic dip of OMIT measured at the center of the spectrum ($\Omega = \Omega_{\mathrm{m}} = \Delta_{\mathrm{opt}}$) can be compared to the peak spectral response when there is no optomechanical coupling ($g_{\mathrm{om}} = 0$) to give insight to the cooperativity of the system.

$$\begin{aligned} \frac{P_{\mathrm{out}}}{P_{\mathrm{out}}(g_{\mathrm{om}}=0)} &= \left(\frac{\frac{\kappa_{\mathrm{opt}}}{2}}{\frac{\kappa_{\mathrm{opt}}}{2} + \frac{g_{\mathrm{om}}^2}{(\frac{\Gamma}{2})}} \right)^2 \\ &= \left(1 + \frac{4g_{\mathrm{om}}^2}{\Gamma\kappa_{\mathrm{opt}}} \right)^{-2} \\ &= (1 + C_{\mathrm{om}})^{-2}. \end{aligned} \tag{2.35}$$

Such a relation is also clear in figure 2.5 where we plot the OMIT spectral response from equation 2.34 while varying the value of optomechanical cooperativity.

2.4.2 Measurement in single-pass configuration

Measurement of optomechanical coupling rate in single-pass configuration is done by directly detecting the scattered optical response. Unlike in cavity optomechanics, the lack of an optical cavity prevents us from describing the system in terms of optical cavity modes and performing OMIT measurements. Here, we assume that the optical reflections from the crystal surfaces are negligible. In order to characterize the scattered optical response, we consider the Hamiltonian of a system where a phonon

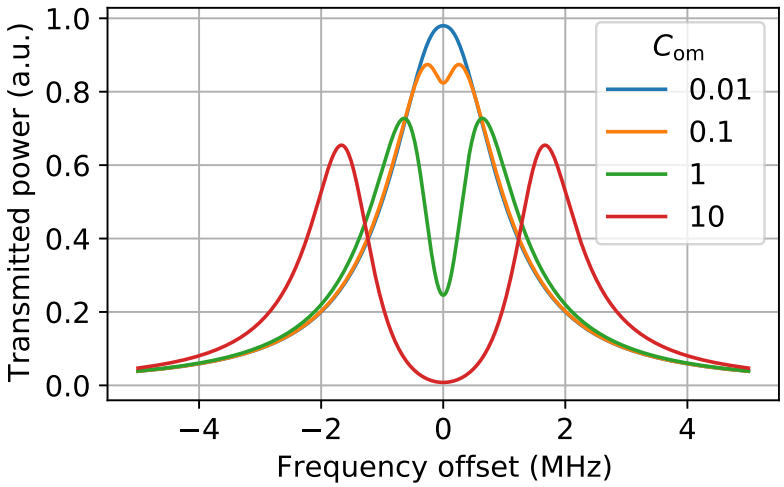

Figure 2.5: **Simulated OMIT spectrum** OMIT spectrum is simulated following equation 2.34. Parameters are set to be $\Gamma/2\pi = 500$ kHz and $\kappa_{opt}/2\pi = 2$ MHz. Optomechanical cooperativity (C_{om}) is varied between $0.01 \sim 10$. As we reach higher cooperativity, we observe a deeper characteristic dip at the center and optical mode splitting. This also indicates hybridization between optical and mechanical modes in the strong coupling regime.

mode couples to a continuum of pump and signal optical modes in k-space [52,73,74].

$$\begin{aligned} H = \int \hbar\omega_{\mathrm{p}}(k) a^{\dagger}_{\mathrm{p,k}} a_{\mathrm{p,k}} dk + \int \hbar\omega_{\mathrm{s}}(k) a^{\dagger}_{\mathrm{s,k}} a_{\mathrm{s,k}} dk + \hbar\Omega_{\mathrm{m}} b^{\dagger} b \\ + \left(\int \hbar g'_{\mathrm{om},0} a_{\mathrm{p,k}} a^{\dagger}_{\mathrm{s,k'}} b \frac{dk dk'}{2\pi} + \mathrm{H.C.} \right), \end{aligned} \tag{2.36}$$

where $a_{\mathrm{p,k}}$ ($a_{\mathrm{s,k}}$) is the annihilation operator for optical pump (signal) photon with wavevector k. Note that unlike the mode operators (a_{p}) previously in cavity optomechanics description which were adimensional, operators $a_{\mathrm{p,k}}$ and $a_{\mathrm{s,k}}$ have units of $\sqrt{\mathrm{Length}}$.

In reality, coupling between phonons and a continuum of traveling-wave optical fields across a bulk crystal with moderate thickness (several orders of magnitude larger than the acoustic wavelength) results in a non-negligible spatial variation in optical field amplitudes and optomechanical coupling rate, making it more intuitive to consider the Hamiltonian in real space with mode envelope operators. For example,

signal field amplitude gets larger along the axis of propagation due to pump scattering. To express the Hamiltonian in terms of real space mode envelope operator, we can use the fact that operators in k-space are Fourier-transformed envelope field operators,

$$a_{\mathrm{p(s),k}} = \frac{1}{\sqrt{2\pi}} \int A_{\mathrm{p(s)}}(z) e^{-i(k-k_{\mathrm{p(s)}})z} dz, \tag{2.37}$$

where A_{p} (A_{p}) is the envelope field operator for the optical pump (signal). Taylor expanding the dispersion relation of optical frequencies in k-space, we can write,

$$\omega_{\mathrm{p(s)}}(k) = \omega(k_{\mathrm{p(s)}}) + (k - k_{\mathrm{p(s)}}) \frac{\partial \omega(k)}{\partial k}\Big|_{k=k_{\mathrm{p(s)}}} .... \tag{2.38}$$

As optical group velocity is given as, $v_{\mathrm{opt}} = \frac{\partial \omega(k)}{\partial k}\big|_{k=k_{\mathrm{p}}} = -\frac{\partial \omega(k)}{\partial k}\big|_{k=k_{\mathrm{s}}}$, this equation can be simplified when there is negligible group velocity dispersion,

$$\begin{aligned} \omega_{\mathrm{p}}(k) &= \omega_{\mathrm{p}} + (k - k_{\mathrm{p}}) v_{\mathrm{opt}} \\ \omega_{\mathrm{s}}(k) &= \omega_{\mathrm{s}} - (k - k_{\mathrm{s}}) v_{\mathrm{opt}}. \end{aligned} \tag{2.39}$$

$\omega_{\mathrm{p}} = \omega(k_{\mathrm{p}})$ Substituting equations 2.37 and 2.39 into 2.36, the Hamiltonian becomes,

$$\begin{aligned} H = \hbar \int A_{\mathrm{p}}^{\dagger}(z)(\omega_{\mathrm{p}} - i v_{\mathrm{opt}} \partial_z) A_{\mathrm{p}}(z) dz + \hbar \int A_{\mathrm{s}}^{\dagger}(z)(\omega_{\mathrm{s}} + i v_{\mathrm{opt}} \partial_z) A_{\mathrm{s}}(z) dz \\ + \hbar g'_{\mathrm{om},0} \left(\int A_{\mathrm{p}}(z) A_{\mathrm{s}}^{\dagger}(z) b dz + \mathrm{H.C.} \right), \end{aligned} \tag{2.40}$$

assuming pump light, signal light, and acoustic modes are phase-matched. For convenience, we modify the expression as,

$$\begin{aligned} H = \hbar \int A_{\mathrm{p}}^{\dagger}(z) \hat{\omega}_{\mathrm{p}} A_{\mathrm{p}}(z) dz + \hbar \int A_{\mathrm{s}}^{\dagger}(z) \hat{\omega}_{\mathrm{s}} A_{\mathrm{s}}(z) dz \\ + \hbar g'_{\mathrm{om},0} \left(\int A_{\mathrm{p}}(z) A_{\mathrm{s}}^{\dagger}(z) b dz + \mathrm{H.C.} \right), \end{aligned} \tag{2.41}$$

where spatial operators are simplified as $\hat{\omega}_{\rm p} = (\omega_{\rm p} - iv_{\rm opt}\partial_z)$ and $\hat{\omega}_{\rm s} = (\omega_{\rm s} + iv_{\rm opt}\partial_z)$. From the Hamiltonian and the commutation relation of the envelope operators ($[A_\gamma(z), A^\dagger_{\gamma'}(z')] = \delta_{\gamma\gamma'}\delta(z-z')$ where $\{\gamma,\gamma'\} = \{\rm p,s\}$), we can obtain the equations of motion,

$$\begin{aligned}
\dot{b} &= \left(-i\Omega_{\rm m} - \frac{\Gamma}{2}\right) b - ig'_{\rm om,0}\int dz A^\dagger_{\rm p} A_{\rm s} \\
\dot{A}_{\rm p} &= -i\hat{\omega}_{\rm p} A_{\rm p} - ig'_{\rm om,0} A_{\rm s} b^\dagger \\
\dot{A}_{\rm s} &= -i\hat{\omega}_{\rm s} A_{\rm s} - ig'_{\rm om,0} A_{\rm p} b.
\end{aligned} \tag{2.42}$$

In the rotating frame, $A_{\rm p(s)}(t) = \bar{A}_{\rm p(s)}(t)e^{-i\omega_{\rm p(s)}t}$ and $b(t) = \bar{b}(t)e^{-i\Omega_{\rm m}t}$,

$$\begin{aligned}
\dot{\bar{b}} &= -\frac{\Gamma}{2}\bar{b}(t) - ig'_{\rm om,0}\int dz \bar{A}^\dagger_{\rm p}\bar{A}_{\rm s} \\
\dot{\bar{A}}_{\rm p} &= -v_{\rm opt}\partial_z \bar{A}_{\rm p} - ig'_{\rm om,0}\bar{A}_{\rm s}\bar{b}^\dagger \\
\dot{\bar{A}}_{\rm s} &= v_{\rm opt}\partial_z \bar{A}_{\rm s} - ig'_{\rm om,0}\bar{A}_{\rm p}\bar{b}.
\end{aligned} \tag{2.43}$$

We can solve the equation of motion for $\bar{A}_{\rm s}$ assuming an undepleted pump ($\bar{A}_{\rm p}$ is a constant) and at a steady state in time.

$$\begin{aligned}
v_{\rm opt}\partial_z \bar{A}_{\rm s} &= ig'_{\rm om,0}\bar{A}_{\rm p}\bar{b} \\
v_{\rm opt}(\bar{A}_{\rm s}(z) - \bar{A}_{\rm s}(L_{\rm m})) &= ig'_{\rm om,0}\bar{A}_{\rm p}\bar{b}(z - L_{\rm m}) \\
v_{\rm opt}\bar{A}_{\rm s}(z) &= ig'_{\rm om,0}\bar{A}_{\rm p}\bar{b}(z - L_{\rm m}),
\end{aligned} \tag{2.44}$$

where $\bar{A}_{\rm s}(L_{\rm m}) = 0$ since there is no medium to reflect off from at the end of the substrate. The signal resulting from scattering throughout the whole medium corresponds to that at $z = 0$, and this is the signal whose power we end up measuring through the detector.

$$\bar{A}_{\rm s}(0) = -i\frac{g'_{\rm om,0}}{v_{\rm opt}}\bar{A}_{\rm p}\bar{b}L_{\rm m} \tag{2.45}$$

$$P_{\rm s}(0) = \frac{g'^2_{\rm om,0}}{v^2_{\rm opt}}P_{\rm p}n_{\rm m}L^2_{\rm m} = GP_{\rm p}n_{\rm m} \tag{2.46}$$

For simplification, we define a scattered signal power per pump power per phonon in the crystal $G = \left(\frac{g'_{\mathrm{om},0} L_{\mathrm{m}}}{v_{\mathrm{opt}}}\right)^2$.

Chapter 3

Piezoelectric coupling to BAW modes

3.1 Introduction

Piezoelectricity is a linear electromechanical interaction between mechanical motion and electric field in crystals with no inversion symmetry. It is a well-understood phenomenon that is widely used in industries and research as motors, actuators, sensors, and many other applications.

In the context of circuit QAD, piezoelectricity is one of the most utilized interactions to couple a microwave element, such as a qubit, to a mechanical element, such as an acoustic resonator. Many of the the implementations of quantum acoustic devices [7–9, 31] and piezo-optomechanical microwave-to-optical transducers [18–22] are based on piezoelectric interaction. In particular, strong piezoelectric couplings have been demonstrated between a superconducting qubit and a mechanical resonator [7–9, 31].

The ability to even reach strong coupling in quantum systems, however, can be a detriment in the context of qubit lifetimes [7, 8, 27–31], if there exists a chance of

an unintended coupling or couplings to unwanted lossy acoustic modes. Anomalous piezoelectricity, leading to an unintended electromechanical coupling, can occur at the surface [34], defect sites [35], and under external stress [36, 37] of non-piezoelectric materials, as a result of local disturbances in inversion symmetry. Several studies on anomalous piezoelectricity [34,38], and on controlled couplings to a variety of acoustic density of states [32, 33] have been done. However, there is more to be explored to fully harness the benefits of piezoelectricity while sufficiently avoiding its drawbacks in quantum acoustic systems.

In this chapter, we present a simple electromechanical system that piezoelectrically couples a 3D microwave cavity with an HBAR. Then, we discuss the effects of anomalous piezoelectricity in qubit lifetimes and find how small parasitic piezoelectricity can lead to noticeable qubit decoherence, potentially becoming a bottleneck in future qubit developments. Combining the design with Brillouin optomechanical interaction from the previous chapter allows a sensitive readout of piezoelectrically-driven phonons through parametrically-enhanced strong optomechanical coupling. Such an approach not only allows us to create a novel piezo-optomechanical (piezo-Brillouin) device that mediates coupling between microwave and optical domain but also provides us with a sensitive platform that can potentially detect anomalous piezoelectricity in crystals.

3.2 Piezoelectric coupling rate to BAW

A simple illustration of piezoelectric coupling between a microwave circuit and a BAR is shown in figure 3.1. The electromechanical interaction Hamiltonian of a cavity electromechanical system can be expressed as a product between piezo-induced stress

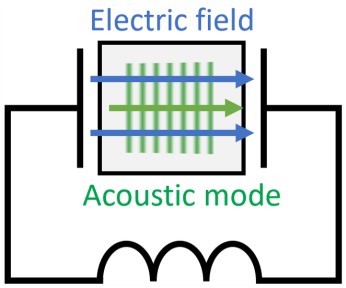

Figure 3.1: **Sketch of an acoustic resonator coupled to a microwave circuit.** A bulk acoustic resonator is placed between the capacitor of an LC microwave circuit. The electric field between the capacitor pads piezoelectrically couples to the bulk acoustic modes of the acoustic resonator. For simplicity, coupling to only the longitudinal acoustic mode is illustrated in the figure.

field ($\overline{\overline{\sigma}}(\bar{r}) = \overline{\overline{c}} \cdot \overline{\overline{d}} \cdot E(\bar{r})$) and strain field in the substrate ($\overline{\overline{s}}(\bar{r})$), approximated as,

$$H_{\text{int}} = \int \overline{\overline{\sigma}}(\bar{r}) \cdot \overline{\overline{s}}(\bar{r}) dV, \tag{3.1}$$

where $\overline{\overline{c}}$ is the stiffness tensor and $\overline{\overline{d}}$ is the piezoelectric tensor. In our system, we chose the coupling to occur predominantly between the z-directional electric fields and z-directional longitudinal strain fields through microwave cavity design and material properties. Thus, we consider longitudinal strain fields ($s(\bar{r}) = S_z(\bar{r})$) of an acoustic resonator interacting with an electric field of a microwave resonator along the z-axis ($\sigma(\bar{r}) = c_{33} d_{33} E_z(\bar{r})$, c_{33} and d_{33} are relevant stiffness and piezoelectric tensor elements), resulting in,

$$H_{\text{int}} = c_{33} d_{33} \int E_z(\bar{r}) S_z(\bar{r}) dV. \tag{3.2}$$

Quantizing the electric ($E_z(\bar{r}) = \bar{E}_z(\bar{r})(c + c^\dagger)$) and strain fields ($S_z(\bar{r}) = \bar{S}_z(\bar{r})(b + b^\dagger)$) with microwave mode ($c$) and acoustic mode ($b$) annihilation operators, the interaction Hamiltonian leads to the expression for electromechanical coupling rate,

$$g_{\text{em}} = \frac{c_{33} d_{33}}{\hbar} \int_{\text{pz}} \bar{E}_z(\bar{r}) \bar{S}_z(\bar{r}) dV, \tag{3.3}$$

where $\int_{\mathrm{pz}} dV$ is a volume integral across the piezoelectric substrate.

The acoustic strain field is assumed to be a standing wave in the longitudinal direction and a Gaussian shape in the transverse direction with mode waist (i.e. in the case of a stable plano-convex resonator) proportional to the probing optical mode waist [54] ($r_{\mathrm{m}} = r_{\mathrm{opt}}/\sqrt{2}$), resulting in an expression,

$$\bar{S}_z(\bar{r}) = S_0 e^{-\frac{r^2}{r_{\mathrm{m}}^2}} \sin\left(\frac{2\pi z}{\lambda_{\mathrm{m}}}\right) \hat{z}, \tag{3.4}$$

where λ_{m} is the acoustic wavelength and S_0 is the zero-point strain. Using the relation between strain and displacement ($\bar{S}_z(\bar{r}) = \frac{\partial U_z}{\partial z}$), and the expression for stiffness constant ($v_{\mathrm{m}} = \sqrt{\frac{c_{33}}{\rho}}$, where v_{m} is the acoustic velocity in the longitudinal direction along z-direction), we can recall equation 2.14 to normalize the strain field such that the zero-point strain is, $S_0 = \sqrt{\frac{2\hbar\Omega_{\mathrm{m}}}{c_{33} L_{\mathrm{m}} A_{\mathrm{m}}}}$.

Most of the microwave resonators we consider for our design (further elaborated in section 3.4) have microwave modes that are spatially larger than the acoustic modes, such that the electric field parallel to the phonon propagation (z-direction) within the microwave/acoustic mode overlap volume can be treated as uniform,

$$\bar{E}_z(\bar{r}) \approx E_0 \hat{z}, \tag{3.5}$$

where E_0 is the zero-point electric field strength within the overlapping mode volume. Following equation 2.9, we can approximate the zero-point field, $E_0 \approx \sqrt{\frac{\hbar\Omega_\mu}{2\epsilon_0 \epsilon_r V_\mu}}$, where Ω_μ is the microwave mode frequency and V_μ is the microwave mode volume. In our experiment, we obtain the electric field of the system through Ansys HFSS (3D high-frequency simulation software). It is convenient, when using the simulation software, to output the electric field values of the microwave mode when the E-field is at its maximum and H-field is zero. This results in a simulated field amplitude of, in terms of zero-point field, $E_{\mathrm{sim}} = \sqrt{2} E_0$.

Combining equations (3.3), (3.5) and (3.4), we obtain the electromechanical coupling rate,

$$\begin{aligned} g_{\mathrm{em}} &= \frac{1}{\hbar} c_{33} d_{33} s_0 E_0 \int_{\mathrm{pz}} e^{-\frac{r^2}{r_{\mathrm{m}}^2}} \sin\left(\frac{2\pi z}{\lambda_{\mathrm{m}}}\right) dV \\ &= d_{33} E_{\mathrm{sim}} \frac{\lambda_{\mathrm{m}}}{\pi} \sqrt{\frac{\Omega c_{33} A_{\mathrm{m}}}{2\hbar L_{\mathrm{m}}}} \sin^2\left(\frac{\pi t_{\mathrm{pz}}}{\lambda_{\mathrm{m}}}\right), \end{aligned} \tag{3.6}$$

where t_{pz} is the piezoelectric substrate thickness.

There are three distinct cases of piezoelectric coupling that one should consider. Firstly, piezoelectricity can be distributed evenly throughout the entire bulk of the acoustic substrate. In this case, acoustic modes with an even longitudinal index ($t_{\mathrm{pz}} = n\frac{\lambda_{\mathrm{m}}}{2}$ with even n) will have zero coupling rate ($\sin^2\left(\frac{\pi t_{\mathrm{pz}}}{\lambda_{\mathrm{m}}}\right) = 0$), while the odd index modes ($t_{\mathrm{pz}} = n\frac{\lambda_{\mathrm{m}}}{2}$ with odd n) will have maximal coupling ($\sin^2\left(\frac{\pi t_{\mathrm{pz}}}{\lambda_{\mathrm{m}}}\right) = 1$). Secondly, substrates may have surface piezoelectricity only on one side of the substrate. In this case, piezoelectricity is concentrated within a thin surface layer on one surface with thickness t_{pz} ($t_{\mathrm{pz}} \ll \lambda_{\mathrm{m}}$), while the bulk remains non-piezoelectric, resulting in a simplification of the sin term in the coupling rate expression as $\sin^2\left(\frac{\pi t_{\mathrm{pz}}}{\lambda_{\mathrm{m}}}\right) = \left(\frac{\pi t_{\mathrm{pz}}}{\lambda_{\mathrm{m}}}\right)^2$. Lastly, there is the case for surface piezoelectricity on both sides of the substrate. Here, the modulation of zero and non-zero coupling rate for even and odd indexed acoustic modes appears as in the bulk piezoelectricity case, while the non-zero coupling rate is proportional to t_{pz}^2 as in the single-sided surface piezoelectricity case. One should keep these observations in mind since they will be important in understanding the measurement responses later on in the dissertaion.

Another aspect of g_{em} is that it has a factor of $1/\sqrt{L_{\mathrm{m}}}$. Although we are integrating along the full length of the substrate, the sin term in the expression results in values equivalent to integrating along an effective piezoelectric thickness of $t_{\mathrm{pz}} < \lambda_{\mathrm{m}}/2$. Hence the factor, $1/\sqrt{L_{\mathrm{m}}}$, from strain normalization term remains throughout the expression of g_{em}. Such dependency of g_{em} in substrate thickness suggests that using thinner substrate is advantageous in achieving larger g_{em}, hinting at ways our system

can be improved.

3.3 Number of piezoelectrically-driven phonons

Now that we have an expression for the piezoelectric coupling rate, g_{em}, we can solve the number of piezoelectrically driven phonons in terms of the coupling rate and the microwave photon number. The interaction Hamiltonian of a microwave cavity mode and an acoustic cavity mode coupled through piezoelectricity is,

$$H_{\mathrm{int}} = \hbar g_{\mathrm{em}}(c^{\dagger}b + cb^{\dagger}). \tag{3.7}$$

Corresponding Heisenberg equations of motion are given as,

$$\begin{aligned} \dot{c} &= -ig_{\mathrm{em}}b - \frac{\kappa_{\mu}}{2}c + \sqrt{\kappa_{\mu,\mathrm{c}}}c_{\mathrm{in}} \\ \dot{b} &= -ig_{\mathrm{em}}c - \frac{\Gamma}{2}b, \end{aligned} \tag{3.8}$$

where κ_{μ} ($\kappa_{\mu,\mathrm{c}}$) is the microwave cavity dissipation rate (external coupling rate), c is the annihilation operator for microwave mode, and c_{in} is the external microwave input field ($P_{\mathrm{in}}/\hbar\Omega_{\mu} = \langle c_{\mathrm{in}}^{\dagger}c_{\mathrm{in}}\rangle$). Solving the equations of motion in steady state, we get the expression for piezoelectrically-driven phonons,

$$\begin{aligned} n_{\mathrm{m}} &= \left(\frac{g_{\mathrm{em}}}{\frac{2g_{\mathrm{em}}^2}{\kappa_{\mu}} + \frac{\Gamma}{2}}\right)^2 n_{\mu} \\ &\sim \left(\frac{2g_{\mathrm{em}}}{\Gamma}\right)^2 n_{\mu}, \end{aligned} \tag{3.9}$$

where n_{μ} is the microwave photon number that can be separately characterized, and assuming $g_{\mathrm{em}}^2/\kappa_{\mu} \ll \Gamma$, which is a realistic assumption (see chapter 5-7).

3.4 3D microwave cavity designs for piezoelectric coupling

In our design, we realize piezoelectric coupling between a 3D microwave cavity and an HBAR. The HBAR, with mm-scale dimensions, is placed inside the microwave cavity, which has cm-scale dimensions (see figure 3.2).

Although there are several alternative ways to couple to an HBAR [7, 23, 33], we choose to use a 3D microwave cavity. 3D designs grant us intuitive ways to tune the resonances through geometrical modifications. Since the microwave cavity is physically separate from other elements of the system, unlike certain 2D devices where most of the elements have to be fabricated on a single chip, we can easily integrate our device with other elements such as a Fabry-Pérot optical cavity. Such a modular nature of the design allows for a variety of piezo-optomechanical devices that can be used as transducers, sensors, etc. Moreover, 3D microwave devices are already used in conjunction with quantum technologies [75, 76], and have the potential to reach extremely high-quality factors (Q-factors) if needed [77]. Additionally, modes of a 3D microwave cavity are well understood and are easy to simulate using commercial software such as HFSS and COMSOL. And lastly, it is often straightforward to prepare 3D microwave cavities through conventional machining. Compared to other 2D microwave cavities, our approach does not involve the need for complicated fabrication steps, thus it is not limited by fabrication techniques.

We consider a few different 3D microwave cavity designs, each with its own strengths and drawbacks. First, we consider a simple rectangular cavity, shown in figure 3.2a. Assuming an HBAR is placed at the center, we can use the TE110 and TE130 modes (depending on the target frequency) to piezoelectrically couple mechanical modes to microwave modes. Such a design is convenient to machine and easy to access optically by adding cylindrical through-holes with waveguide cutoff frequencies

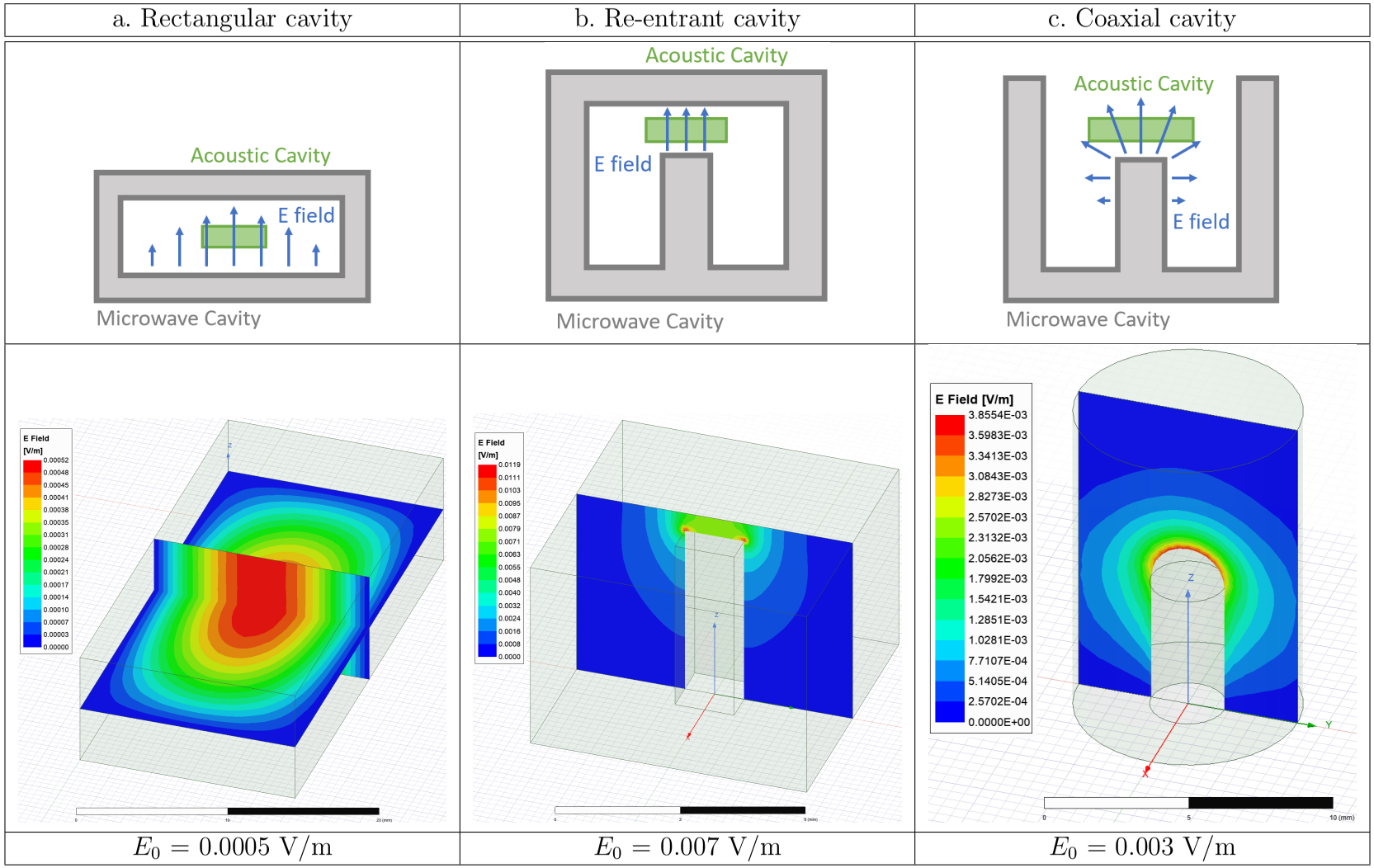

Figure 3.2: **Microwave cavity designs for piezoelectric coupling** (From top to bottom) Cross-sectional sketch, HFSS simulation, and average E-field along the microwave/acoustic mode overlap region. The cross-sectional sketch includes E-field, microwave cavity, and acoustic cavities. HFSS simulation includes E-field strength shown in the color plot. All cavity designs have resonance frequency around 10.5 GHz and E-field corresponding to mode energy of $\hbar\omega_\mu = 1.1 \times 10^{-24}$J $\sim 7\mu$eV. E-field values are taken where the acoustic substrate is expected to be placed. (i.e. at the center for a., and ~ 500 um above the pin for b. and c.) a. Figure for a rectangular microwave cavity. TE110 mode is illustrated. Note that higher order mode (TE130) can also be used for piezoelectric coupling at a higher frequency. b. Figure for a re-entrant cavity. HFSS simulation indicates a highly concentrated E-field between the center pin and the top lid. c. Figure for a quarter-wavelength coaxial stub cavity. The fundamental TEM mode of the design is used. The center pin has a round design to minimize the edge effect.

much higher than the cavity resonance frequency. However, rectangular cavities can have multiple spurious modes nearby the mode of interest due to their exact geometry, especially when using higher-order modes, requiring extra care when characterizing and tuning the target mode. Moreover, it is challenging to achieve wide (> 500 MHz) frequency tunability as it leads to mode distortion. As an alternative, we can use a re-entrant cavity, as shown in figure 3.2b. The electric field of a re-entrant cavity is concentrated between the center pin and the lid which behave like a parallel plate capacitor. Hence, re-entrant cavities tend to have stronger electric field and piezoelectric coupling, compared to other types of cavities, as shown by the value of E_0 in figure 3.2. Also, the resonance frequency is well isolated from other responses in frequency space. However, limited tunability (< 200 MHz) and practical challenges in making optical light accessible are some of the problems with the design. The last option we consider is a quarter-wavelength coaxial stub cavity, shown in figure 3.2c. Coaxial cavities are common resources for quantum technologies [76], that can reach beyond a Q-factor of $Q_\mu > 10^7$ [77]. Since the microwave field is concentrated around the quarter-wavelength central post (TEM mode), the resonance frequency can be easily adjusted by changing the post length. If seam loss through a moving post is a concern, one can instead insert a dielectric rod to tune the resonance frequency [78]. Additionally, the fundamental resonance frequency is well isolated from higher-order modes in frequency space. Challenges in using a coaxial cavity include a potential machining challenge if the design requires a hole through the central pin for optical access.

3.5 Relation to qubit lifetimes

Piezoelectric coupling, integrated with quantum circuits, can be a valuable resource enabling the control of quantum acoustics, but it also has the potential to harm the

coherence of the quantum circuits. This has already been observed in many studies incorporating superconducting qubits with piezoelectricity [7, 8, 27–33], where the qubit lifetimes are up to two orders of magnitude shorter compared to conventional transmons. Besides, if there exists anomalous piezoelectricity in qubit substrates [34], it can directly lead to incoherent couplings to an acoustic continuum, setting an intrinsic limit to qubit lifetimes [38].

To understand the decoherence mechanisms in a qubit that is piezoelectrically coupled to an acoustic continuum (or equivalently, experiences acoustic spontaneous emission), there are several assumptions we make. For simplicity, we consider piezoelectric coupling that occurs from the capacitor pads of a qubit. Since the dimensions of the capacitor pads (∼100um) are typically much larger than acoustic wavelengths (∼1um), we can assume that the acoustic waves are predominantly emitted in the z-direction (perpendicular to the capacitor pads). Also, we assume that we are only coupling to longitudinal acoustic waves, which is valid in materials such as x-cut quartz with d_{33} piezoelectric tensor component much greater than the shear coupling component (d_{36}). For a further study that includes shear waves, see reference [33].

The calculation of a qubit decay rate from piezoelectricity can be done through Fermi's golden rule,

$$\gamma_{\text{em}} = 2\pi \sum_{\bar{k}} |g_{\text{em}}\left(\bar{k}\right)|^2 \delta(\omega(\bar{k}) - \omega), \tag{3.10}$$

where γ_{em} is the decay rate. The piezoelectric coupling rate $g_{\text{em}}\left(\bar{k}\right)$ in the expression is different from equation 3.6 since we are now assuming couplings to a continuum of plane wave longitudinal acoustic modes rather than a standing wave acoustic cavity mode. A plane-wave acoustic mode with wave vector $\bar{k}$ is,

$$s_{\bar{k}}(\bar{x}) = S_0 e^{-i\bar{k}\cdot\bar{x}}\hat{k}, \tag{3.11}$$

where S_0 is the zero-point field. Combining this with interaction Hamiltonian (equa-

tion 3.1) and piezo-induced stress field ($\overline{\overline{\sigma}}(\bar{x}) = \overline{\overline{c}}_{\mathrm{p}} \cdot \overline{\overline{d}} \cdot \bar{E}(\bar{x})$), we can get an expression for the piezoelectric coupling rate with wave vector $\bar{k}$,

$$\begin{aligned} g_{\mathrm{em}}\left(\bar{k}\right) &= \frac{1}{\hbar}\int \left(\overline{\overline{c}}_{\mathrm{p}} \cdot \overline{\overline{d}} \cdot \bar{E}(\bar{x})\right) \cdot \left(S_0 e^{-i\bar{k}\cdot\bar{x}}\hat{k}\right) dV \\ &= \frac{S_0}{\hbar}\int X(\bar{x}) e^{-i\bar{k}\cdot\bar{x}} dV \\ &= (\sqrt{2\pi})^3 \frac{S_0}{\hbar}\widetilde{X}(\bar{k}), \end{aligned} \tag{3.12}$$

where $X(\bar{x}) = \overline{\overline{c}}_{\mathrm{p}} \cdot \overline{\overline{d}} \cdot \bar{E}(\bar{x}) \cdot \hat{k}$ and $\widetilde{X}(\bar{k})$ is the 3D Fourier transform of $X(\bar{x})$ ($\widetilde{X}(\bar{k}) = \mathcal{F}(X(\bar{x}))$). Since we are assuming that the dominant component of the strain field is in longitudinal z-direction, $X(\bar{x}) = c_{33}d_{33}E_z(\bar{x})$. From the same reason, zero-point field $S_0 = \sqrt{\frac{\hbar\Omega_{\mathrm{m}}}{2c_{33}V_{\mathrm{m}}}}$ can be obtained following equation 2.14. Using Fermi's golden rule (equation 3.10) and converting a discrete sum to an integral, we get the following equation,

$$\gamma_{\mathrm{em}} = 2\pi V_{\mathrm{m}} \frac{S_0^2}{\hbar^2}\int \widetilde{X}^2(\bar{k})\delta(\omega(\bar{k}) - \omega) d^3k. \tag{3.13}$$

3.5.1 Analytical approach: Rectangular pad example

Typically, the design of a qubit involves metallic pads that provide capacitance to the qubit. Let's assume that a qubit generates a uniform electric field over a rectangular region with side lengths a and b, defined by the dimensions of the capacitor pads. Note that this is a much-simplified picture. In reality, there are electric fields concentrated around the edges and the junctions (edge effect). Also, assume that the thickness of the piezoelectric layer is t_{pz}. Then, the z-directional component of the electric field can be expressed as,

$$E_z(\bar{x}) = E_0 \frac{k_z}{k} \mathrm{rect}\left(\frac{x}{a}\right) \mathrm{rect}\left(\frac{y}{b}\right) \mathrm{rect}\left(\frac{z}{t_{\mathrm{pz}}}\right). \tag{3.14}$$

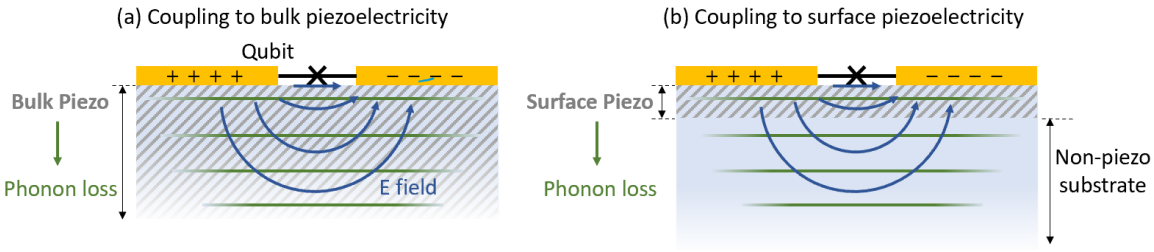

Figure 3.3: **Sketch of different sources of piezoelectric coupling** Drawn in orange are capacitor pads, between which there is a Josephson junction forming a transmon qubit. Light blue is the substrate and grey shade is the piezoelectric layer region. Indicated in green is the acoustic radiation and blue is the electric field between the capacitor pads. a. Maximal piezoelectric coupling between the qubit and the acoustic substrate is achieved when there exists bulk piezoelectricity across the substrate. b. The qubit can piezoelectrically couple to the substrate if there is a thin piezoelectric layer ($t_{\mathrm{pz}} \ll \lambda_{\mathrm{m}}$). However, the coupling strength, in this case, is much weaker than that in a.

Combining this with equation 3.13, we get the following expression,

$$\begin{aligned}\gamma_{\mathrm{em}} &= 2\pi V_{\mathrm{m}} \frac{S_0^2 c_{33}^2 d_{33}^2}{\hbar^2} \int \mathcal{F}^2 \left(E_0 \frac{k_z}{k} \mathrm{rect}\left(\frac{x}{a}\right) \mathrm{rect}\left(\frac{y}{b}\right) \mathrm{rect}\left(\frac{z}{t_{\mathrm{pz}}}\right) \right) \delta(\omega(\bar{k}) - \omega) d^3k \\ &= \frac{\lambda_{\mathrm{m}} E_0^2 c_{33} d_{33}^2 ab}{\pi\hbar} \sin^2\left(\frac{\pi t_{\mathrm{pz}}}{\lambda_{\mathrm{m}}}\right),\end{aligned} \tag{3.15}$$

where $a \gg t_{\mathrm{pz}}$, $b \gg t_{\mathrm{pz}}$, and $k_z \sim k$. Given realistic numbers, a and b are around 100 $\sim$ 500 um and $t_{\mathrm{pz}} < 1$ um. Estimating γ_{em} at $a = 500$ um, $b = 250$ um, $E_0 = 0.1$ V/m (from simulation), $c_{33} = 496$ GPa (material property of sapphire), and $\lambda_{\mathrm{m}} = 1.9$ um (at 6 GHz), we get $\gamma_{\mathrm{em}} \propto d_{33}^2 \sin^2(\frac{\pi t_{\mathrm{pz}}}{\lambda_{\mathrm{m}}})$.

Qubit T_1 lifetime limited by piezoelectricity can be calculated in two separate cases (See figure 3.3). First is when the coupling is maximal ($\sin^2(\frac{\pi t_{\mathrm{pz}}}{\lambda_{\mathrm{m}}}) = 1$). This occurs when the thickness of the piezoelectric layer is odd integer multiples of half wavelength, or when the piezoelectricity originates from the bulk of the substrate. Maximal piezoelectric coupling condition assuming $d_{33} = 1$ pm/V gives $\gamma_{\mathrm{em}}/2\pi \sim 550$ kHz, which corresponds to $T_1 = 290$ ns. In order to have a reasonably long lifetime of $T_1 > 1$ ms ($\gamma_{\mathrm{em}}/2\pi < 160$ Hz), it requires a very small piezoelectric constant, $d_{33} < 17$ fm/V. Another case we should consider is when piezoelectricity is concentrated within

a thin layer on the surface of a substrate. Simplifying the expression for the qubit loss rate for $t_{\mathrm{pz}} \ll \lambda_{\mathrm{m}}$, we have $\gamma_{\mathrm{em}} \propto d_{33}^2(\frac{\pi t_{\mathrm{pz}}}{\lambda_{\mathrm{m}}})^2$. Assuming piezoelectricity of $d_{33} =$ 1 pm/V only exists within a few atomic layers ($\sim$ 1 nm), $\gamma_{\mathrm{em}}/2\pi$ becomes 1.6 Hz, corresponding to $T_1 \sim 100$ ms. Note that in this model only a very thin layer is needed ($\gtrsim$ 10 nm) to limit qubit T_1 below 1 ms.

3.5.2 Utilizing simulation data for edge fields

There are several assumptions that we made in the calculation of γ_{em} in the previous section that can be further improved. One such assumption is incorporating the edge fields of the electric field profile. The value of $E_0 = 0.1$ V/m from earlier is chosen by observing the Maxwell electromagnetic field simulation of 500 um by 250 um capacitor pads of a transmon. We took the value of the electric field right below the center of the capacitor pad. However, as shown in figure 3.4(b-c), the simulation predicts edge fields that are more than an order of magnitude larger than the E_0 value used.

As an alternative way of calculating γ_{em}, we can directly import the electric field simulation data from the software. Shown in figure 3.4c is a zoomed-in electric field profile data within 1 um around the edge. Due to meshing limitations, we chose to work with a 2D cross-section of a 500 um wide, 250 um long, and 80 nm high capacitor. It is clear from the figure that we are indeed observing an edge effect. In order to take the edge fields into account, we revisit equation 3.13. Since we are considering coupling to longitudinal acoustic modes along z-direction, $X(\bar{x}) = c_{33}d_{33}E_z(\bar{x})$ assumption still holds as in the previous section, resulting in,

$$\gamma_{\mathrm{em}} = 2\pi V_{\mathrm{m}} \frac{S_0^2 c_{33}^2 d_{33}^2}{\hbar^2} \int \widetilde{E}_z^2(\bar{k})\delta(\omega(\bar{k}) - \omega)d^3k. \tag{3.16}$$

$\widetilde{E}_z(\bar{k})$ can be directly obtained through Fourier transforming the electric field profile (in figure 3.4b) within a t_{pz} thick piezoelectric layer ($\widetilde{E}_z(\bar{k}) = \mathcal{F}(E_z(\bar{x})\mathrm{rect}(z/t_{\mathrm{pz}}))$),

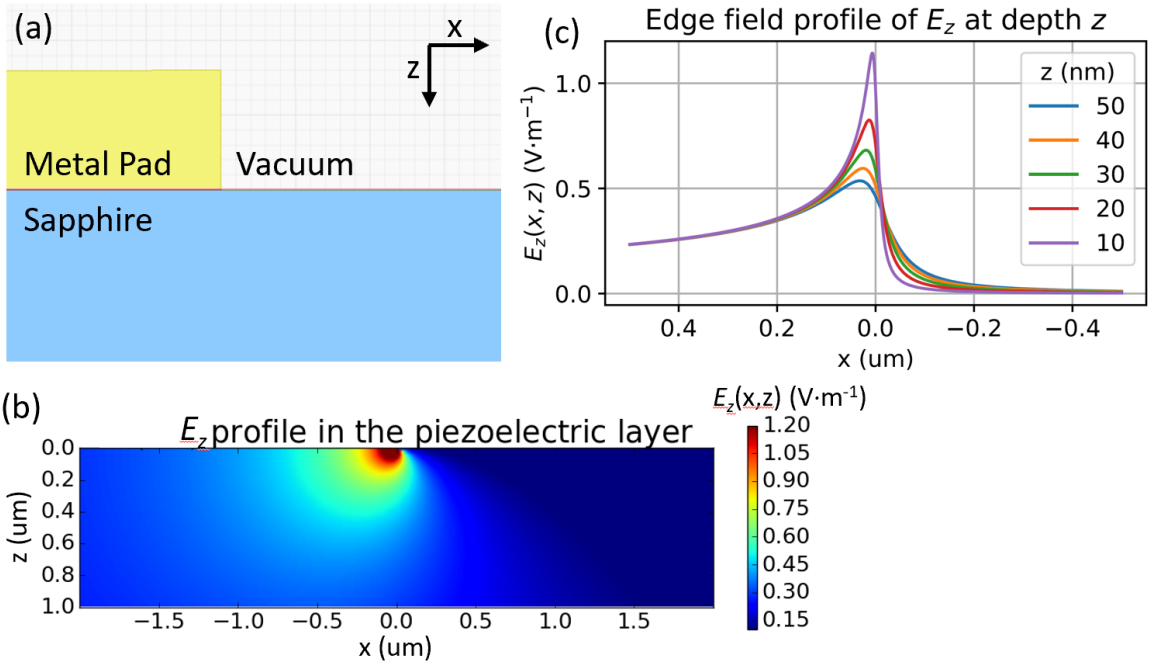

Figure 3.4: **Simulation data of E_z electric field near the edge of the capacitor** a. Simulation in Maxwell software. The yellow region corresponds to the metallic capacitor pad, blue to the sapphire substrate, and white to the vacuum. The figure shown here is zoomed in to be visually clear. The simulated metal pad has a height of 80 nm and a width of 500 um. The simulation is simplified into 2D instead of 3D due to meshing constraints. b. Colorplot of E_z field profile in the substrate. $z = 0$ um is defined at the metal-substrate interface, and z increases along the substrate depth. $x = 0$ is defined at the tip of the metal pad (metal-vacuum interface), where left or negative x is the metal side. We see the electric field peaking at $(x, z) = (0,0)$, which is a clear indication of an edge effect. c. 2D cross-sectional view of E_z profile at multiple positions inside the substrate. Here, we again see the edge field effect.

which we then integrate over $\bar{k}$ satisfying $|\bar{k}| = \omega/v_{\mathrm{m}}$ to get the value inside the integral. Note that the $\mathrm{rect}(z/t_{\mathrm{pz}})$ term in the electric field that gets Fourier transformed gives rise to a $\sin(\pi t_{\mathrm{pz}}/\lambda_{\mathrm{m}})$ term. From this, we observe a relation between T_1, d_{33}, and t_{pz},

$$T_1 = \frac{1}{\gamma_{\mathrm{em}}} \propto \frac{1}{d_{33}^2 \sin^2\left(\frac{\pi t_{\mathrm{pz}}}{\lambda_{\mathrm{m}}}\right)}. \tag{3.17}$$

Similar to the previous section, we can divide the result into two different cases - when $t_{\mathrm{pz}} = n\lambda_{\mathrm{m}}/2$ for odd n and when $t_{\mathrm{pz}} \ll \lambda_{\mathrm{m}}$. In the former case of maximal piezoelectric coupling, or bulk piezoelectricity, having $d_{33} = 1$ pm/V gives an extremely

Method	Piezo assumption	t_{pz}	d_{33}	Qubit T_1
Analytic	Bulk	n/a	1 pm/V	290 ns
Analytic	Bulk	n/a	17 fm/V	1 ms
Analytic	Surface	1 nm	1 pm/V	100 ms
Analytic	Surface	10 nm	1 pm/V	1 ms
Simulation	Bulk	n/a	1 pm/V	100 ns
Simulation	Bulk	n/a	10 fm/V	1 ms
Simulation	Surface	1 nm	1 pm/V	100 ms
Simulation	Surface	9 nm	1 pm/V	1 ms

Table 3.1: **Summary of qubit lifetimes for a range of piezoelectricity assumptions** Using approaches given in section 3.5.1 and 3.5.2, we summarize the piezo-limited qubit T_1 for a range of piezoelectric assumptions.

short T_1 of $\sim$ 100 ns. Under bulk piezoelectricity assumption, even piezoelectricity as small as 10 fm/V limits qubit T_1 to 1 ms. In the latter case of thin piezoelectricity, simulation with $d_{33} = 1$ pm/V and $t_{pz} = 1$ nm predicts $T_1 \sim 100$ ms. Simulating for a relatively thin piezoelectric layer of $t_{pz} = 9$ nm, while keeping the piezo constant as $d_{33} = 1$ pm/V, results in $T_1 = 1$ ms. The summary of piezo-limited qubit lifetimes using analytical and simulation approaches is shown in table 3.1.

From the analysis in the previous paragraphs, it turns out that a very thin surface piezoelectric layer or a very weak bulk piezoelectricity can both limit the qubit lifetime. It only requires a moderate piezoelectric material with a thickness of $\sim$ 9 nm to limit the qubit T_1 to 1 ms. On the other hand, a very weak bulk piezoelectricity of 10 fm/V can likewise limit qubit T_1 to 1 ms. There is a study predicting surface piezoelectricity on sapphire, a widely used non-piezoelectric substrate for a qubit, from surface relaxation [34]. In fact, the study claims that the resulting surface piezoelectricity of sapphire may be comparable in strength to that of a typical bulk crystalline piezoelectric material. Moreover, there are many studies reporting anomalous piezoelectricity in non-piezoelectric bulk crystals [35–37]. The current upper limit in the state-of-the-art qubit lifetime is $T_1 \sim 0.3$ ms [79], and there are many ongoing efforts trying to find what is fundamentally limiting the qubit lifetime, from quasiparticles

to dielectric loss. Understanding and identifying anomalous piezoelectricity may help us get closer to understanding this fundamental limit since even a very weak piezoelectric source can limit the qubit lifetime to within an order of magnitude of the current limit.

Chapter 4

High-overtone bulk acoustic resonator (HBAR)

4.1 Introduction

Acoustic resonators with long-lived modes have played an important technological role, in applications ranging from precision metrology [80], to tests of fundamental physics [81], and to efficient quantum transducers [14]. For quantum applications, acoustic devices offer the promise of flexibly linking disparate quantum systems, through a wide variety of coupling pathways [82]. Mechanical resonators have achieved quantum-coherent coupling to systems ranging from optical and microwave cavities, to solid state defect centers, atomic ensembles, and superconducting qubits [3–5, 31, 83–85]. These advances relied on high quality-factor (Q) mechanical resonators, building on phononic engineering and low material dissipation at cryogenic temperatures [12, 13].

There are several aspects to consider while designing an acoustic cavity. In our design, we seek to utilize the strong optomechanical coupling at GHz frequencies provided through Brillouin interaction. As mentioned in chapter 2, Brillouin interaction

is a bulk process that is present in practically every bulk medium due to the ubiquitous nature of photoelasticity. Hence, our acoustic system should be applicable to a variety of crystal media, operate at GHz frequencies, be compatible with cryogenic temperatures, and have a long lifetime. Additionally, ease and reliability of fabrication are nice bonus qualities to have.

Among mechanical systems, high-overtone bulk acoustic resonators (HBARs), where high-frequency elastic standing waves are formed between polished surfaces of a crystalline substrate, offer a promising platform that satisfies the aforementioned requirements while achieving high acoustic Q-factors [56]. By design, these modes live primarily in the bulk, avoiding the loss typically associated with surface imperfections. Moreover, acoustic loss from phonon-phonon scattering plummets at cryogenic temperatures [56, 86, 87], offering an ideal environment for long-lived acoustic modes. Recent advancement in fabrication allows for chip-scale fabrications of such HBAR devices in a variety of materials, including quartz, silicon, sapphire, and calcium fluoride (CaF_2) [53]. It is also important to note that strong Brillouin optomechanical coupling between a Fabry-Pérot cavity and an HBAR [55], and strong piezo-electromechanical coupling between a superconducting qubit and an HBAR [7] have recently been demonstrated, making it appealing to explore a combined system of HBAR-mediated piezo-Brillouin system, which has not yet been built.

4.2 Loss mechanisms in HBAR

To begin with, it is informative to walk through the loss mechanisms that affect acoustic resonators. There are many factors that can lead to acoustic decoherence, such as thermal phonons, impurities, surface roughness, etc, which are well understood through various studies [88, 89]. Here, we explore the mechanisms for some of the notable loss channels that we consider in the design of our HBAR.

4.2.1 Phonon-phonon scattering

Phonon-phonon scattering is a dampening process between phonon modes and thermal phonons. This process occurs when thermal phonons present in a substrate lead to instantaneous local heating and cooling of resonant modes. Thermal phonons as a response react to maintain thermal equilibrium in such conditions, drawing energy from existing phonon modes. Here we consider two regimes in phonon-phonon scattering that are relevant to our system at low temperatures, known as the Akhiezer regime and the Landau-Rumer regime [88–90].

Akhiezer regime

We consider the Akhiezer regime when the frequency of the strain wave is at a much lower frequency than the thermal phonon lifetime, meaning that the thermal phonon lifetime is much shorter than the single oscillation of injected phonons, or the relaxation of thermal phonons is faster than the oscillation frequency of the strain wave. This condition is often described in terms of thermal phonon lifetime (τ_{th}) as, $\Omega_{\mathrm{m}}\tau_{\mathrm{th}} \ll 1$.

Interactions between acoustic phonons and thermal phonons can be described as follows. First, when strain fields exist in an acoustic substrate, the substrate undergoes temporal dilatation (dilatation is strain-induced volume change), which not only changes its volume but also its elastic constant. This leads to a shift in the normal mode frequency of the substrate, which is equivalent to a temporal fluctuation of mode temperature. As the modes are occupied by thermal phonons, mode temperature fluctuation drives a diffusive motion of thermal phonons in an attempt to restore thermal equilibrium, removing energy from the existing strain wave in the process. In this process, restoration of thermal equilibrium can occur only if the redistribution of thermal phonons, which is roughly equivalent to the thermal phonon lifetime, is faster than the strain field. Hence comes the condition $\Omega_{\mathrm{m}}\tau_{\mathrm{th}} \ll 1$.

To understand the rate at which strain field decays from phonon-phonon interaction, we start from Zener's model of anelastic solids [91], which provides a generalized version of Hook's stress-strain relation including rate terms.

$$\sigma + \tau_s \frac{d\sigma}{dt} = \bar{\bar{c}}_{\mathrm{R}} \left(s + \tau_\sigma \frac{ds}{dt} \right), \tag{4.1}$$

where $\bar{\bar{c}}_{\mathrm{R}}$ is the relaxed elastic modulus (or equivalently, Young's modulus or stiffness constant) and τ_σ (τ_s) is the time constant correlated with stress (strain) variation. Relaxed modulus is defined as the stress-strain relation that is slow in time, while the modulus acting on fast oscillating stress and strain is called the unrelaxed modulus. Considering time harmonic stress ($\sigma = \sigma_0 e^{i\Omega t}$) and strain ($s = s_0 e^{i\Omega t}$) at frequency Ω, we can express the relaxed and unrelaxed moduli in terms of other variables. With low frequency assumption ($\Omega \ll 1/\tau_\sigma, 1/\tau_s$), equation 4.1 gives $\sigma_0 = \bar{\bar{c}}_{\mathrm{R}} s_0$, consistent with our definition of relaxed modulus. Meanwhile with high frequency assumption ($\Omega \gg 1/\tau_\sigma, 1/\tau_s$), we obtain $\sigma_0 = \bar{\bar{c}}_{\mathrm{U}} s_0 = (\bar{\bar{c}}_{\mathrm{R}} \tau_\sigma / \tau_s) s_0$, giving the unrelaxed modulus $\bar{\bar{c}}_{\mathrm{U}} = \bar{\bar{c}}_{\mathrm{R}} \tau_\sigma / \tau_s$.

Solving equation 4.1 in the generic case in terms of frequency-dependent elastic modulus provides us with both the real part and the imaginary part of the elastic modulus, where the imaginary part represents the loss rate of the strain field.

$$\begin{aligned} \sigma_0 e^{i\Omega t} + \tau_s \frac{d}{dt} \sigma_0 e^{i\Omega t} &= \bar{\bar{c}}_{\mathrm{R}} \left(s_0 e^{i\Omega t} + \tau_\sigma \frac{d}{dt} s_0 e^{i\Omega t} \right) \\ \sigma_0 &= \bar{\bar{c}}_{\mathrm{eff}}(\Omega) \left(1 + i \frac{\Omega \bar{\tau} \Delta}{1 + \Omega^2 \bar{\tau}^2} \right) s_0, \end{aligned} \tag{4.2}$$

where $\bar{\bar{c}}_{\mathrm{eff}}(\Omega) = \bar{\bar{c}}_{\mathrm{R}} \frac{1+\Omega^2 \tau_\sigma \tau_s}{1+\Omega^2 \tau_s^2}$, $\bar{\tau} = \sqrt{\tau_\sigma \tau_s}$, and Δ is given as, $\Delta \bar{\bar{c}}_{\mathrm{R}} = \bar{\bar{c}}_{\mathrm{U}} - \bar{\bar{c}}_{\mathrm{R}}$. A quality factor ($Q$) of the strain field can be defined from the ratio between the real part and the imaginary part of the strain in the above expression,

$$\frac{1}{Q} = \frac{\Omega \bar{\tau} \Delta}{1 + \Omega^2 \bar{\tau}^2}. \tag{4.3}$$

To properly express acoustic loss rate due to thermal phonons, we can rearrange equation 4.3 as,

$$\frac{1}{Q} = \frac{|\bar{\bar{c}}_{\mathrm{U}} - \bar{\bar{c}}_{\mathrm{R}}|}{|\bar{\bar{c}}_{\mathrm{R}}|} \frac{\Omega\tau_{\mathrm{th}}}{1 + \Omega^2\tau_{\mathrm{th}}^2}, \tag{4.4}$$

where mean relaxation time $\bar{\tau}$ is replaced with τ_{th}, the difference between the unrelaxed and relaxed modulus is given as [92], $|\bar{\bar{c}}_{\mathrm{U}} - \bar{\bar{c}}_{\mathrm{R}}| = \gamma^2 c_{\mathrm{V}} T$, γ is the Gruneisen parameter, c_{V} is the volumetric specific heat capacity, and T is the absolute temperature. Also, the thermal relaxation time, τ_{th}, is given in reference [93] as $\tau_{\mathrm{th}} = 3\kappa/c_{\mathrm{V}} v_{\mathrm{m}}^2$, where κ is the thermal conductivity. Hence, the acoustic quality factor and dissipation rate in Akhiezer regime at phonon frequency Ω_{m} and temperature T can be written as,

$$Q_{\mathrm{Akhiezer}} = \frac{\rho v_{\mathrm{m}}^2}{\gamma^2 c_{\mathrm{V}} T} \frac{1 + \Omega_{\mathrm{m}}^2 \tau_{\mathrm{th}}^2}{\Omega_{\mathrm{m}} \tau_{\mathrm{th}}} = \frac{\Omega_{\mathrm{m}}}{\Gamma_{\mathrm{Akhiezer}}}. \tag{4.5}$$

More thorough derivation and further discussions of the Akhiezer regime can be found in literature, such as reference [88].

Landau-Rumer regime

When the oscillation frequency of a strain wave is faster than the relaxation of thermal phonons, the acoustic system is in the Landau-Rumer regime. This means that in the presence of normal mode temperature fluctuations due to strain fields, thermal phonons cannot diffuse fast enough to retain thermal equilibrium. The condition can be described in terms of thermal phonon lifetime as, $\Omega_{\mathrm{m}}\tau_{\mathrm{th}} > 1$, and it is generally satisfied at high acoustic frequencies or at low temperatures.

In such a regime, Landau and Rumer described the scattering process as a three-phonon process between incoming phonon and thermal phonon satisfying energy and momentum conservation [90, 94]. This lead to the corresponding quality factor expression,

$$Q_{\mathrm{LR}} = \frac{120\rho v_{\mathrm{m}}^5 \hbar^3}{\pi^2 \gamma^2 k_{\mathrm{B}}^4} \frac{1}{T^4} = \frac{\Omega_{\mathrm{m}}}{\Gamma_{\mathrm{LR}}}, \tag{4.6}$$

where k_B is the Boltzmann constant. Note that, this expression is specific to cubic and isotropic materials. In trigonal crystals, the temperature dependence becomes $\propto T^{-6.5}$ [86]. Compared to the expression from the Akhiezer regime (equation 4.5), the expression for the Landau-Rumer regime (equation 4.6) has a strong temperature dependence. Many acoustic devices to date leverage this strong temperature dependence of acoustic Q and the low-temperature condition required for an acoustic system to be in the Landau-Rumer regime to design high Q acoustic devices operating in cryogenic conditions.

4.2.2 Impurity scattering

Scattering of phonons from crystal impurities or point defects is another source of phonon loss. This type of loss can be caused by any element that contributes to the variation in atomic mass of the crystal, such as impurities in the substrate, dopant ions, and even mass variations in isotopes [88].

In order to obtain the rate of phonon loss, we should treat the variations in atomic mass within the crystal lattice structure as perturbations from which phonons scatter off. The Hamiltonian of such a system can be written as,

$$H = H_0 + \Delta H, \tag{4.7}$$

where ΔH is the perturbative term from impurities. For a perfect crystal, Hamiltonian H_0 is,

$$H_0 = \sum \frac{p^2}{2M} + H_{\text{int}}, \tag{4.8}$$

where p is the atomic momentum operator and M is the atomic mass. Here, the first term is the kinetic energy term and the second term is the interaction potential term between atoms independent of local atomic mass. Replacing crystal atomic mass (M) with the atomic mass of impurities ($M - \Delta M$) in the H_0 Hamiltonian, we obtain the

perturbative term from atomic mass variation,

$$\Delta H \approx \frac{\Delta M}{M} \frac{p^2}{2M}. \tag{4.9}$$

To solve the phonon scattering rate, we apply the perturbation Hamiltonian to Fermi's golden rule,

$$\Gamma_{i \to f} = \frac{2\pi}{\hbar} \left| \langle f | \Delta H | i \rangle \right|^2 \delta(E_f - E_i), \tag{4.10}$$

that describes the scattering fate from the initial state i to the final state f. We desire to calculate the scattering rate of a single phonon. Hence, we set the initial state as a single phonon state, and the final state as a state that is in thermal equilibrium with the substrate at temperature T, whose occupation follows the Bose-Einstein distribution. Decomposing the momentum operator in ΔH in terms of normal mode momenta, we find the impurity scattering rate for a single phonon,

$$\Gamma_{\text{impurity}} = \frac{1}{4\pi n v_{\text{m}}^3} \left(\frac{n_{\text{d}}}{n} \right) \left(\frac{\Delta M}{M} \right)^2 \frac{\Omega_{\text{m}}^4}{1 - e^{-\frac{\hbar \Omega_{\text{m}}}{k_{\text{B}} T}}} = \frac{\Omega_{\text{m}}}{Q_{\text{impurity}}}, \tag{4.11}$$

where n (n_{d}) here is the atomic density (defect density). See reference [88] for a more detailed derivation.

4.2.3 Two-level systems

Defect sites in solids can affect phonon coherence by not only directly scattering phonons but also generating two-level systems (TLS) that can interact with phonons to induce dissipation [95–97]. TLS is a system with two states (often denoted as the ground state and the excited state) that can exist in superposition. Defect sites of a crystal can lead to TLS generation if two local arrangements of atoms arse nearly degenerate in energy, effectively possessing a quantized energy spectrum. These defect states can be phonon-active, meaning that they can exchange energy with phonons.

Although phonon-active TLSs are mostly studied in the context of amorphous media, they also exist in crystalline substrates and are suspected as one of the limiting factors of acoustic lifetimes in highest Q acoustic devices [12, 56]. Effects of TLS usually become prominent at low temperatures ($\hbar\Omega \gg k_{\mathrm{B}}T$) and are suppressed at high temperatures ($\hbar\Omega \ll k_{\mathrm{B}}T$). This is because TLSs are mostly in their ground states at low temperatures, allowing for phonon absorption and subsequent dissipation to occur. Meanwhile, at high temperatures, TLSs are mostly saturated, or in excited states, not allowing for such phonon absorption processes.

In this section, we first work out the excited state lifetime of a TLS. Then, we consider acoustic dissipation from resonant TLS coupling in the weak and strong acoustic field regimes, followed by acoustic loss from the relaxation absorption process.

TLS excited state lifetime

TLS in a crystal can be thought of as a tunneling state of a double well potential with asymmetry Δ and tunneling strength Δ_0, such that the energy splitting between the excited state and the ground state is $E_{\mathrm{TLS}} = \sqrt{\Delta^2 + \Delta_0^2}$. An excited state of a TLS can decay into its ground state, releasing energy into a phonon bath. The Hamiltonian of a corresponding TLS-phonon coupled system is given as following [95, 96],

$$H = \hbar\Omega \left(b^\dagger b + \frac{1}{2} \right) + \frac{1}{2}(E_{\mathrm{TLS}} + D \cdot s(\bar{x}))\sigma_z + M \cdot s(\bar{x})\sigma_x, \tag{4.12}$$

where longitudinal coupling potential is $D = 2\frac{\Delta}{E_{\mathrm{TLS}}}$, transverse coupling potential is $M = \frac{\Delta_0}{E_{\mathrm{TLS}}}\gamma$, and deformation potential constant is $\gamma = \frac{1}{2}\frac{\partial\Delta}{\partial s}$. Using Fermi's golden rule (or time-dependent perturbation theory), we can write the TLS transition rate,

$$\Gamma^{\mathrm{TLS}}_{e\to g} = \frac{2\pi}{\hbar} \left| \langle g | H_{\mathrm{int}} | e \rangle \right|^2 g(E_{\mathrm{TLS}}) n_{\mathrm{B}}(E_{\mathrm{TLS}}), \tag{4.13}$$

where the Debye density of phonon states is $g(E_{\mathrm{TLS}}) = E_{\mathrm{TLS}}/2\pi^2\hbar^3 v_{\mathrm{m}}^3$, the Bose distribution $n_{\mathrm{B}}(E_{\mathrm{TLS}}) = 1/(e^{E_{\mathrm{TLS}}/k_{\mathrm{B}}T} - 1)$, and the interaction term is $|\langle g| H_{\mathrm{int}} |e\rangle|^2 = |M \cdot s(\bar{x})|^2$. In thermal equilibrium at temperature T, the rate at which the TLS excited state transitions into the ground state should be equal to the process in the other direction, giving the relation between TLS occupation probability (p_e^{TLS} for excited state and p_g^{TLS} for ground state occupation probability) and TLS transition rate, $p_e^{\mathrm{TLS}}\Gamma_{e\to g}^{\mathrm{TLS}} = p_g^{\mathrm{TLS}}\Gamma_{g\to e}^{\mathrm{TLS}}$. From this, we get the TLS relaxation rate ($\Gamma_{\mathrm{m}}^{\mathrm{TLS}}$), at which the initial state of TLS deviates,

$$\Gamma_{\mathrm{m}}^{\mathrm{TLS}} = \Gamma_{e\to g}^{\mathrm{TLS}} \left(1 + e^{\frac{E_{\mathrm{TLS}}}{k_{\mathrm{B}}T}}\right). \tag{4.14}$$

Combining this expression with equation 4.13, we obtain the phonon-induced TLS relaxation rate of,

$$\Gamma_{\mathrm{m}}^{\mathrm{TLS}} = \frac{\gamma^2 \Delta_0^2 E_{\mathrm{TLS}}}{2\pi\rho\hbar^4 v_{\mathrm{m}}^5} \coth\left(\frac{E_{\mathrm{TLS}}}{2k_{\mathrm{B}}T}\right) \tag{4.15}$$

Resonant TLS damping in weak acoustic fields

We now reverse roles such that TLS is a dissipative channel phonons decay into. We first consider the regime of weak acoustic fields, where the mean free time between TLS-phonon interactions is much longer compared to the TLS excited state lifetime. Here, TLSs attenuate acoustic waves through resonant absorption, meaning that TLSs in the ground state absorb phonon to be resonantly excited into their excited state. This type of interaction is mediated via the σ_x term in the Hamiltonian (equation 4.12). (Note that the σ_z term is discussed in the later section on relaxation absorption.)

For weak acoustic fields, the phonon damping rate from TLS resonant absorption can be obtained through Fermi's golden rule,

$$\Gamma_{\mathrm{TLS}}^{\mathrm{weak}} = \frac{2\pi}{\hbar} |\langle e, n_{\mathrm{m}} - 1| H_{\mathrm{int}} |g, n_{\mathrm{m}}\rangle|^2 P(p_g^{\mathrm{TLS}} - p_e^{\mathrm{TLS}}), \tag{4.16}$$

where P is the TLS density of states, the interaction term is $|\langle e, n_{\mathrm{m}} - 1| H_{\mathrm{int}} |g, n_{\mathrm{m}}\rangle|^2 = |M \cdot s(\bar{x})|^2$, and the difference between the TLS occupation probabilities is $p_g^{\mathrm{TLS}} - p_e^{\mathrm{TLS}} = \tanh\left(\frac{E_{\mathrm{TLS}}}{2k_{\mathrm{B}}T}\right)$. Solving the above equation, we end up with an expression for phonon dissipation rate due to TLS damping in weak acoustic fields, given as,

$$\Gamma_{\mathrm{TLS}}^{\mathrm{weak}} = \frac{\pi\gamma^2 P\Omega}{\rho v_{\mathrm{m}}^2}\tanh\left(\frac{\hbar\Omega}{2k_{\mathrm{B}}T}\right), \tag{4.17}$$

where the TLS transition energy is set equal to the phonon energy ($E_{\mathrm{TLS}} = \hbar\Omega$). Note that the decay rate is maximized at low temperature ($\hbar\Omega \gg k_{\mathrm{B}}T$) and suppressed at high temperature ($\hbar\Omega \ll k_{\mathrm{B}}T$). This is because, at low temperatures, TLSs are found mostly in their ground state, resulting in the resonant absorption term ($p_g^{\mathrm{TLS}} \sim 1, p_e^{\mathrm{TLS}} \sim 0$) to dominate. On the other hand, stimulated emission from TLS that coherently amplifies the acoustic field can occur at high temperatures, which suppresses the resonant absorption process and subsequently minimizes the decay rate.

Resonant TLS damping in strong acoustic fields

In the regime of strong acoustic fields, we can no longer use the perturbation theory approach to calculate the dissipation rate. Instead, we solve the Heisenberg equation of motion to obtain the TLS-induced phonon dissipation rate at high acoustic fields, which gives an expression similar to the weak acoustic field case with an addition of an acoustic intensity ratio term [95, 96],

$$\Gamma_{\mathrm{TLS}}^{\mathrm{strong}} \approx \frac{\pi\gamma^2 P\Omega}{\rho v_{\mathrm{m}}^2}\tanh\left(\frac{\hbar\Omega}{2k_{\mathrm{B}}T}\right)\frac{1}{\sqrt{1 + J/J_{\mathrm{c}}}}, \tag{4.18}$$

where J is the acoustic intensity and J_{c} ($J_{\mathrm{c}} \approx \rho\hbar^2 v^3/2\gamma^2 T_1^{\mathrm{TLS}} T_2^{\mathrm{TLS}}$) is the critical intensity defining the strong/weak acoustic field regimes.

Relaxation absorption

Another mechanism through which TLS can induce phonon decoherence is relaxation absorption. This is a process in which TLS's energy splitting experiences a modulation due to a time-dependent strain field, resulting in TLS constantly absorbing and releasing energy into the phonon bath environment. Recalling the TLS-phonon Hamiltonian (equation 4.12), the process is represented in the σ_z term ($\frac{1}{2}(E_{\mathrm{TLS}} + D \cdot s(\bar{x}))$), and the corresponding phonon decay rate is given as [95, 96],

$$\Gamma_{\mathrm{TLS}}^{\mathrm{relax}} = \frac{\pi^3}{24} \frac{P\gamma^2}{\rho^2 v_{\mathrm{m}}^2 \hbar^4} \left(\sum_{\mathrm{pol}} \frac{\gamma^2}{v_{\mathrm{m}}^5} \right) k_{\mathrm{B}}^3 T^3, \tag{4.19}$$

where $\sum_{\mathrm{pol}}$ represents a sum over all strain field polarizations.

4.2.4 Diffraction

Besides the type of phonon decoherences originating internally within substrates, consequently being heavily dependent on material properties, there are other mechanisms through which phonons can lose energy, such as through geometrical properties and surface properties of the substrate.

The design of an HBAR closely follows that of an optical Fabry-Pérot cavity with Hermite-Gaussian-like acoustic mode profiles driven via Gaussian optical beams [7, 53–56]. Consequently, an HBAR has to satisfy stability criteria, similar to that of an optical Fabry-Pérot cavity, to produce stable cavity modes. This is given as,

$$0 \leq g_1 g_2 \leq 1, \tag{4.20}$$

where g_1 (g_2) is the stability parameter of the front (back) surface of an HBAR. The acoustic stability parameter that takes into account the anisotropy of elastic constants

is given as [53],

$$g_{1(2)} = 1 - \frac{L_{\mathrm{m}}}{\chi R_{1(2)}}, \tag{4.21}$$

$$\chi = \frac{v_l^2(v_l^2 - v_t^2)}{v_l^2 v_t^2 - v_t^4 + \gamma_1^4}, \tag{4.22}$$

where χ is the anisotropy constant, R is the radius of curvature of the surface, $v_l = \sqrt{c_{11}/\rho}$ is longitudinal acoustic velocity, $v_t = \sqrt{c_{44}/\rho}$ is transverse acoustic velocity, and $\gamma_1 = \sqrt{(c_{12} + c_{44})/\rho}$. Combining equations 4.20 and 4.21, we get the condition $0 \leq (1 - L_{\mathrm{m}}/\chi R_1)(1 - L_{\mathrm{m}}/\chi R_2) \leq 1$, for a stable HBAR. Typically, an HBAR is made from a plano-convex geometry, where one side of a crystal is flat ($g_2 = 1$) and the other side is convex ($g_1 = 1 - L_{\mathrm{m}}/\chi R_1$), giving a simplified condition,

$$0 \leq 1 - L_{\mathrm{m}}/\chi R_1 \leq 1. \tag{4.23}$$

Mode waist radius of Gaussian acoustic wave can also be expressed in terms of the stability parameters as [53],

$$w_0 = \frac{L_{\mathrm{m}}\lambda_{\mathrm{m}}}{\chi\pi}\sqrt{\frac{g_1 g_2(1 - g_1 g_2)}{(g_1 + g_2 - 2g_1 g_2)^2}}. \tag{4.24}$$

When we consider the diffractive loss of an HBAR, it is conventional to imagine an HBAR with a flat-flat geometry, where both sides of the crystal have no curvature ($R_1, R_2 = \infty$). In this type of HBARs, acoustic mode waists are not well defined due to unity stability parameters ($g_1, g_2 = 1$) and the modes are unstable. The diffraction of acoustic beams makes them walk off from their initial mode profile, resulting in dissipation.

Gaussian beam propagation

There are a couple of different approaches we can take to calculate the diffractive loss in a flat-flat HBAR. The first method is to observe the Gaussian wave propagation

along the crystal and compare it with its initial profile. The expression for Gaussian beam propagation of acoustic displacement field along z-direction is given as [53],

$$u(r,z) = u_0 \frac{w_0}{w(z)} e^{-\frac{r^2}{w(z)^2}} e^{-i\left(kz + k\frac{r^2}{2R(z)} - \psi(z)\right)}, \tag{4.25}$$

where $w(z)$ is the beam waist radius at position z, $R(z)$ is the radius of curvature of the beamfronts at z, and $\psi(z)$ is the acoustic Gouy phase. We can calculate the overlap of the displacement field at the initial position ($z = 0$) and at z through the expression [54],

$$|\eta(z)|^2 = \frac{|\int u(r,z) \cdot u(r,0) dA|^2}{|\int u(r,0) \cdot u(r,0) dA|^2}, \tag{4.26}$$

where the denominator is for normalization. The relation between beam waist and the Rayleigh length z_{R} is,

$$\frac{w(z)}{w_0} = \sqrt{1 + \left(\frac{z}{z_{\mathrm{R}}}\right)^2}, \tag{4.27}$$

where the acoustic Rayleigh length is given as,

$$z_{\mathrm{R}} = \frac{\pi w_0^2}{\lambda_{\mathrm{m}}} \chi. \tag{4.28}$$

Putting together equations 4.28, 4.27, and 4.26, we can simplify the overlap described in equation 4.26 as,

$$|\eta(z)|^2 = 4 \frac{1 + \left(\frac{z}{z_{\mathrm{R}}}\right)^2}{\left(2 + \left(\frac{z}{z_{\mathrm{R}}}\right)^2\right)^2}. \tag{4.29}$$

We can define a distance at which propagating phonons lose energy to, or have mode overlap of, e^{-1} of their initial value. Let's call it an acoustic coherence (attenuation) length Λ, analogous to the optical coherence length. Setting $|\eta(\Lambda)|^2$ from equation 4.29 equal to e^{-1}, we obtain the acoustic coherence length and the corresponding

decoherence rate,

$$\begin{aligned} \Lambda &= 2.785 z_{\mathrm{R}} \\ \Gamma_{\mathrm{diffract}} &= \frac{v_{\mathrm{m}}}{\Lambda} = \frac{v_{\mathrm{m}}}{2.785 z_{\mathrm{R}}}. \end{aligned} \tag{4.30}$$

However, note that equation 4.29 is not exponential in x, thus one has to be cautious in using $\Gamma_{\mathrm{diffract}}$ from equation 4.30 and treat it as an estimate.

Bessel mode decomposition and time evolution

An alternative approach in calculating diffractive loss in a flat-flat HBAR involves decomposing the initial phonon mode into Bessel modes and observing their time evolution [54]. Since the acoustic mode waist is not well defined in a flat-flat HBAR, here we assume that the initial acoustic displacement profile at time $t = 0$ follows the Gaussian profile of optical electrostrictive drive from Brillouin scattering,

$$u_m(r, z, t = 0) = u_0 e^{-\frac{2r^2}{r_{\mathrm{opt}}^2}} \cos\left(\frac{m\pi}{L_{\mathrm{m}}} z\right), \tag{4.31}$$

where r_{opt} is the optical beam waist radius and m is the overtone number in longitudinal direction. The initial acoustic profile can then be decomposed into the eigenmodes of the acoustic cavity and put through a time evolution, shown as,

$$u(r, z, t) = \sum_{m,n} c_{m,n} u_{m,n}(r, z) e^{-i\omega_{m,n} t}, \tag{4.32}$$

where n is the transverse mode number, coefficient $c_{m,n}$s are determined by the initial profile, and $u_{m,n}(r, z)$s are the eigenmodes with corresponding frequency $\omega_{m,n}$. For a cylindrical HBAR, the acoustic modes of the cavity can be written in terms of the Bessel functions,

$$u_{m,n}(r, z) = \beta_{m,n} \cos\left(\frac{m\pi}{L_{\mathrm{m}}} z\right) J_0\left(\frac{j_{0,n} r}{r_{\mathrm{c}}}\right), \tag{4.33}$$

where $\beta_{m,n}$ is the normalization constant, J_0 is the zeroth order Bessel function of the first kind, $j_{0,n}$ is the n^{th} root of J_0, and r_c is the radius of the cylindrical crystal substrate. Also, the frequency $\omega_{m,n}$ of an acoustic mode $u_{m,n}(r,z)$ is,

$$\omega_{m,n} = \sqrt{\left(\frac{m\pi}{L_\text{m}}\right)^2 v_l^2 + \left(\frac{j_{0,n}}{r_\text{c}}\right)^2 v_t^2}. \tag{4.34}$$

To analyze the acoustic energy dissipated from the initial state as the acoustic modes evolve in time, we can calculate the overlap of time-evolved acoustic modes at time t with their initial state [54],

$$\begin{aligned} |\eta(t)|^2 &= \frac{|\int u(r,z,t)\cdot u(r,z,0)dV|^2}{|\int u(r,z,0)\cdot u(r,z,0)dV|^2} \\ &= \frac{|\sum_n |c_{m,n}|^2 e^{i\omega_{m,n}t}|^2}{|\sum_n |c_{m,n}|^2|^2}. \end{aligned} \tag{4.35}$$

With $|\eta(t)|^2$, the acoustic coherence time (τ'_diffract) and dissipation rate (Γ'_diffract) from diffraction can be obtained from solving,

$$|\eta(\tau'_\text{diffract})|^2 = e^{-1}, \tag{4.36}$$

and subsequently from $\Gamma'_\text{diffract} = 1/\tau'_\text{diffract}$.

4.2.5 Anchoring loss

When placing an HBAR in an experimental setup, there is also a practical concern that we need to take into account. As an acoustic device is clamped in place, direct mechanical couplings between phonon modes and lossy outside environment at the clamping points can lead to anchoring loss or clamping loss [53].

Similar to the previous section on diffraction, the main mode of interest in a plano-convex HBAR is its fundamental Gaussian mode, whose displacement profile along

z-direction is described as,

$$u_n(r,z) = u_0 e^{-\frac{r^2}{r_{\mathrm{m}}^2}} \cos\left(\frac{m\pi}{L_{\mathrm{m}}} z\right), \tag{4.37}$$

where r_{m} is acoustic mode waist radius (equivalent to w_0 from section 4.2.4) and m is the overtone number in longitudinal direction. Assuming that all of the acoustic energy that exists outside a certain distance r_{anchor} away from the center of the plano-convex HBAR is lost during a single round-trip, we can calculate the fraction of the energy loss in a single round-trip,

$$\frac{E_{\mathrm{lost}}}{E_{\mathrm{tot}}} = \frac{\int_{V_{\mathrm{out}}} |u_n(r,z)|^2 dV}{\int_{V_{\mathrm{tot}}} |u_n(r,z)|^2 dV} = e^{-\frac{2r_{\mathrm{anchor}}^2}{r_{\mathrm{m}}^2}}. \tag{4.38}$$

Equating the remaining energy, $R = 1 - E_{\mathrm{lost}}/E_{\mathrm{tot}}$, with $e^{-\Gamma_{\mathrm{anchor}} t}$, where $t = 2L_{\mathrm{m}}/v_{\mathrm{m}}$ is the round-trip time, we can obtain the acoustic loss rate and the corresponding acoustic Q from anchoring at distance r_{anchor},

$$\Gamma_{\mathrm{anchor}} = -\frac{v_{\mathrm{m}} \ln(R)}{2L_{\mathrm{m}}} = \frac{\Omega_{\mathrm{m}}}{Q_{\mathrm{anchor}}}. \tag{4.39}$$

Note that this is a simplistic model that does not take into account the additional stress exerted at the anchoring points and the deformation of acoustic modes that subsequently follows. These can contribute to acoustic loss even further.

4.2.6 Surface roughness

In an optical Fabry-Pérot cavity, rough mirrors with low reflectivities can limit the cavity lifetime. Likewise in an HBAR, which is analogous to an acoustic Fabry-Pérot cavity, roughness on the surface of a crystal can lead to acoustic loss. Assuming a Gaussian distribution of surface roughness, phonon reflectivity from a surface can be

expressed as [56],

$$R = e^{-8\pi^2\sigma^2/\lambda_{\mathrm{m}}^2}, \tag{4.40}$$

where σ is the surface roughness variance. Equating the product of reflectivities from both surfaces of a crystal to the phonon loss after one round-trip ($e^{-\Gamma_{\mathrm{rough}}t_{\mathrm{RT}}} = e^{-8\pi^2(\sigma_1^2+\sigma_2^2)/\lambda_{\mathrm{m}}^2}$), and assuming both surfaces of the crystal have identical roughness ($\sigma_1 = \sigma_2$), we obtain the phonon decay rate from surface roughness.

$$\Gamma_{\mathrm{rough}} = \frac{\Omega_{\mathrm{m}}^2\sigma^2}{v_{\mathrm{m}}L_{\mathrm{m}}} = \frac{\Omega_{\mathrm{m}}}{Q_{\mathrm{rough}}}. \tag{4.41}$$

4.2.7 Deposition layer on crystal

When designing an HBAR, it is sometimes necessary to have a deposited layer on top of the device depending on its purpose. For instance, a layer of metal electrodes can be deposited for direct electromechanical coupling to the device [98]. Additionally, the integration of a multi-layer dielectric mirror coating with high reflectivity may be an appealing way to realize optomechanical coupling.

Assuming that the interface loss is negligible, mechanical devices with thin layer coating have quality factor given as [98–100],

$$Q_{\mathrm{composite}}^{-1} = Q_{\mathrm{s}}^{-1} + \eta Q_{\mathrm{c}}^{-1}, \tag{4.42}$$

where η is the energy participation ratio ($\eta = E_{\mathrm{c}}/E_{\mathrm{s}}$) and subscript $s(c)$ indicates the value for the substrate (coating layer). For an isotropic substrate with Poissons's ratio much lower than unity and for thin films ($t_{\mathrm{c}} \ll t_{\mathrm{s}}$), this energy participation ratio can be simplified to $\eta = 3t_{\mathrm{c}}Y_{\mathrm{c}}/t_{\mathrm{s}}Y_{\mathrm{s}}$ [98–100], where Y is Young's modulus of a material. Also note that for multi-layer coating, Y_{c} is taken as the weighted average of Young's modulus of deposited materials, $Y_{\mathrm{c}} \approx \frac{\sum_i t_{\mathrm{c,i}}Y_{\mathrm{c,i}}}{\sum_j t_{\mathrm{c,j}}}$.

4.3 Identification of acoustic dissipation

Now that we have laid out the theoretical background for possible sources of acoustic dissipation, we discuss how it is observed experimentally. Experimental implementation of phonon characterization is detailed in section 5.2.3. To give an overview of the method, the Brillouin interaction (introduced in chapter 2) is used to probe the acoustic properties of materials. As illustrated in figure 2.3(b), optical light is sent into a BAR to probe the phonon modes. In addition to the pump light, a counter-propagating probe light is also provided to electrostrictively drive the phonons [52], which is an inverse process of photoelasticity. Detecting the scattered light from phonons, we observe the phonon spectrum following figure 2.1(b) and figure 4.2, from which we can record the phonon mode frequency, Ω_{m}, and dissipation, Γ.

In this section, we apply the dissipation models established in the previous section to analytically predict the loss rates in relevant acoustic materials (i.e. x-cut quartz and Si) and device designs (i.e. plano-convex and flat-flat geometry) for our experiment. In the following section 4.4, we further discuss the fabrication and preparation of HBAR acoustic devices.

4.3.1 Loss value calculations on relevant materials

Plano-convex geometry

Using the material constant values at room temperature, we find the acoustic dissipation from phonon-phonon scattering, which is in the Akhiezer regime, to be well over 1 MHz at the Brillouin-active frequencies of x-cut quartz and Si. Even without any other sources of dissipation, this is already a major factor limiting the accessibility to high-Q HBARs at room temperatures.

At cryogenic temperatures (< 10 K), on the other hand, thermal relaxation time (τ_{th}) becomes greatly enhanced, thus bringing both x-cut quartz and Si well into the

Landau-Rumer regime ($\Omega_{\mathrm{m}}\tau_{\mathrm{th}} > 1$). Solving equation 4.6, we obtain substantially lower dissipation rates of 190 Hz for x-cut quartz and 5 Hz for Si. This opens up the utilization of high-Q HBARs at cryogenic temperatures and motivates further investigation into additional sources of loss that may affect total acoustic dissipation.

TLS effects, on the other hand, are suppressed ($\hbar\Omega \ll k_{\mathrm{B}}T$) at the temperature and frequency range we operate ($10 \sim 50$ GHz, $5 \sim 10$ K).

The quartz substrates we use in our experiment are from MTI, graded as optical grade single-crystal with 99.99% purity. Since the vendor does not specify the impurities in the substrate, we have to make an assumption about the composition of impurities. Nominally, impurities in quartz consist of iron, aluminum, potassium, calcium, and sodium. Although iron is known to be the most common impurity in quartz, we assume sodium to be the only impurity here since it gives the largest n_{d} and ΔM, resulting in a more conservative value for $\Gamma_{\mathrm{impurity}}$. Additionally, we assume that the crystal purity is 99.9% to be conservative. Solving for $\Gamma_{\mathrm{impurity}}$ following equation 4.11, we obtain $\Gamma_{\mathrm{impurity}} = 2$ Hz at 10 K.

For Si, we use float-zone, high resistivity, N-type Si of R $>$ 10000 Ω as high resistivity is correlated to high purity. We consider impurity loss contribution from Si isotope with 29 atomic mass, which occurs at a rate of 4.67% in nature, phosphorous with concentration calculated from the resistivity value, oxygen, and carbon with concentration observed through x-ray diffraction analysis (XRD). Combined, impurities in Si give a loss rate of ~ 1.2 Hz at 10 K.

In both quartz and Si, we can calculate the clipping loss from equation 4.39 for our common design parameters (provided in section 4.4) of ~ 50 μm acoustic mode waist with device size of ~ 500 μm radius. Assuming full dissipation of acoustic waves outside of the device diameter, the clipping loss for a perfect plano-convex resonator turns out to be minimal (< 1 Hz).

We believe that a dominant contributor to acoustic loss at cryogenic temperatures

turns out to be surface roughness loss. Several of the high-Q HBAR studies have reported that their devices' Q-factors are limited by surface roughness [53, 56]. For the device parameters used for our design and a reasonable roughness of 1 nm which we often observe in our devices through AFM and Zygo measurements, we expect surface roughness induced loss from equation 4.41 is 300 Hz for quartz and 1 kHz for Si, which is indeed the highest loss contribution of all the factors we have considered so far. With adequate process and careful optimization, we can reduce the surface roughness to a sub-Å level [101].

Flat-flat geometry

Diffraction loss becomes relevant only for a flat-flat HBAR geometry. Using the model presented in section 4.2.4, we get a dissipation rate in the range of 10 to 100 kHz. However, other detrimental factors, such as the instability of the acoustic modes in flat-flat geometry and the bunching of higher-order transverse modes, can further contribute to an effective broadening of the acoustic linewidth. Indeed, later in chapter 6 and 7, we observe the linewidth of a flat-flat HBAR to be in the range of 300 - 500 kHz, which we attribute to diffractive loss. In order to avoid this, we have previously developed a technique of fabricating a plano-convex HBAR with flexible design parameters, forming a stable resonator and completely avoiding the diffractive loss [53].

4.4 On-chip HBAR devices

HBARs support longitudinal acoustic standing waves between the two faces of a crystalline substrate, forming Fabry-Pérot-like acoustic modes. As the mode predominantly lives in the bulk, they have greatly reduced surface interactions, which allows suppression of surface-originating acoustic loss and robustness thermal prop-

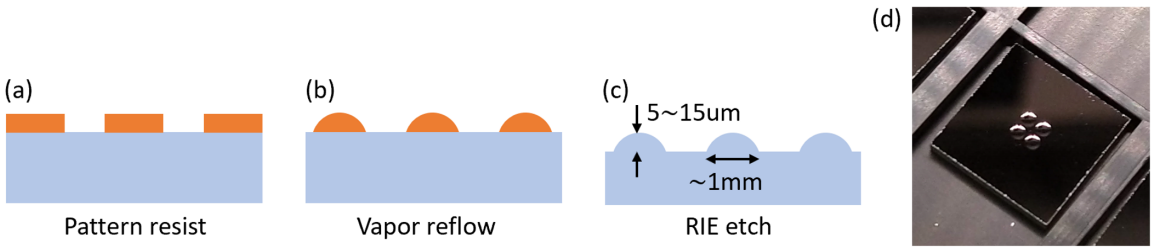

Figure 4.1: **On-chip HBAR fabrication** (a-c) Procedures for on-chip HBAR fabrication. After the initial cleaning and conditioning of a substrate wafer, circular resist patterns are developed. Then, dome-like structures are formed by carefully controlled and monitored vapor reflow of the resist. Reactive ion etch (RIE) transfers this pattern onto the substrate, resulting in an on-chip plano-convex HBAR. (d) Picture of a set of four HBAR devices made on a 1 mm thick Si wafer. HBARs shown have 1 mm diameter with 12 μm height.

erties. There are works taking advantage of such properties, where they demonstrate Q-factors in an HBAR reaching 10^7 (10^9) at GHz (MHz) frequencies [53, 56], and achieve strong optomechanical coupling between an HBAR and a Fabry-Pérot cavity by linearizing the interaction around a strong optical pump [55].

Previously, designs of such high-Q HBARs were limited to cm-scale dimensions. Recent work from our group allows on-chip fabrication of high-Q HBARS in the mm-scale and even μm-scale dimensions [53]. The HBAR devices fabricated for our experiments are made closely following the method laid out in reference [53] with minor adaptations. In the subsequent sections, we discuss how HBARs are fabricated along with some notable observations we made along the way.

4.4.1 Fabrication steps

In order to create plano-convex HBARs, we start by preparing a high-purity substrate wafer that is thoroughly cleaned through solvent cleaning[1], followed by oxygen plasma ashing[2]. If necessary, one may choose to replace the solvent clean step with a piranha

1. Ultrasonic clean of a wafer in NMP, acetone, and methanol solution, respectively, for 3 min each

2. 3 min duration with 150 W RF-power at 300 mTorr pressure

etch[3]. Note that we want the wafer surface to be somewhat hydrophilic to promote adhesion of the photoresist and obtain optimal surface tension characteristics. We then spin positive photoresist on the wafer, which is exposed and developed using UV lithography to create cylinder structures on the wafer (see figure 4.1a). Depending on the height of the final HBAR, this process is compatible with a range of photoresists, including AZ series (P4620 and P4330) and Microposit S1800 series (S1818 and S1813). In order to promote the adhesion of the photoresist structures, the sample is vapor primed with hexamethyldisilane (HMDS). The sample then undergoes a reflow process in an upside-down orientation in an enclosed chamber filled with propylene glycol methyl ether acetate (PGMEA) vapor. As the photoresist structures absorb the solvent vapor and start to reflow, surface tension results in dome-like structures to appear by smoothing sharp corners of the photoresist cylinders (see figure 4.1c). At this stage, note that too much surface tension can lead to the deformation of the photoresist, losing its initial circular structure, while too little surface tension leads to the separation and removal of photoresist structures during the reflow process. Once concave dome structures are fully formed, the sample is hard-baked to remove any residual solvent. The sample is then put into a dry-etch chamber where it goes through a reactive ion etching (RIE) process with custom recipes optimized for the type of substrate material used. Finally, the sample is piranha cleaned after the RIE to remove any organic contaminants. For surface oxide forming materials such as Si, an additional oxide stripping step of a short HF dip procedure, also known as surface passivation, is beneficial as it helps achieve a consistent surface termination of dangling bonds.

3. 10 min submersion of sample in 3:1 mixture of sulfuric acid and hydrogen peroxide at 100°C

Label	Material	Linewidth	Pre-treatment	Post-treatment
XQu01*	x-quartz	1.3 kHz	-	Pr
XQu02	x-quartz	410 Hz	-	Pr
XQu03	x-quartz	9.3 kHz	-	Pr
Si01-1	Si	150 kHz	-	-
Si01-2**	Si	6 kHz	-	Pr, HF
Si01-3$_{\dagger}$	Si	1 MHz	-	Pr, HF
Si02.1-1	Si	700 kHz	-	-
Si02.1-2$_{\dagger\dagger}$	Si	2.1 MHz	-	Pr, HF
Si02.2-1	Si	40 kHz	-	Pr, HF
Si02.2-2***$_{\dagger\dagger\dagger}$	Si	45 kHz	-	Pr, HF
Si03	Si	0.6∼2.5 MHz	Furnace, HF	Pr, HF
Si04-1	Si	900 kHz	-	Pr, HF
Si04-2	Si	120 kHz	-	2×(RTP, HF), Pr, HF
Si04-3	Si	1 MHz	-	4×(RTP, HF), Pr, HF

Table 4.1: **Table of selected HBAR devices fabricated** In the label column, devices are named following the order, 'device name - measurement number'. In the treatment column, Furnace means processed in a horizontal tube furnace, HF means 1 min HF strip of oxide, Pr means piranha cleaned, and RTP means put through rapid thermal processing. *XQu01 sample is identical to the sample used in section 6.2.1, figure 6.2. **Si01-2 sample is identical to the sample used in reference [53]. ***Si02.2-2 sample is identical to the sample used in section 6.2.3, figure 6.5. † Measured after 1 year of room storage. †† Measured after 2 months of room storage. † † † Measured after 10 months of vacuum storage.

4.4.2 Measurements

For the measurements of acoustic Q of fabricated HBAR devices, we use stimulated Brillouin scattering measurement described in chapter 5. In table 4.1, we provide a list of devices made and corresponding acoustic linewidths measured.

Due to the final goal of this dissertation, we focus on making HBAR devices on x-cut quartz and Si. HBARs made on x-cut quartz consistently had good Q-factors with correlated linewidths of < 10 kHz. The highest Q device made was the XQu02 device where we observed a linewidth of 410 Hz, consistent with a value limited by surface roughness of 1.2 nm. We also perform a ring-down measurement with device XQu03. Results are shown in figure 4.2, where we confirm that we do not observe any noticeable dephasing in our HBAR devices ($\Gamma_{\phi} \approx 0$).

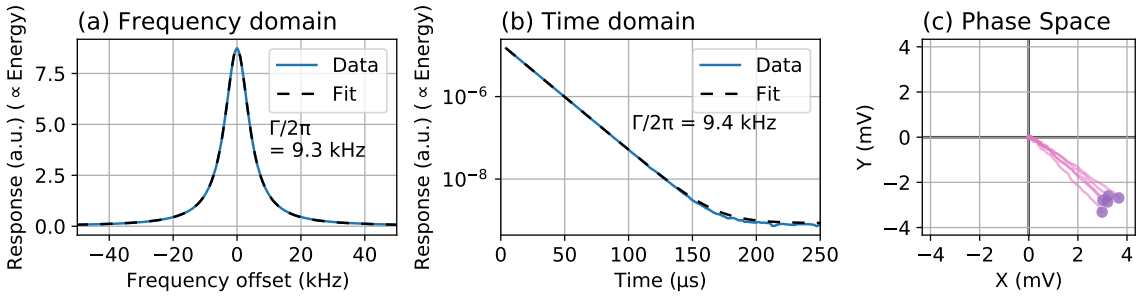

Figure 4.2: **Ring-down measurement on HBAR** (a) Frequency response and (b-c) ring-down measurement done with the HBAR sample XQu03. Microwave tone is used to piezoelectrically drive the acoustic mode in an optical single-pass configuration (see section 5.2.3 for details). In order to perform a ring-down measurement, we send in a microwave pulse instead of a tone and observe the time-dependent decay of acoustic resonant response at the end of the pulse. In the phase space data, initial starting points are indicated in purple, and trajectories of time-dependent decay are indicated in pink.

HBAR devices on Si, on the other hand, had a lot more variability in their linewidth compared to devices on x-quartz. Beyond the devices listed in table 4.1, we observed acoustic linewidths varying between 0.6 $\sim$ 2 MHz in Si-based devices. We suspect this is due to possible damages and contaminations in the Si devices. In fact, there are many studies discussing damages that certain fabrication procedures, such as RIE, can inflict on Si substrates [102–109]. While trying to tackle this issue, we made several notable observations.

4.4.3 Observation 1: effects of thermal treatments

In an attempt to relax the built-in stress inside a Si substrate that may be affecting the acoustic properties, we explored options for thermally treating the samples. Thermal treatment can anneal the substrate, relaxing the built-in stress and it leads to oxidation of the surface, effectively peeling off damaged and contaminated surface layer.

Firstly, we put Si wafers in a horizontal tube furnace, exposing them to high temperatures (900 $\sim$ 1000 °C) for 4 hours. This results in surface oxide growth of $\sim$ 1 μm,

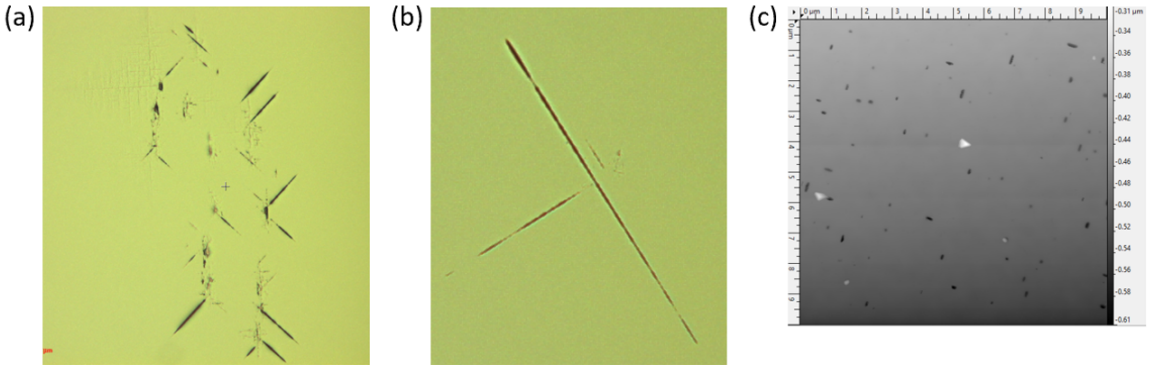

Figure 4.3: **Surface damage on Si samples from thermal treatments** (a-b) Optical microscope image of Si sample surface. These samples went through initial furnace treatment and oxide strip before being fabricated into plano-convex HBARs. Marks shown are bump features with $2 \sim 20\mu$m width, $1 \sim 5\mu$m height, and $10 \sim 100\mu$m length. Directions of the bumps are along y and z crystal axis. (c) AFM image of Si sample surface that has gone through four cycles of rapid thermal oxidation and HF strip post-HBAR fabrication (device Si04-3 from table 4.1). Marks shown are pits with < 100 nm width, ~ 300 nm depth, and ~ 250 nm length. Directions of the pits are along y and z crystal axis.

which we remove by dipping the wafers in HF. Acoustic responses of HBARs made on Si wafers with such furnace treatment are given in table 4.1, device Si03. Unfortunately, we do not observe any noticeable improvement in the acoustic linewidth. Monitoring the surfaces of HBAR devices made on furnace-treated Si, we can identify several defects along the crystal axis of Si (see figure 4.3a-b). Thus, it is highly likely that our furnace treatment is poorly executed, and more careful study and optimization are desired to actually benefit from furnace treatments.

Secondly, we also record the effects of thermal treatment post-fabrication of HBARs. Since RIE-induced damages are mostly accumulated on the surface [104–107], our goal here is to strip off surfaces of Si through oxidization. After fabrication of an HBAR, we probe its initial characteristics (Si04-1 in table 4.1). Then, this sample is put through rapid thermal processing (RTP) and HF strip of oxide. RTP lasts about 5 to 10 min and it produces ~ 30 nm of surface oxide layer at a time. After each cycle of RTP and HF dip, the acoustic property of the device is characterized again. The acoustic property of the device improves until the 2nd cycle of the RTP thermal process.

As shown in device Si04-2 in table 4.1, 2 cycles of thermal process post-fabrication improves the acoustic linewidth by a factor of ~ 7.5. However, from the 3rd cycle of the RTP thermal process, we observe degradation of acoustic linewidth, and at the 4th cycle, we even observe worse acoustic quality than its initial value (device Si04-3, table 4.1). We believe that this is because our thermal process not only fixes certain substrate damages but also induces other certain substrate damages. Probing sample Si04-3 under AFM, we indeed observe accumulated damages on the surface after multiple rounds of RTP thermal treatment (see figure 4.3c). Hence, thermal treatment of Si HBAR post-fabrication can improve the acoustic quality of the device, but it needs further optimization to minimize the additional damage it also induces on the substrate.

4.4.4 Observation 2: surface passivation

Another observation from the list of samples is the effect of the surface passivation step in Si. Surface passivation using piranha solution and HF, as laid out in reference [110], substantially improves the acoustic quality of our devices. This is shown in devices Si01-1 and Si01-2, where we detect acoustic linewidth improvement from 150 kHz to 6 kHz, and in devices Si02.1-1 and Si02.2-1, where we detect acoustic linewidth improvement from 700 kHz to 40 kHz. In both cases, surface passivation results in over an order of magnitude improvements in acoustic linewidths. Thus, we include surface passivation as an essential post-fabrication step before making measurements in Si HBAR devices.

4.4.5 Observation 3: on sample deterioration and storage

The final observation we can make from Si samples is the degradation of acoustic quality in time, depending on their storage conditions. After the measurement of device Si01-2, it was stored in room condition for approximately 1 year and then

re-measured (labeled device Si01-3). We observe a degradation in acoustic linewidth from 6 kHz to 1 MHz, which is irreversible even after repeating surface passivation steps. In a separate sample, Si02.1-1 and Si02.1-2, acoustic linewidth experiences an irreversible degradation from 700 kHz to 2.1 MHz, just after 2 months of room storage. In this case, the sample has not gone through surface passivation prior to storage. We speculate that room condition storage leads to the absorption of contaminants into the Si devices that are irreversible with the methods available to us.

In order to tackle this issue with storage, we attempted to store a device under a vacuum. A surface passivated sample (Si02.2-1) is stored in vacuum storage for 10 months (Si02.2-2). Characterizing the acoustic properties of the sample before and after storage, we observe that the sample maintains its acoustic linewidth of $\sim$ 40 kHz.

Hence, we decide vacuum storage to be our standard protocol for long-term storage of Si samples to avoid degradation in acoustic qualities. Fortunately, other materials that we study in this dissertation, such as quartz and CaF_2, do not experience such degradation, so they are free from such storage requirements.

Chapter 5

A hybrid cavity platform for simultaneous electro-optomechanical coupling

5.1 Introduction

Interactions between acoustics and optics have been long studied and are being heavily utilized, in the field of optomechanics. Optomechanical systems have been used in many contexts, including that of precision measurements [111, 112], generation of non-classical mechanical states [4, 113–115]. In particular, through optomechanical systems, people are able to perform quantum operations on mechanical motions, such as laser cooling a mechanical state to its quantum ground state [4] and realizing remote entanglement between mechanical resonators [115].

Similarly, electromechanical system is another field of study that harnesses the versatile interaction of acoustics with microwaves. Besides the numerous use-cases of piezo-actuators in everyday life, electromechanics is explored in research including the tests of fundamental physics [81], quantum ground state cooling [3], single phonon

control [5], and control of acoustic quantum state through qubits [7, 8]. With long lifetimes and high compactness (compared to microwave resonators) of acoustic resonators, there are also efforts to investigate further applications to quantum memory elements in quantum computers [11].

Combining optomechanical and electromechanical interactions on a single platform, electro-optomechanical systems allow us to traverse between optical, acoustic, and microwave regimes with relative ease, opening the door to important operations such as transduction and precision sensing [14, 24]. In particular, there are several types of electro-optomechanical devices being developed to realize an efficient microwave-to-optical quantum transducer for quantum computers [15–23]. The type of platforms includes mechanical membrane [15–17], OMC [18–20], thin film devices [21,22], and BAR devices [23]. With electro-optomechanical transducers, people have demonstrated record transduction efficiency with 47% [17], low added noise ($<$ 1 photons) [20], and integration with a superconducting qubit [16, 20].

Here, we present a novel electro-optomechanical (piezo-Brillouin) design with an HBAR that simultaneously integrates piezoelectric and Brillouin interaction in a resonantly enhanced configuration. With advantages such as long acoustic lifetimes [56], good thermal properties, good optical mode matching [52, 54], and well-established fabrication steps [53], an HBAR is an appealing ingredient for an electro-optomechanical system. Besides, strong optomechanical coupling [54, 55] and strong electromechanical coupling [7] to HBARs have been shown in separate works, making it even more intriguing to come up with experimental designs that take advantage of HBARs.

In this chapter, we present the ingredients for our piezo-Brillouin device and the measurement layouts. Then, we provide a theoretical model to predict and understand the response we would get from the device. We also compare our initial design without an optical cavity to our later design with optical cavity integration, highlighting the

high resonant enhancement of signal we can achieve by adding the optical cavity element to the design.

5.2 Experimental setup

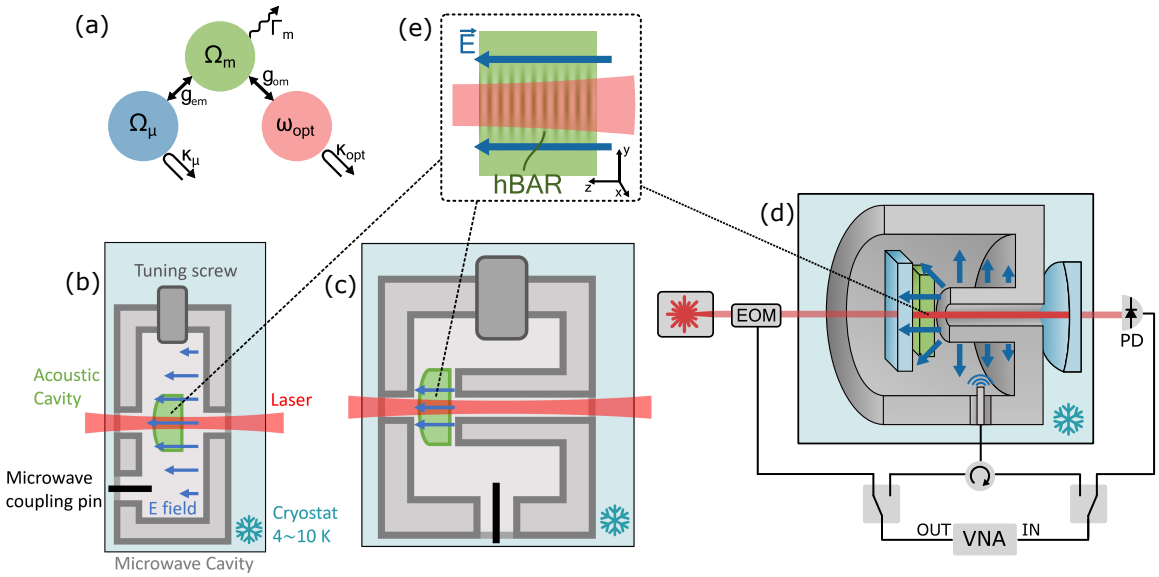

Figure 5.1: **Assembly of hybrid piezo-Brillouin optomechanical system** (a) Simplified diagram of mode couplings and decay pathways for the optical (red), microwave (blue), and acoustic (green) modes. (b-d) Cross-section of hybrid cavity assemblies showing acoustic resonator (green), microwave cavity (grey), and optical mirrors (light blue). The cavities are placed in a He-4 flow cryostat between 4∼10 K. Dark blue arrows indicate microwave E-field, red arrows indicate optical light, black insert into the cavity is the microwave coupling pin, and dark gray block on the top is the tuning screw for microwave frequency tuning. Rectangular microwave cavity (b) and re-entrant microwave cavity (c) are used for single-pass measurement, hence optical cavity is absent in this assembly. Lock-in signal detection is performed with these devices (details of the experimental schematic in figure 5.6). Coaxial microwave cavity (d) is used for both single-pass measurements without an optical cavity and resonantly enhanced measurements with an optical cavity. Direct VNA-type signal detection is done in this device and a simplified experimental schematic is illustrated. Microwave and optical signals can be injected by driving the microwave cavity or electro-optic modulator (EOM), respectively. Optical signals are detected in transmission (at photodiode, PD), using the pump light as the heterodyne local oscillator. Microwave signals can be collected and amplified directly. A detailed experimental schematic is shown in figure 5.7. (e) Inset showing the overlap between the microwave/optical/acoustic modes. Dark green wavefronts indicate the longitudinal acoustic mode of the HBAR. Adapted from Ref. [57].

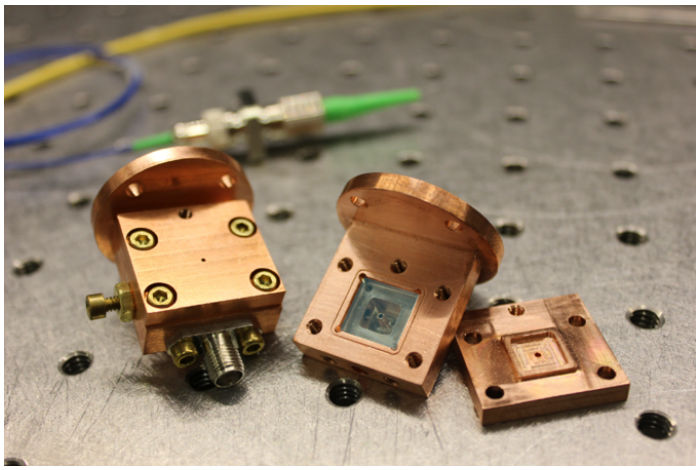

Figure 5.2: **Example hybrid cavity device** Image of a hybrid cavity device image used in one of the experiments. On the left is the assembled version, the middle is the bottom piece of the device, and the right is the lid. The body of the device, which is the microwave cavity part, is made out of oxygen-free high thermal conductivity (OFHC) copper for better thermalization and reasonable microwave Q. This example device uses a re-entrant microwave cavity as its microwave element and lacks an optical cavity. The bulk acoustic substrate is placed between the body and the lid. It is marked as transparent blue in the image. In reality, the substrate used in this image is CaF_2, which is fully transparent. A small through hole at the center of the device is to allow optical light to interface with the acoustic substrate. The metallic connector shown at the lower side of the left image is the microwave coupling pin. The brass screw on the side of the left image is the frequency tuning screw. The round top part is for attaching to the cold finger of the He-4 cryostat.

5.2.1 Cavity assembly

Our hybrid platform is designed to achieve simultaneous microwave (piezoelectric) and optical (Brillouin) coupling to an HBAR device, as illustrated in figure 5.1(a). An example device is shown in figure 5.2. We explore both options of a single-pass implementation without resonant enhancement of signal (figure 5.1b-c), and optical cavity integrated version (figure 5.1d) enabling resonant enhancement of signal. For practical reasons, signal detection when rectangular and re-entrant microwave cavities are used is done through a lock-in measurement and when a coaxial cavity is used is done through direct VNA measurement. This is further elaborated in the later sections.

In contrast to integrated nanomechanical devices that have all of the elements on a single chip, this platform is an assembly of three distinct resonators (acoustic, optical, and microwave) that are well mode-matched (figure 5.1e). This modular design enables independent optimization of each resonator, including quality factors and mode-matchings, which are discussed in the following sections. The optical and microwave resonators are designed to be individually tunable with a wide range, allowing resonant coupling to virtually any transparent crystalline material, and fully taking advantage of the universality of Brillouin optomechanical interaction.

Acoustic cavity (HBAR)

As discussed previously in chapter 4, the platform design centers around the use of an HBAR, which supports longitudinal elastic standing waves confined between the opposing surfaces of a crystalline substrate. At modest cryogenic temperatures ($T = 4 \sim 10$ K), these Fabry-Perot-like acoustic modes can achieve quality factors at GHz (MHz) frequencies in excess of 10^7 (10^9), by working with high purity crystals with smooth surfaces [53, 56].

Plano-convex crystals offer stable resonances with the highest mechanical Q, thus we use plano-convex HBAR fabricated on a chip for certain single-pass designs (figure 5.1b-c). For a resonantly enhanced device (figure 5.1d), however, there is a restriction in the acoustic cavity geometry due to optical-acoustic mode-matching alignment imperfections. There are currently efforts in the lab to improve the alignment between Fabry-Pérot optical cavity modes and plano-convex acoustic cavity modes, which is a technique highly desired for improving the performance of our piezo-Brillouin system. For now, we work with flat, unprocessed substrates for the resonantly enhanced setup. With a simpler flat-flat resonator, acoustic modes experience diffraction loss, but still reach $Q > 10^4$, and there are added benefits such as material flexibility and simplified assembly. The substrates host a set of longitudinal modes at their Brillouin frequency

given in equation 2.7 (typically in the range, 10∼50 GHz), spaced by a mechanical free spectral range, $\Delta_{\mathrm{m}} = v_{\mathrm{m}}/2L_{\mathrm{m}}$, and with acoustic linewidth (loss rate), Γ.

Microwave cavity

For electromechanical coupling to an HBAR, we rely on resonant piezoelectric interactions with a 3D microwave resonator as shown in figure 5.1(b-d). We require a microwave resonator with resonant modes that match the acoustic Brillouin frequency (10∼50 GHz) and have uniform E-fields along z-direction (figure 5.1e), ideally with high Q-factor and easy tunability. Rectangular, re-entrant, and coaxial stub cavities, discussed in chapter 3.4, are common resources for quantum technologies, and are well-suited for this task [75, 76].

The type of microwave cavity is chosen based on the goals and characteristics of the piezo-Brillouin device we want to produce. A rectangular cavity has the advantage of being easy to machine and being able to easily target high frequencies (above 20 GHz) by using higher-order modes. Thus, we choose to work with a rectangular cavity for substrates with high Brillouin frequencies. Silicon is an example of such a substrate with a high Brillouin frequency of ∼37 GHz. However, a rectangular cavity is prone to forming spurious microwave modes near the mode of interest due to its simplistic design.

A re-entrant cavity, on the other hand, has a well-localized fundamental microwave mode, spectrally isolated from spurious modes. Additionally, the E-field of a re-entrant cavity is highly concentrated (see table 3.2), making it the most favorable design to maximize the coupling rate (see equation 3.6). Despite the practical machining challenge that limits the design to a relatively lower range of frequencies (below 15 GHz), we use re-entrant cavities to interface with substrates with moderate Brillouin frequencies, such as quartz (∼11 GHz) and CaF_2 (∼13 GHz).

A coaxial cavity also has resonant modes that are well spectrally isolated with

minimal spurious modes. With moderate E-field strength (see table 3.2), and with higher order modes available, it is the most flexible design among the candidates. Moreover, a coaxial cavity can be made seamless, giving it an edge when we require a higher Q-factor for improvements further down the road. Coaxial cavities are used to couple to a range of substrates, including quartz, CaF_2, and $LiNbO_3$ ($\Omega_B \sim$21 GHz).

The tunability of resonance frequency is a key requirement for the microwave cavities to effectively couple to acoustic substrates, as we rely on resonant piezoelectric interaction. Since the microwave cavity designs we are considering are 3-dimensional, it is fairly straightforward to achieve reasonable frequency tunability by modifying the cavity geometries. As illustrated in figure 5.1(b-c), rectangular and re-entrant designs have a tuning screw on the side that tunes the cavity frequency by effectively altering the cavity length (rectangular cavity) and modifying the cavity inductance (re-entrant cavity). Typically, this achieves a tuning range of $<$ 500 MHz ($\approx \pm 5\%$) for a rectangular cavity and $<$ 200 MHz ($\approx \pm 2\%$) for a re-entrant cavity. Tuning of a coaxial cavity resonance frequency is done by changing the length of the center post, which provides $\sim$3 GHz of tuning range ($\approx \pm 30\%$). An alternative way of cavity frequency tuning includes inserting a low-loss dielectric rod [78].

Here, we work at T = 4$\sim$10 K and choose oxygen-free high thermal conductivity (OFHC) copper for its thermal conductivity and low electrical resistivity (see figure 5.2). Although such a design choice comes with a limited Q-factor (conductive loss limits microwave Q-factor below 2000), it is sufficient to piezoelectrically drive phonons, as shown in the following chapters. Upgrading the cavity material from copper to superconducting metal is a promising future direction that the device can take, as the Q-factor of a coaxial stub cavity can exceed $Q_\mu > 10^7$ [76]. In experiments, we also observe frequency drift of approximately 10$\sim$40 MHz (0.1% $\sim$ 0.4%) which corresponds to the thermal contraction of copper between room and cryogenic temperatures. Additionally, we make a small (1 mm diameter) aperture through the

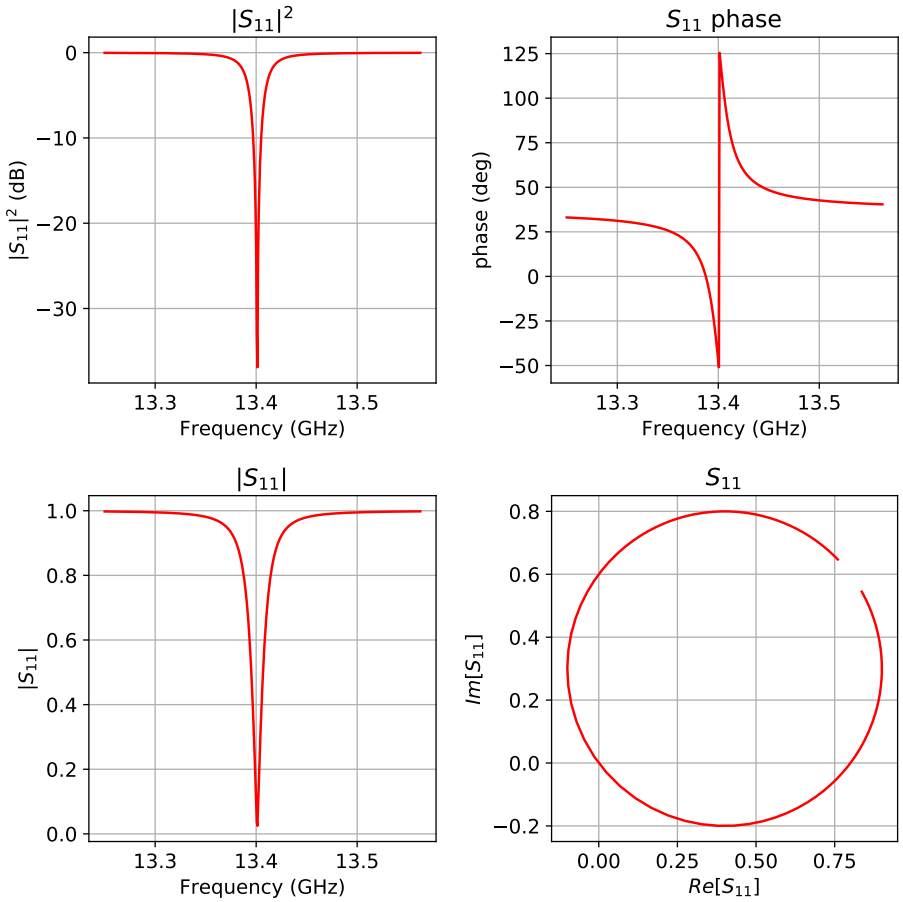

Figure 5.3: **Example S_{11} spectrum of a microwave cavity** S_{11} spectrum of a microwave cavity is plotted based on equation 5.3. In an experiment, we first take data from VNA, then fit it with the given function. Parameters used in this example are, $\Omega_\mu/2\pi = 13.4$ GHz, $\kappa_\mu/2\pi = 20$ MHz, $\kappa_{\mu,\mathrm{c}}/2\pi = 10$ MHz, and $\kappa_{\mu,\mathrm{i}}/2\pi = 10$ MHz.

microwave cavity to allow for optical access, which has a negligible impact on the Q-factor of the microwave design.

It is important to quantify the number of circulating microwave photons inside a microwave cavity, as it directly leads to the number of piezoelectrically driven phonons following equation 3.9. We use a vector network analyzer (VNA) to take the reflection (S_{11}) data from microwave cavities. This can be understood using the equation of motion of microwave photons inside a cavity,

$$\dot{c} = i(\Omega - \Omega_\mu)c - \frac{\kappa_\mu}{2}c + \sqrt{\kappa_{\mu,\mathrm{c}}}c_{\mathrm{in}}. \tag{5.1}$$

Using input-output relation,

$$c_{\text{out}} = \sqrt{\kappa_{\mu,\text{c}}}c - c_{\text{in}}. \tag{5.2}$$

Combining equations 5.1 and 5.2 in steady state, we get,

$$S_{11}(\Omega) = X\frac{c_{\text{out}}}{c_{\text{in}}} = \alpha e^{i(\Omega-\Omega_\mu)\beta}\frac{\kappa_{\mu,\text{c}} - \frac{\kappa_\mu}{2} + i(\Omega-\Omega_\mu)}{\frac{\kappa_\mu}{2} - i(\Omega-\Omega_\mu)}, \tag{5.3}$$

where $X = \alpha e^{i(\Omega-\Omega_\mu)\beta}$ is a fit parameter to take into account VNA calibration imperfections and drifts. Example S_{11} spectrum following equation 5.3 is shown in figure 5.3. The number of circulating photons (n_μ) is given by observing the energy in the cavity,

$$E_\mu = \hbar\Omega_\mu n_\mu = \frac{1-|S_{11}|^2}{\kappa_{\mu,\text{i}}}P_\mu, \tag{5.4}$$

where P_μ is the input microwave power launched into the cavity and $\kappa_{\mu,\text{i}}$ is the internal loss of the microwave cavity ($\kappa_\mu = \kappa_{\mu,\text{i}} + \kappa_{\mu,\text{c}}$).

Optical cavity

Including an optical cavity into this piezo-Brillouin system allows for resonant enhancements of both the optical pump and signal fields [116]. As demonstrated in prior works [54, 55], a Fabry-Pérot cavity is well-suited to this task, with Gaussian modes that achieve good spatial overlap with highly confined HBAR modes (see Fig. 5.1e). Also, it is simple to put together with other HBAR/microwave cavity components, can predict performance based on mirror reflectivities, and has well-established methods to control/tune its resonance frequencies [54].

Finesse ($\mathcal{F}$) is an important factor in understanding an optical cavity. It represents

the number of round-trips that a light wave can make before decaying, expressed as,

$$\mathcal{F} = \frac{\Delta_{\text{opt}}}{\kappa_{\text{opt}}}, \tag{5.5}$$

where Δ_{opt} is the optical free spectral range. It is related to the cavity Q-factor by,

$$Q = \frac{\mathcal{F}\omega_{\text{opt}}}{\Delta_{\text{opt}}}. \tag{5.6}$$

In a Fabry-Pérot cavity comprised of mirrors with reflectivities R_1 and R_2 (figure 5.4a), finesse can be predicted as,

$$\mathcal{F} = \frac{\pi(R_1R_2)^{1/4}}{1-\sqrt{R_1R_2}}. \tag{5.7}$$

In reality, the finesse of our optical cavity deviates from this value to a small degree due to having a crystal placed between the mirrors and making it a composite optical cavity figure 5.4(b).

The resonant frequencies of our optical cavity are tuned with a piezo-actuator that is incorporated into one of the mirrors, enabling precise control of the cavity length. As we modify the cavity length, however, the optical mode spacing does not simply follow the conventional expression, $\Delta_{\text{opt}} = c/2L_{\text{opt}}$, due to the vacuum/dielectric composition of our optical cavity. To characterize this uneven optical mode spacing, we follow the work done in reference [54]. The transmission matrices for a mirror and for propagation in space are,

$$\begin{aligned} \mathcal{T}_{\text{mir}} &= -\frac{i}{\sqrt{T}}\begin{pmatrix} -1 & \sqrt{R} \\ -\sqrt{R} & 1 \end{pmatrix} \\ \mathcal{T}_{\text{prop}} &= \begin{pmatrix} e^{ik_{\text{opt}}z} & 0 \\ 0 & e^{-ik_{\text{opt}}z} \end{pmatrix}. \end{aligned} \tag{5.8}$$

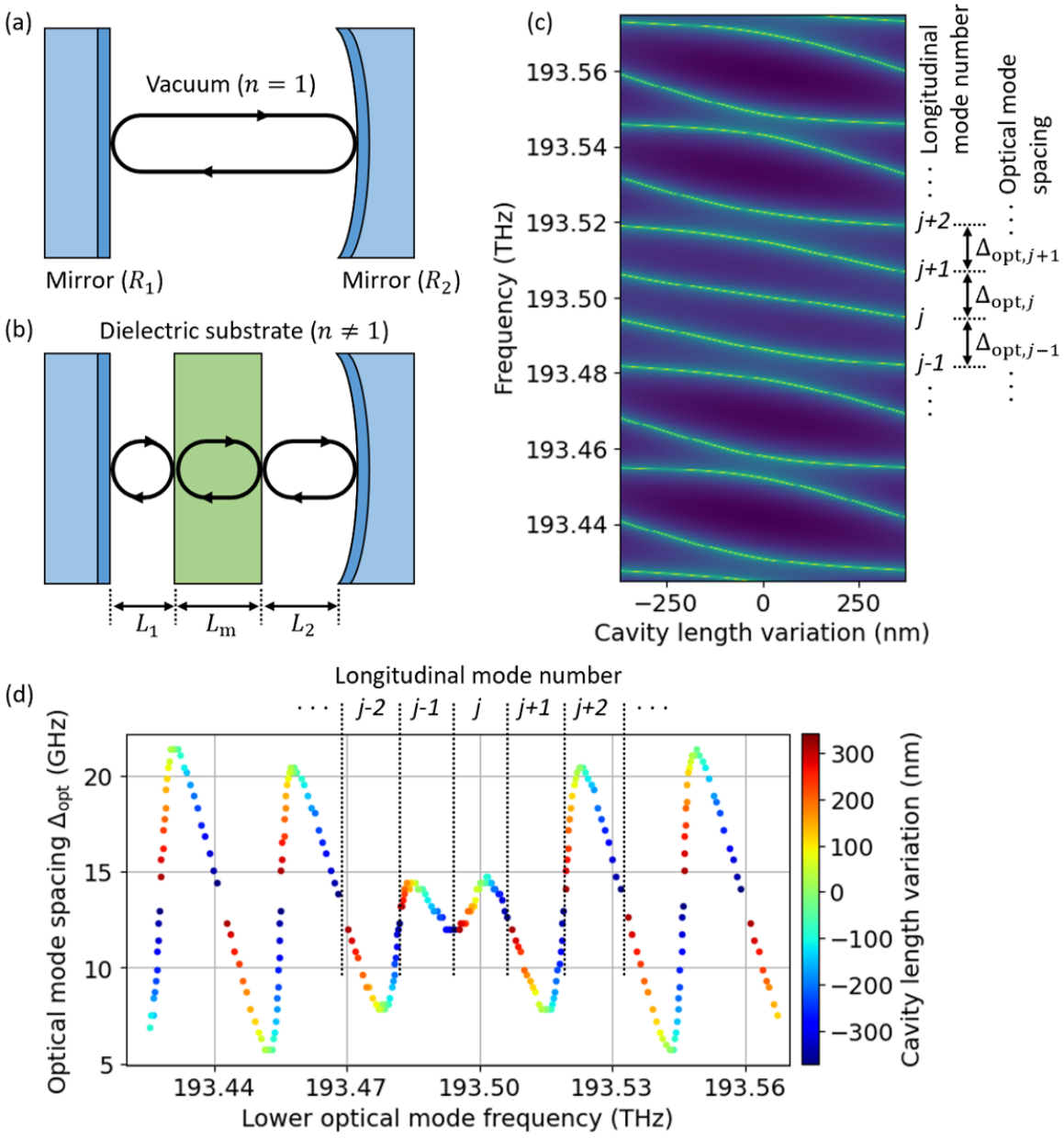

Figure 5.4: **Frequency tuning in a composite optical Fabry-Pérot cavity** (a) Optical Fabry-Pérot cavity composed on mirrors with reflectivities R_1 and R_2. (b) Optical Fabry-Pérot cavity with dielectric crystal in the middle. Fresnel reflections at the vacuum/dielectric interface alter the optical mode frequency spacing to be wavelength-dependent. (c) Simulated optical cavity resonance spectrum as a function of cavity length variation. Bright green indicates peak spectral response, or resonance. Due to the dielectric substrate in the middle, we see uneven optical mode spacing (Δ_{opt}). The cavity length is modified by shifting one of the mirrors using a piezo-actuator. We simulate this by modifying L_2 by the varied length. **(Caption continued in next page)**

Figure 5.4: **(Caption continued from last page)** Parameters used are, $L_1 = 5$ mm, $L_2 = 5$ mm, $L_{\mathrm{m}} = 500$ um, $R_1 = 0.99$, $R_2 = 0.99$, and $n_{\mathrm{substrate}} = 3$. (d) Plot of optical mode spacing versus the lower frequency of the optical mode pair. Change of mirror position (L_2) is indicated as a colorscale from blue to red, as shown in the colorbar. In this simulation, we achieve Δ_{opt} variation of up to $\sim$15 GHz, which is not representative of what is achieved in the experiment due to the difference in experimental parameters. Note that in both (c) and (d), we see periodicity in Δ_{opt} as cavity length is varied by approximately half of the optical wavelength ($\sim$1550 nm/2) .

We can calculate the total transmission matrix by combining the appropriate transmission matrices for our optical system,

$$\mathcal{T}_{\mathrm{tot}} = \mathcal{T}_{\mathrm{mir1}} \cdot \mathcal{T}_{\mathrm{propVac}} \cdot \mathcal{T}_{\mathrm{mirSubst}} \cdot \mathcal{T}_{\mathrm{propSubst}} \cdot \mathcal{T}_{\mathrm{mirSubst}} \cdot \mathcal{T}_{\mathrm{propVac}} \cdot \mathcal{T}_{\mathrm{mir2}}, \tag{5.9}$$

where subscript mir1 (mir2) indicates the mirror on the light entry side (exit side) of the cavity, Vac is vacuum, and Subst is substrate. For inputted light wave across a range of frequency, we can obtain the transmitted power spectrum by plotting $|\mathcal{T}_{21}|^2$. Optical cavity tuning, achieved by shifting a mirror position through a piezo-actuator is illustrated in figure 5.4(b) with varying L_2. The shift in $|\mathcal{T}_{21}|^2$ spectrum as we move one of the mirror positions is shown in figure 5.4(c). In experiment, we can vary the piezo actuator length by approximately 500$\sim$1000 nm. For the reasons we list in the following section, it is also important to record the change in optical mode spacing, which is shown in figure 5.4(d).

5.2.2 Cavities in frequency space

Since we are using various frequency components spanning microwave to acoustics to optics, it is important to characterize the system in frequency space to understand and control the interactions between them (see figure 5.5).

We start by driving a microwave cavity with resonance frequency Ω_μ. Driven microwave photons, following equation 5.4, piezoelectrically drive phonons in an HBAR

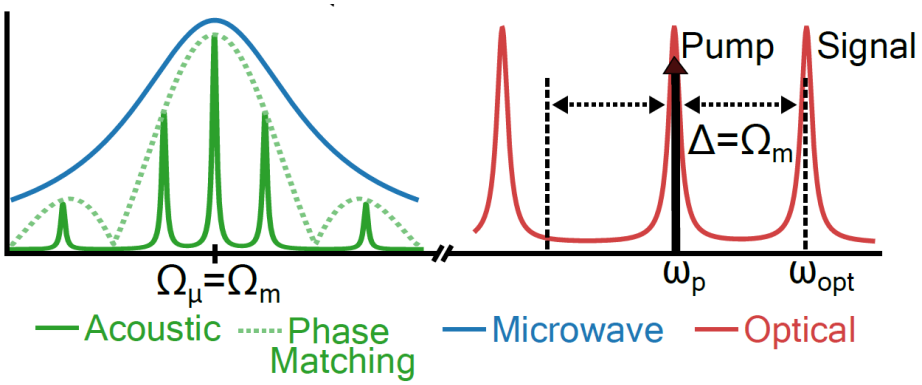

Figure 5.5: **Combined spectral responses of the cavities** Spectral response of microwave (blue), optical (red), and acoustic (green) modes, including the Brillouin phase-matching bandwidth (dashed green). The Stokes and anti-Stokes sideband frequencies are indicated by black dashed lines, symmetrically spaced around the optical pump (ω_{p}, black arrow). Only the anti-Stokes is resonant with an optical mode (at ω_{opt}). Non-uniform optical mode spacing is caused by the Fresnel reflections at the vacuum/dielectric interface of the crystal within the cavity (figure 5.4c-d) [54]. Adapted from Ref. [57].

where their number can be obtained through equation 3.9. As discussed in chapter 4, we design the HBAR to have low loss by using high purity (optical-grade with purity $>$ 99.99 %) material, placing it in a cryostat ($<$ 10 K), and fabricating a smooth (roughness $<$ 1 nm) convex surface. Note that we can still reach a reasonably high Q without the convex lens fabrication. In this highly coherent phonon regime and assuming good mode matching between microwave and phonon modes, piezoelectrically driven phonons are sharply peaked at a set of longitudinal modes within the microwave cavity spectrum. Here, the microwave resonance frequency and the frequency of the primary mechanical mode of interest should be well matched through microwave cavity tuning ($\Omega_{\mu} = \Omega_{\mathrm{m}}$).

In the presence of an optical pump, phonons photoelastically scatter the pump through Brillouin interaction (see chapter 2). Brillouin phase-matching condition in this interaction leads to a $\mathrm{sinc}^2\left[(\Omega - \Omega_{\mathrm{B}})/4\Delta_{\mathrm{m}}\right]$ envelope in the phonon spectrum. Hence, for the interaction to be the most efficient, we choose our mechanical mode to match the Brillouin frequency ($\Omega_{\mathrm{m}} = \Omega_{\mathrm{B}}$). Brillouin interaction also leads to both

the Stokes and the anti-Stokes process. In a single-pass configuration (figure 5.1b-c) without an optical cavity, we place a fiber Bragg grating (FBG) filter at the output of the system to suppress either the Stokes or the anti-Stokes signal from reaching the detector.

For our optical cavity geometry, even a modest finesse ($\mathcal{F} > 1000$) results in optical linewidths that are orders of magnitude less than the mechanical frequency (i.e. $\kappa_{\mathrm{opt}}/\Omega_{\mathrm{m}} < 10^{-3}$). In this deeply resolved-sideband regime, it becomes necessary to use separate resonances to enhance the pump and signal, thus imposing a requirement that the optical mode spacing closely matches the acoustic frequency ($\Delta_{\mathrm{opt}} \equiv \Omega_{\mathrm{m}}$). Two features of this hybrid system allow us to meet this requirement. First, the Fresnel reflections at the vacuum/dielectric interface produced by the HBAR cause the optical mode spacing to be wavelength-dependent (figure 5.4d), effectively suppressing either the Stokes or the anti-Stokes process depending on the cavity resonance alignment (figure 5.5). While this coarse frequency-matching was possible in prior works [54,55], incorporation of a piezo actuator onto one of the mirrors enables more precise control required in this multiply resonant system.

Hence, observing the microwave/acoustic/optical cavity components in the frequency space highlights the importance of frequency matching of each element. In order to achieve the strongest interaction, we not only need to pick the mechanical mode whose frequency well matches the Brillouin frequency ($\Omega_{\mathrm{m}} = \Omega_{\mathrm{B}}$), but also tune the microwave cavity to maximally drive the mechanical mode ($\Omega_{\mu} = \Omega_{\mathrm{m}}$), and tune the optical mode spacing to match the acoustic frequency ($\Delta_{\mathrm{opt}} = \Omega_{\mathrm{m}}$). High tunability of our design that allows > 100 MHz and > 1 GHz tuning range in microwave and optical regimes, respectively, makes it convenient to effectively perform piezo-Brillouin operations. After walking through the experimental apparatus in the following section, we provide a model for the combined piezo-Brillouin process in section 5.3.

5.2.3 Measurement setup

As briefly introduced previously, we use two different measurement schemes depending on the hybrid cavity design. These are lock-in measurement that uses a lock-in amplifier, and direct measurement of optical pump-signal beat tone through a VNA.

We use lock-in measurement primarily for the initial characterization of substrates and for single-pass experiments. It is a useful tool for the initial characterization of acoustic modes as it allows both photoelastic and piezoelectric approaches when driving the acoustic modes. Detection of phonons through photoelasticity or, equivalently, spontaneous Brillouin scattering (SBS) measurement with lock-in detection [52] is a convenient choice as a control experiment, revealing the Brillouin frequency and acoustic features to look for. On the other hand, direct measurement requires high optomechanical cooperativity to execute similar SBS measurements through OMIT, making it unfavorable for photoelastically driven phonon measurement in the single-pass configuration.

On the other hand, direct VNA measurement is mostly used for the resonantly enhanced scheme. The benefits of this type of measurement include straightforward implementation, convenient laser locking ability, and built-in phase noise cancellation. However, unlike lock-in detection, this approach lacks a sensitive photoelastically driven phonon measurement besides OMIT that requires high optomechanical cooperativity, making it not the most optimal setup for a control experiment in the single-pass configuration. Thus, we prefer to do direct measurements on substrates whose acoustic spectrum is already known.

Lock-in measurement

The experimental setup for lock-in measurement is depicted in figure 5.6. There is a small variation in the apparatus depending on whether phonons are driven through photoelasticity (figure 5.6a) or through piezoelectricity (figure 5.6b).

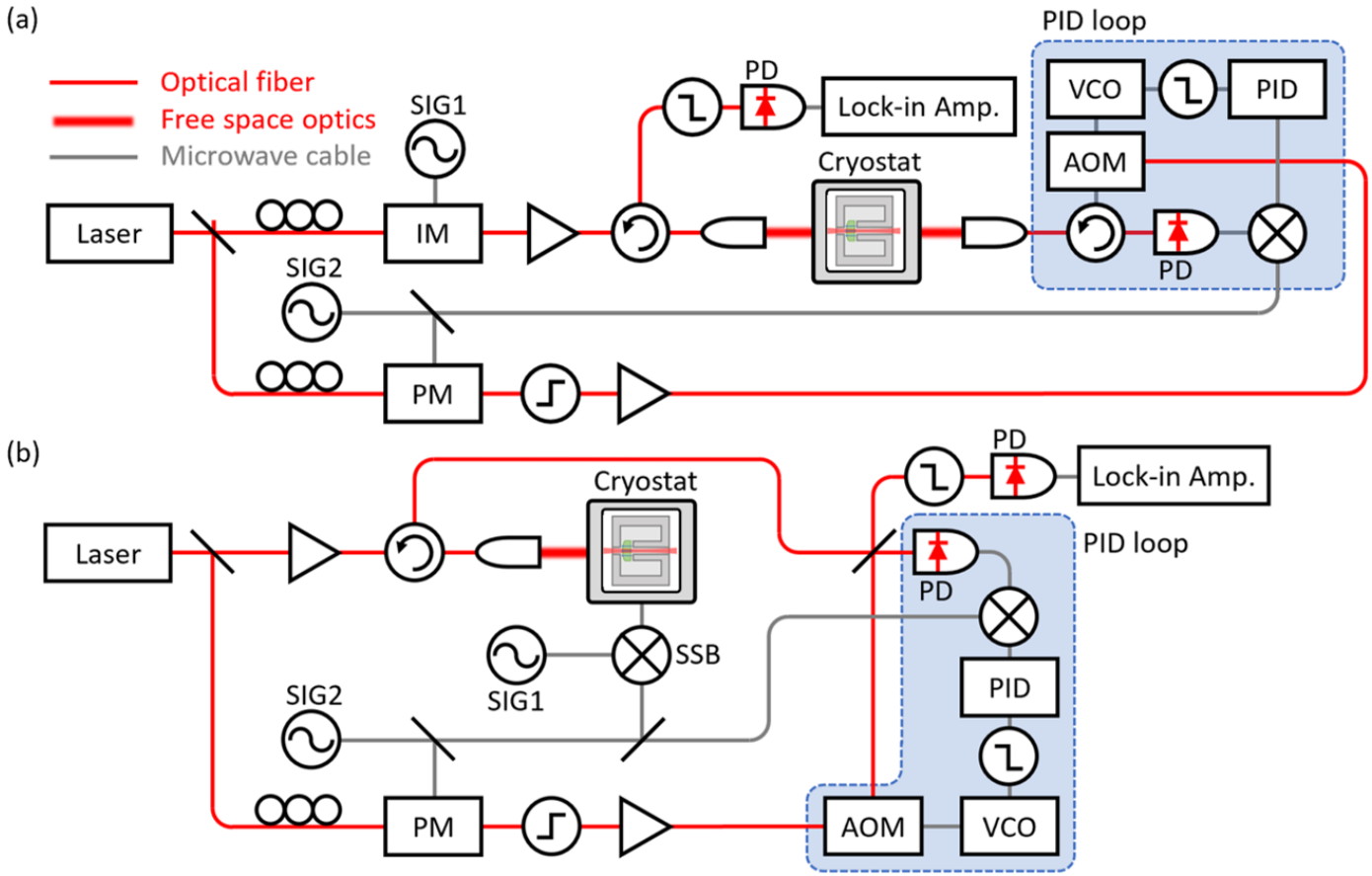

Figure 5.6: **Experimental apparatus for lock-in measurement** PM: phase modulator, IM: intensity modulator, AOM: acousto-optic modulator, SIG: signal generator, PID: proportional integral derivative controller, VCO: voltage controlled oscillator, SSB: single-sideband mixer, PD: photodetector. (a) Schematic for photoelastically driven phonons measurement or, equivalently, stimulated Brillouin scattering (SBS) measurement [52]. This measurement is done as a control experiment for phonon modes characterization before moving on to the piezoelectrically driven phonons measurement. (b) Schematic for piezoelectrically driven phonons measurement. Note that the hybrid cavity inside the cryostat is directly driven through a microwave tone. Part of the apparatus shaded in blue is a PID loop to remove the phase noise in our signal.

We first describe the process for detecting photoelastically driven phonons (figure 5.6a). Laser with $\lambda_{\text{opt}} \approx 1550$ nm is split into two arms, which we call the pump arm and the probe arm. In the pump arm, light is sent through an intensity modulator, creating sidebands Ω_{SIG1} frequency apart from the pump tone, then sent into the hybrid cavity. Ω_{SIG1} frequency is later being used for lock-in detection, so it is set to be around $\Omega_{\text{SIG1}} \approx 10$ MHz, matching the specifications of our lock-in amplifier. In the probe arm, optical sidebands roughly Brillouin frequency away from the main tone is generated through a signal generator (SIG2) and sent through a filter to remove the existing pump tone. This is then sent through an acousto-optic modulator (AOM), further shifting the tone ($\omega_{\text{probe}} = \omega_{\text{pump}} + \Omega_{\text{SIG2}} + \Omega_{\text{AOM}}$), before being launched into the hybrid cavity. Phonons photoelastically generated by the beat note between pump and probe ($\Omega_{\text{m}} = \omega_{\text{probe}} - \omega_{\text{pump}}$) not only scatters the pump tone but also scatters the sidebands of the pump tone, resulting in a creation of sidebands Ω_{SIG1} away from the probe. The optical signal collected goes through a filter to suppress the remaining pump tone that can easily saturate the photodetector. Finally, we perform a lock-in detection at Ω_{SIG1} to detect the beat tone between probe tone (at ω_{probe}) and scattered sidebands (at $\omega_{\text{probe}} \pm \Omega_{\text{SIG1}}$).

Lock-in detection of piezoelectrically driven phonons is done similarly with minor modifications (figure 5.6b). The pump light in this case is not frequency modulated by Ω_{SIG1}, but rather directly launched into the hybrid cavity. Phonons are now driven piezoelectrically at frequency $\Omega_{\text{SIG2}} + \Omega_{\text{SIG1}}$ through a microwave cavity mode, causing the pump light to scatter and create signal at $\omega_{\text{pump}} + \Omega_{\text{SIG2}} + \Omega_{\text{SIG1}}$. Note that the use of a single-sideband mixer (SSB) in driving the microwave cavity is done to avoid crosstalk between microwave components. Instead of being sent into the cavity, light in the probe arm is now combined with the signal light and used as a local oscillator (LO), resulting in a beat tone at $\Omega_{\text{AOM}} - \Omega_{\text{SIG1}}$. After sending the light through a filter to remove the pump tone, lock-in measurement is done at the frequency

$(\Omega_{\mathrm{AOM}} - \Omega_{\mathrm{SIG1}})$.

A proportional integral derivative controller (PID) loop, shown as a blue shaded box in figure 5.6, is there to cancel phase-noise in the setup. The hybrid cavity is attached to the bottom of a He-4 flow cryostat, which is similar to a long beam with many vibrational modes. These vibrations are picked up by our pump and probe lights as phase noise. Experimentally, we observe phase noise when the linewidth of an optomechanical response reaches 1 kHz, setting a lower limit to the detectable acoustic linewidth. Here, we mitigate the effects of phase noise by setting up a PID loop. Light reflected from the cavity acquires the same phase noise as the optomechanical signal, thus the beat tone between this reflected light and a light tone without the phase noise (transmitted light in the photoelastically driven phonons scheme, and LO light in the piezoelectrically driven phonons scheme) contains the phase noise. The beat tone (at $\Omega_{\mathrm{SIG2}} + \Omega_{\mathrm{AOM}}$) is detected with a fast photodetector, then mixed down to an appropriate frequency (Ω_{AOM}). This is then input to a PID controller, which generates an error signal to control a voltage-controlled oscillator (VCO) with output at Ω_{AOM}. The VCO output finally drives the AOM to modulate the probe light, compensating for the phase noise.

Direct measurement

Direct VNA measurement of phonon response, on the other hand, has several benefits over the lock-in measurement, such as being straightforward to implement and phase noise being innately absent due to the identical optical path between LO and signal.

The experimental setup is illustrated in Figure 5.7. Laser with $\lambda_{\mathrm{opt}} \approx 1550$ nm is locked to the optical cavity via the Pound-Drever-Hall (PDH) locking technique. The optical sidebands required for the lock are generated by the signal generator (SIG2) and the PM. For OMIT measurements, a sideband is generated by an intensity modulator (IM), which is driven by a microwave signal generator (SIG1) synchronized to

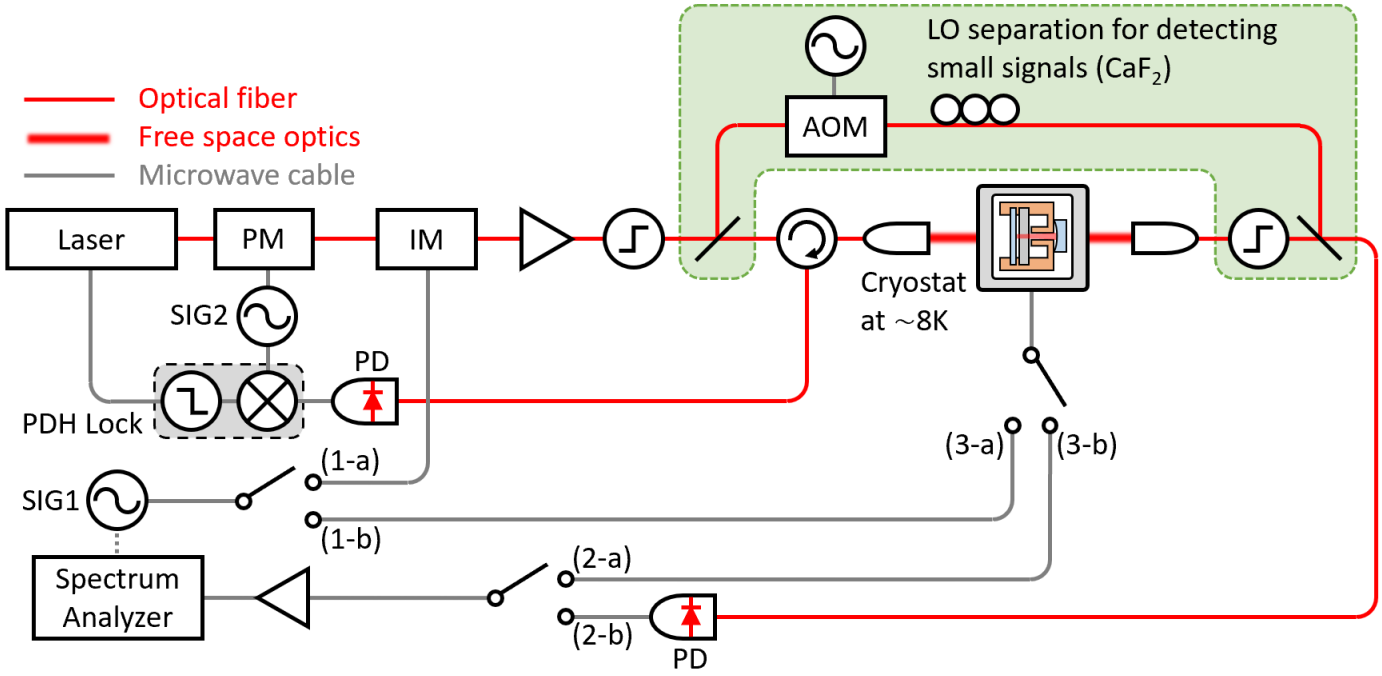

Figure 5.7: **Experimental apparatus for direct VNA measurement** PM: phase modulator, IM: intensity modulator, AOM: acousto-optic modulator, PDH: Pound-Drever-Hall, SIG: signal generator, PD: photodetector. For OMIT measurement, switch combinations (1-a) and (2-b) are used (switch 3 is irrelevant). For microwave-to-optical conversion, switch combinations (1-b), (2-b), and (3-a) are used. For optical-to-microwave conversion, switch combinations (1-a), (2-a), and (3-b) are used. Part of the apparatus shaded in green is not used for transduction measurement (chapter 7), but instead only used for anomalous piezoelectricity measurement (chapter 6) to achieve better signal-to-noise ratio for highly sensitive detection. We later detect piezoelectricity in CaF_2, which is nominally non-piezoelectric, in chapter 6. Adapted from Ref. [57].

the readout frequency of a spectrum analyzer. Here, the main optical tone and the sideband act as the pump and probe, respectively. The beat note between the transmitted pump and probe is measured via a high-speed photodetector and spectrum analyzer. The readout frequency of the spectrum analyzer can be synchronized to the frequency of the signal generator, effectively functioning as a scalar network analyzer. As we later discuss in chapter 7, optical detection of piezoelectrically driven phonons is equivalent to microwave-to-optical transduction, where the drive tone from the signal generator directly drives the microwave cavity, piezoelectrically exciting phonons from which the pump light scatters to achieve electro-optical conversion. Then, it is natural to consider the transduction in the opposite direction, optical-to-microwave transduction. Characterization of optical-to-microwave transduction can be performed in our setup by generating an optical probe from the pump using the intensity modulator, which enters the hybrid cavity and photoelastically drives phonons. However, instead of measuring the optical response of the probe (as in OMIT), the spectrum analyzer directly reads the signal leaving the microwave cavity.

For the OMIT/transduction measurements described, the transmitted pump serves as a LO for high-frequency heterodyne detection of the signal sideband. In this configuration, it is not easy to attenuate the LO power (e.g. to avoid detector saturation) without also attenuating the signal. Therefore, to achieve the enhanced sensitivity needed in anomalous piezoelectricity measurements, we modify the circuit (green shaded box of Figure 5.7), filtering out the transmitted pump and using a separate, controllable LO derived from the original laser. We also shift the frequency of this new LO using an AOM to avoid microwave crosstalk in the detection channel. The spectrum analyzer frequency can be offset accordingly to accommodate this shift between drive frequency and heterodyne frequency, resulting in a unique signal frequency to avoid any potential microwave crosstalk. Using this separate-path LO can reintroduce low-frequency phase noise (<1kHz) in the heterodyne beat note, which does not

currently impact our measurements but needs to be dealt with in the future as we further improve the setup.

5.3 Theory

5.3.1 Resonant enhancement of signal from optical cavity

Here, we consider the configuration in which one seeks to measure an optical sideband scattered from a (piezoelectrically-driven) phonon population. In particular, we analyze the optical power in the scattered sideband on both single-pass and optical cavity configurations, to illustrate the benefit of the optical cavity.

Signal without optical cavity enhancement

In the absence of an optical cavity, a strong pump scatters off phonons to generate a Brillouin sideband. Following section 2.4.2, the optical power in this sideband can be written as

$$P'_{\mathrm{sig}} = \left(\frac{g'_{\mathrm{om},0} L_{\mathrm{m}}}{v_{\mathrm{o}}}\right)^2 P_{\mathrm{p}} n_{\mathrm{m}}, \tag{5.10}$$

which is equivalent to equation 2.46.

Signal with optical cavity enhancement

To compare equation 5.10 to the resonantly enhanced signal, we can derive the output signal power similar to section 2.4.1, but now in terms of phonon number and scattered signal power per pump power per phonon.

In the case where we do consider an optical cavity, it becomes natural to describe the optomechanical interaction through coupled equations of motion for the pump

and signal fields. In the rotating frame, this can be written as,

$$\begin{aligned} \dot{a}_{\mathrm{s}} &= i\sqrt{N_{\mathrm{p}}}g_{\mathrm{om},0}b - \frac{\kappa_{\mathrm{opt}}}{2}a_{\mathrm{s}} \\ \dot{a}_{\mathrm{p}} &= -\frac{\kappa_{\mathrm{opt}}}{2}a_{\mathrm{p}} + \sqrt{\kappa_{\mathrm{opt},c}}a_{\mathrm{in}}. \end{aligned} \tag{5.11}$$

A more extensive Hamiltonian approach can be found in the following section on space model. Here, we assume that there is no optical detuning (the optical signal is sitting exactly at the optical cavity resonance).

In steady state, we obtain

$$\begin{aligned} i\sqrt{N_{\mathrm{p}}}g_{\mathrm{om},0}b &= \frac{\kappa_{\mathrm{opt}}}{2}a_{\mathrm{s}} \\ \frac{\kappa_{\mathrm{opt}}}{2}a_{\mathrm{p}} &= \sqrt{\kappa_{\mathrm{opt},c}}a_{\mathrm{in}}. \end{aligned} \tag{5.12}$$

Inter-cavity pump photon number can then be written as

$$\left(\frac{\kappa_{\mathrm{opt}}}{2}\right)^2 N_{\mathrm{p}} = \kappa_{\mathrm{opt},c}\langle a_{\mathrm{in}}^{\dagger}a_{\mathrm{in}}\rangle. \tag{5.13}$$

From input-output formalism, Equation 5.12, and Equation 5.13, outgoing scattered signal field (a_{out}) is

$$\begin{aligned} a_{\mathrm{out}} &= \sqrt{\kappa_{\mathrm{opt},c}}a_{\mathrm{s}} \\ &= \left(\frac{\sqrt{\kappa_{\mathrm{opt},c}}}{\kappa_{\mathrm{opt}}}\right)^2 (4ig_{\mathrm{om},0})\sqrt{\langle a_{\mathrm{in}}^{\dagger}a_{\mathrm{in}}\rangle}b, \end{aligned} \tag{5.14}$$

and the corresponding scattered signal power in terms of phonon number is

$$P_{\mathrm{sig}} = 16\left(\frac{\kappa_{\mathrm{opt,c}}}{\kappa_{\mathrm{opt}}^2}\right)^2 g_{\mathrm{om},0}^2 P_{\mathrm{p}} n_{\mathrm{m}}, \tag{5.15}$$

where the scattered signal power per pump power per phonon is $16\left(\frac{\kappa_{\mathrm{opt,c}}}{\kappa_{\mathrm{opt}}^2}\right)^2 g_{\mathrm{om},0}^2$.

Resonant enhancement of signal

Compared to the single-pass interaction, the effect of incorporating an optical resonator is to increase the optomechanical cooperativity and P_{sig} by a factor of $\mathcal{F}^2$. Specifically, we can compare equation 5.10 and equation 5.15, where we get a ratio of,

$$\begin{aligned}\frac{P_{\mathrm{sig}}}{P'_{\mathrm{sig}}} &= \frac{16\left(\frac{\kappa_{\mathrm{opt,c}}}{\kappa^2_{\mathrm{opt}}}\right)^2 g^2_{\mathrm{om},0} P_{\mathrm{p}} n_{\mathrm{m}}}{\left(\frac{g'_{\mathrm{om},0} L_m}{v_{\mathrm{o}}}\right)^2 P_{\mathrm{p}} n_{\mathrm{m}}} \\ &= \frac{16}{\pi^2}\eta^2_{\mathrm{opt}}\mathcal{F}^2,\end{aligned} \tag{5.16}$$

where η_{opt} is the optical coupling efficiency, $\frac{\kappa_{\mathrm{opt,c}}}{\kappa_{\mathrm{opt}}}$. Here, we assume that everything was kept constant between the single-pass and resonantly enhanced setup, make a realistic assumption of $\eta_{\mathrm{opt}} \approx \frac{1}{2}$, and recall that $g_{\mathrm{om},0}$ acquires a factor of $\frac{L_{\mathrm{m}}}{L_{\mathrm{opt}}}$ compared to the single-pass coupling rate, corresponding to a geometric filling factor between the acoustic and optical cavities. Thus, we expect $\sim 0.4\mathcal{F}^2$ improvement in signal power by introducing an optical cavity with a finesse, $\mathcal{F}$.

Similarly, we can compare the cavity optomechanical cooperativity in equation 2.25 and equation 2.28,

$$\begin{aligned}\frac{C_{\mathrm{om}}}{C'_{\mathrm{om}}} &= \frac{\frac{4g^2_{\mathrm{om}}}{\kappa_{\mathrm{opt}}\Gamma}}{\frac{g'^2_{\mathrm{om}}}{\Gamma}\frac{L_{\mathrm{m}} n}{c}} \\ &= \frac{16}{\pi^2}\eta_{\mathrm{opt}}\mathcal{F}^2,\end{aligned} \tag{5.17}$$

which also shows a $\propto \mathcal{F}^2$ increase.

5.3.2 State space model

Besides the signal enhancement we can achieve via resonant operation of cavities, we can also predict the spectral response of the system by understanding the state space model [15, 22]. The Hamiltonian describing the system is

$$H/\hbar = \omega_{\mathrm{p}} a^\dagger_{\mathrm{p}} a_{\mathrm{p}} + \omega_{\mathrm{s}} a^\dagger_{\mathrm{s}} a_{\mathrm{s}} + \Omega_{\mathrm{m}} b^\dagger b + \Omega_\mu c^\dagger c + (g_{\mathrm{om},0} a_{\mathrm{p}} a^\dagger_s b + g_{\mathrm{em}} b^\dagger c + \mathrm{H.c.}), \tag{5.18}$$

where ω_{p} (ω_{s}) is the optical wavelength of the pump (signal) mode. In the rotating frame with $H_0/\hbar = \omega_{\mathrm{p}} a_{\mathrm{p}}^\dagger a_{\mathrm{p}} + \omega_{\mathrm{p}} a_{\mathrm{s}}^\dagger a_{\mathrm{s}}$, we obtain an effective Hamiltonian

$$H_{\mathrm{eff}}/\hbar = \Delta_{\mathrm{o}} a_{\mathrm{s}}^\dagger a_{\mathrm{s}} + \Omega_{\mathrm{m}} b^\dagger b + \Omega_\mu c^\dagger c + (g_{\mathrm{om},0} a_{\mathrm{p}} a_{\mathrm{s}}^\dagger b + g_{\mathrm{em}} b^\dagger c + \mathrm{H.c.}), \tag{5.19}$$

where $\Delta_{\mathrm{opt}} = \omega_{\mathrm{s}} - \omega_{\mathrm{p}}$ is the detuning of optical signal frequency from the optical pump. In the undepleted pump regime, we can linearize the Hamiltonian about a strong, coherent pump, giving the expression

$$H_{\mathrm{eff}}/\hbar = \Delta_{\mathrm{opt}} a_{\mathrm{s}}^\dagger a_{\mathrm{s}} + \Omega_{\mathrm{m}} b^\dagger b + \Omega_\mu c^\dagger c + (g_{\mathrm{om}} a_{\mathrm{s}}^\dagger b + g_{\mathrm{em}} b^\dagger c + \mathrm{H.c.}). \tag{5.20}$$

Recall from chapter 2 that $g_{\mathrm{om}} = \sqrt{N_{\mathrm{p}}} g_{\mathrm{om},0}$ and N_{p} is the intracavity pump photon number. The Heisenberg equations of motion for this Hamiltonian and the input-output relation between the fields are given by the following equations:

$$\dot{\mathbf{a}}(t) = A\mathbf{a}(t) + B\mathbf{a}_{\mathrm{in}}(t) \tag{5.21}$$

$$\mathbf{a}_{\mathrm{out}}(t) = B^T \mathbf{a}(t) - \mathbf{a}_{\mathrm{in}}(t) \tag{5.22}$$

$$\mathbf{a} = (a, c, b)^T \tag{5.23}$$

$$\mathbf{a}_{\mathrm{in}} = (a_{\mathrm{in}}, a_{\mathrm{in}}^{\mathrm{N}}, c_{\mathrm{in}}, c_{\mathrm{in}}^{\mathrm{N}}, b_{\mathrm{in}}^{\mathrm{N}})^T \tag{5.24}$$

$$\mathbf{a}_{\mathrm{out}} = (a_{\mathrm{out}}, a_{\mathrm{out}}^{\mathrm{N}}, c_{\mathrm{out}}, c_{\mathrm{out}}^{\mathrm{N}}, b_{\mathrm{out}}^{\mathrm{N}})^T \tag{5.25}$$

$$A = \begin{pmatrix} -i\Delta_{\mathrm{opt}} - \frac{\kappa_{\mathrm{opt}}}{2} & 0 & ig_{\mathrm{om}} \\ 0 & -i\Omega_\mu - \frac{\kappa_\mu}{2} & ig_{\mathrm{em}} \\ ig_{\mathrm{om}} & ig_{\mathrm{em}} & -i\Omega_{\mathrm{m}} - \frac{\kappa_{\mathrm{m}}}{2} \end{pmatrix} \tag{5.26}$$

$$B = \begin{pmatrix} \sqrt{\kappa_{\mathrm{opt,c}}} & \sqrt{\kappa_{\mathrm{opt,i}}} & 0 & 0 & 0 \\ 0 & 0 & \sqrt{\kappa_{\mu,\mathrm{c}}} & \sqrt{\kappa_{\mu,\mathrm{i}}} & 0 \\ 0 & 0 & 0 & 0 & \sqrt{\Gamma} \end{pmatrix}, \tag{5.27}$$

where $\mathbf{a}$ is a vector for resonator mode operators, $\mathbf{a}_{\mathrm{in(out)}}$ is a vector of input (output) fields, and superscript N is the corresponding noise port ($a^{\mathrm{N}}_{\mathrm{in(out)}}$, $b^{\mathrm{N}}_{\mathrm{in(out)}}$, and $c^{\mathrm{N}}_{\mathrm{in(out)}}$). Note that in this analysis, we assume zero noise input.

In the frequency domain, we can reduce the expressions into a scattering matrix,

$$\mathbf{a}_{\mathrm{out}}(\omega) = S(\omega)\mathbf{a}_{\mathrm{in}}(\omega) \tag{5.28}$$

$$S(\omega) = B^T(-i\omega I - A)^{-1}B - I. \tag{5.29}$$

Using this scattering matrix, we can obtain various features that we can expect from our system, including OMIT, microwave-to-optical transduction, and optical-to-microwave transduction. Since we have previously solved for the OMIT spectrum in chapter 2, here we mainly focus on the transduction spectrum ($\eta(\omega) = |S_{\mathrm{oe}}(\omega)|^2 = |S_{\mathrm{eo}}(\omega)|^2$).

$$\eta(\omega) = \frac{\kappa_{\mathrm{opt,c}}}{\kappa_{\mathrm{opt}}}\frac{\kappa_{\mu,\mathrm{c}}}{\kappa_{\mu}}\left|\frac{\alpha(\omega)}{\beta(\omega)}\right|^2 \tag{5.30}$$

$$\alpha(\omega) = -2\sqrt{C_{\mathrm{em}}C_{\mathrm{om}}} \tag{5.31}$$

$$\begin{aligned}\beta(\omega) = {} & C_{\mathrm{em}}\left(1 - \frac{i(\omega - \Delta_{\mathrm{opt}})}{\kappa_{\mathrm{opt}}/2}\right) + C_{\mathrm{om}}\left(1 - \frac{i(\omega - \Omega_{\mu})}{\kappa_{\mu}/2}\right) \\ & + \left(1 - \frac{i(\omega - \Delta_{\mathrm{opt}})}{\kappa_{\mathrm{opt}}/2}\right)\left(1 - \frac{i(\omega - \Omega_{\mu})}{\kappa_{\mu}/2}\right)\left(1 - \frac{i(\omega - \Omega_{\mathrm{m}})}{\Gamma/2}\right).\end{aligned} \tag{5.32}$$

We observe peak conversion when the optical detuning, microwave mode, and acoustic mode are in resonance. Measuring transduction at this resonant frequency ($\omega = \Delta_{\mathrm{opt}} = \Omega_{\mu} = \Omega_{\mathrm{m}}$), we get

$$\eta = \eta_{\mathrm{opt}}\eta_{\mu}\frac{4C_{\mathrm{em}}C_{\mathrm{om}}}{(C_{\mathrm{em}} + C_{\mathrm{om}} + 1)^2}, \tag{5.33}$$

where η_μ is the microwave coupling efficiency, $\frac{\kappa_{\mu,c}}{\kappa_\mu}$. This is consistent with the expression for microwave-to-optical transduction efficiency in prior studies.

Chapter 6

Precision sensing of piezoelectricity

6.1 Introduction

Mechanical resonators are widely used as sensitive sensors, including the detection of weak forces [40], small masses [41], and even a single electron spin [42]. In prior works [54,55], it has been shown that Brillouin optomechanical systems with mechanical resonators can achieve strong coupling, where they reach high enough phonon sensitivity to detect thermal phonons at cryogenic temperatures. By simultaneously combining strong optomechanical coupling enabled through Brillouin scattering and piezoelectric interactions in an HBAR as described in chapter 5, one of our goals is to create a measurement tool for piezoelectrically driven phonons, sensitive enough to even detect anomalous piezoelectricity in inversion-symmetric crystals.

There is a strong motivation for this type of study, as parasitic piezoelectricity may be a relevant loss channel for emerging solid-state quantum technologies. In fact, in many of the systems combining superconducting qubits with piezoelectricity, people have reported qubit lifetimes of up to two orders of magnitude shorter compared to conventional transmons [7, 8, 27–33]. Even in qubit designs without any intentional electromechanical coupling components, anomalous piezoelectricity in qubit

substrates, if it exists, can lead to qubit dissipation, setting an intrinsic limit to qubit lifetimes [34,38]. An example of a dissipation model for a simplistic qubit design can be found in section 3.5. Anomalous piezoelectricity from nominally non-piezoelectric materials can originate from subsurface lattice damage, bulk defects/imperfections [35], built-in stress [36], or even the inherent asymmetry of the lattice boundary [34].

In this chapter, we build upon the hybrid cavity assembly described in chapter 5, and show its usage as a piezo-sensing platform. In particular, we demonstrate extremely high sensitivity by detecting anomalous piezoelectricity in CaF_2, a nominally non-piezoelectric material, and comparing the results with a more conventional means of piezo-sensing. This sensitivity, combined with the modular construction of the system, makes it an appealing tool to investigate electromechanical couplings in a variety of materials. Additionally, we provide a bound in anomalous piezoelectricity in Si, based on limited observations.

6.2 Experimental data

6.2.1 Control experiment: x-cut quartz in single-pass (lock-in) setup

Before attempting to detect anomalous piezoelectricity in a non-piezoelectric material, we first conduct a control experiment on a known piezoelectric material to validate the setup described in chapter 5. We choose x-cut quartz for this control experiment. X-cut quartz is a material with moderate piezoelectricity (2.3 pm/V) and its bulk acoustic properties are well studied [53, 56]. With x-cut quartz, we fabricate a plano-convex HBAR as laid out in chapter 4. The microwave component used is a re-entrant microwave cavity (figure 3.2b, 5.1c). The setup used is the lock-in apparatus for single-pass measurements (figure 5.6).

Characterization of the re-entrant microwave cavity used to piezoelectrically drive

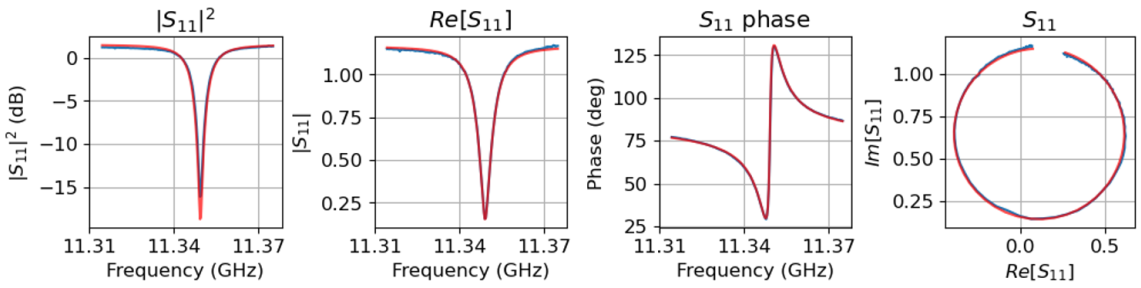

Figure 6.1: **Microwave cavity characterization for single-pass x-cut quartz experiment** S_{11} spectrum of the microwave cavity (re-entrant design) used for single-pass x-cut quartz experiment at cryogenic temperature (5 K). Blue is the measured data and red is the fit based on equation 5.3. The fit values are: $\Omega_\mu/2\pi = 11.35$ GHz, $\kappa_\mu/2\pi = 8.7$ MHz, $Q_\mu = 1300$, $\kappa_{\mu,\mathrm{c}}/2\pi = 4.5$ MHz, $Q_{\mu,\mathrm{c}} = 2500$, $\kappa_{\mu,\mathrm{i}}/2\pi = 4.2$ MHz, $Q_{\mu,\mathrm{i}} = 2700$.

the phonons in the system is shown in figure 6.1. The cavity is made out of OFHC copper, is centered around $\Omega_\mu/2\pi = 11.35$ GHz, and reaches a loss rate of $\kappa_\mu/2\pi = 8.7$ MHz ($\kappa_{\mu,\mathrm{c}}/2\pi = 4.5$ MHz, $\kappa_{\mu,\mathrm{i}}/2\pi = 4.2$ MHz), which corresponds to a quality factor of $Q_\mu = 1300$ ($Q_{\mu,\mathrm{c}} = 2500$, $Q_{\mu,\mathrm{i}} = 2700$). Note that the cavity undergoes contraction at cryogenic temperatures, leading to drifts in the resonance frequency and the coupling rate. This is accounted for and the cavity is adequately tuned as we assemble the apparatus at room temperature.

Once the system is set up and brought down to a cryogenic temperature (5 K) with a He-4 flow cryostat, we initially detect a photoelastic optomechanical response from the x-cut quartz without any microwave drive, following the measurement scheme in figure 5.6(a). The result of this measurement is shown in figure 6.2(a-b). By controlling the optical pump wavelength, we set the Brillouin frequency to match the m^{th} longitudinal phonon mode frequency ($\Omega_\mathrm{B} = \Omega_\mathrm{m} = 11.3495$ GHz). This maximizes the signals of acoustic resonances within the Brillouin bandwidth. We then confirm that the features we are observing are indeed phonon responses by comparing the detected acoustic FSR ($\Delta_\mathrm{m} = 5.7$ MHz) and transverse mode spacing (150 kHz) to theoretical predictions, both of which well-match. We also intentionally mismatch the pump and probe light polarizations, and check that the signal goes away. The uneven

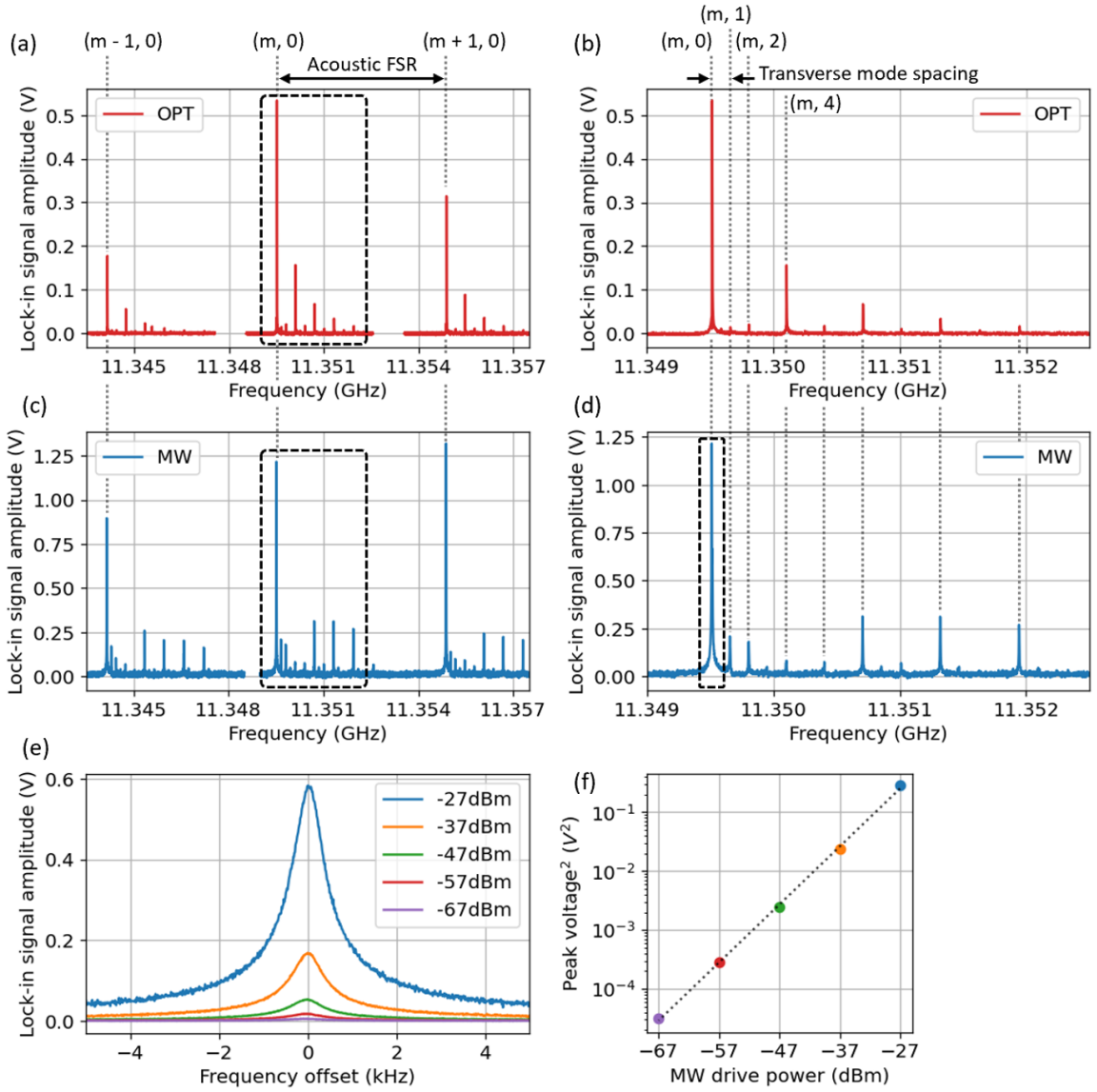

Figure 6.2: **Single-pass phonon spectroscopy of x-cut quartz measured with a lock-in amplifier at 5 K temperature (a)** Response from stimulated Brillouin scattering, where electrostrictively driven phonons photoelastically scatter the pump. The Brillouin frequency is set to match the m$^{\text{th}}$ longitudinal phonon mode frequency ($\Omega_{\text{B}} = \Omega_{\text{m}} = 11.3495$ GHz), such that the three families of resonances within the bandwidth are maximized (corresponding to m-1$^{\text{th}}$, m$^{\text{th}}$, and m+1$^{\text{th}}$ longitudinal modes). Phonon mode numbers of the response peaks are indicated as (longitudinal mode number, transverse mode number). Label 'OPT' indicates signals from optically driven phonons. Observed acoustic FSR (Δ_{m}) is 5.7 MHz, consistent with substrate thickness (L_{m}) of 0.5 mm. Observed acoustic linewidth (Γ) is 1.3 kHz. The center family of modes (m$^{\text{th}}$ longitudinal mode) within the dashed box is zoomed in and plotted in (b). **(Caption continued in next page)**

Figure 6.2: **(Caption continued from last page) (b)** Finer transverse mode structures are indicated up to the 5^{th} transverse mode. The uneven distribution of couplings to higher-order transverse modes mostly originates from fabricated HBAR device imperfections, and to a lesser degree from optical alignment. We observe transverse mode spacing of 150 kHz. **(c)** Brillouin scatter response from piezoelectric phonons. Label 'MW' indicates signals from microwave-driven phonons. Features closely resemble those in (a) with identical acoustic FSRs and linewidths. Longitudinal modes matching with those in (a) are compared with dotted lines. The center family of modes (m^{th} longitudinal mode) within the dashed box is zoomed in and plotted in (d). **(d)** Features closely resemble those in (b) with identical acoustic transverse mode spacing. Higher-order transverse modes matching with those in (b) are compared with dotted lines. (m,0)-th acoustic mode, marked with a dashed box, is further zoomed and shown in (e). **(e)** The zoomed-in spectrum of (m,0)-th acoustic response with varying microwave input power. In the legend is the microwave drive power in dBm. **(f)** Peak signal amplitudes from (e) are squared and plotted against the microwave drive power. The color of each datapoint matches that of (e). The dashed black line is a linear fit, indicating a linear relation between microwave drive power and detected signal power (slope of 0.99 ± 0.02 when y-axis is plotted in dB).

distribution of couplings to higher-order transverse modes mostly originates from fabricated HBAR device imperfections, and to a lesser degree from optical alignment. Note that the observed phonon linewidth of 1.3 kHz indicates a surface roughness limited HBAR, as the linewidth corresponds to a surface roughness of approximately 0.9 nm, consistent with the discussion on surface roughness induced loss in chapter 4. From the signals in figure 6.2(b), we obtain a single-photon optomechanical coupling rate of $g'_{\text{om},0}/2\pi = 130$ Hz $\pm 50\%$, which includes the theoretically predicted value of 158 Hz based on equation 2.26. Minor optical misalignment and pump/probe polarization mismatch possibly account for the slightly lower observed optomechanical coupling rate compared to theory.

Once phonon spectrum and optomechanical coupling are well understood, we switch to the piezoelectric phonon measurement scheme in figure 5.6(b). Besides the Brillouin frequency tuning, the microwave cavity is tuned to match the Brillouin-active phonon frequency ($\Omega_\mu \approx \Omega_{\text{m}}$). The measurement result is shown in figure 6.2(c-d). Compared to the previous optomechanically driven phonons response (figure

6.2a-b), we observe similar longitudinal and transverse phonon features with identical longitudinal acoustic FSR, transverse mode spacing, and phonon linewidth. Dotted black lines in the figure directly compare the results, highlighting the similarities. Thus, we can conclude that the observed signals are indeed features from phonons that are electromechanically driven.

To calculate the piezoelectric constant of x-cut quartz from the observed signal, we first convert the signal to the number of phonons in the system using equation 5.10. The number of photons circulating in the microwave cavity is given by equation 5.4. Combining the number of detected phonons and microwave photons, we can extract the electromechanical coupling rate from equation 3.9. From the data, we obtain an electromechanical coupling rate of $g_{\mathrm{em}}/2\pi = 2.85$ kHz (we used the theoretical value of $g'_{\mathrm{om}}/2\pi = 158$ Hz for this electromechanical analysis), corresponding to piezoelectric constant of 0.94 pm/V $\pm 50\%$ from equation 3.6. This closely matches with the literature value of cryogenic $d_{33} = 0.95$ pm/V for x-cut quartz [117], and the discrepancy is most likely due to an insignificant microwave/acoustic/optical mode mismatch. To confirm piezoelectricity as the primary source of electromechanical coupling, we record the phonon spectrum at several microwave drive powers (figure 6.2e-f). Here, we observe a linear relationship between the peak power and the microwave drive power as shown by the slope of 0.99 ± 0.02 in figure 6.2(f). This is a clear indicator of the piezoelectric effect, which is a linear electromechanical interaction.

From the x-cut quartz control experiment, we have validated the proposed piezo-Brillouin setup by successfully obtaining the optomechanical coupling rate and the electromechanical coupling rate of the substrate. Hence, we can now test the setup by probing an example of a non-piezoelectric substrate, CaF_2. For detailed parameter values for the measurements done in this section, see appendix A.

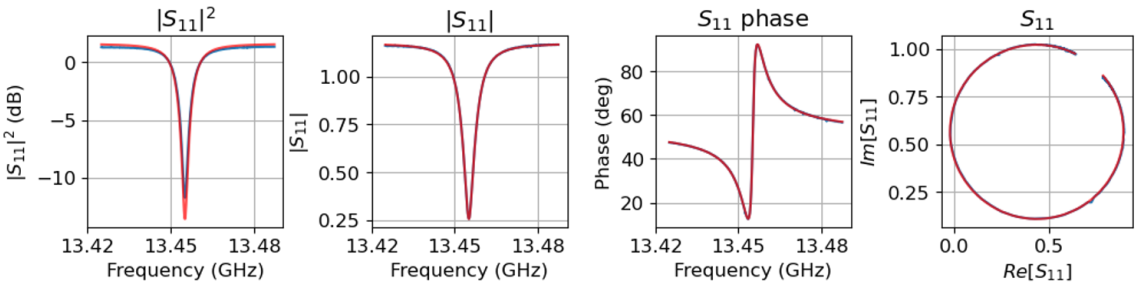

Figure 6.3: **Microwave cavity characterization for single-pass CaF_2 experiment** S_{11} spectrum of the microwave cavity (re-entrant design) used for single-pass CaF_2 experiment at cryogenic temperature (6 K). Blue is the measured data and red is the fit based on equation 5.3. The fit values are: $\Omega_\mu/2\pi = 13.455$GHz, $\kappa_\mu/2\pi = 7.2$ MHz, $Q_\mu = 1870$, $\kappa_{\mu,\mathrm{c}}/2\pi = 2.8$ MHz, $Q_{\mu,\mathrm{c}} = 4800$, $\kappa_{\mu,\mathrm{i}}/2\pi = 4.4$ MHz, $Q_{\mu,\mathrm{i}} = 3060$.

6.2.2 Anomalous piezo-measurement 1: CaF_2 in single-pass setup

CaF_2 is an inversion symmetric crystal, meaning that it should nominally be non-piezoelectric. For the purpose of testing our piezo-Brillouin platform, CaF_2 has a couple of advantages over other substrates. First, the Brillouin-active mechanical frequency for CaF_2 is ∼13.3GHz, which we can easily target with minimal changes in the setup used for x-cut quartz. Additionally, CaF_2 has a moderate photoelastic constant, approximately 60% of that of quartz, meaning that we should be able to reliably obtain Brillouin scattered signals from CaF_2.

The setup of the lock-in detection follows figure 5.6, with hybrid cavity design in figure 5.1(c). The microwave component used here is a re-entrant microwave cavity made out of OFHC copper (figure 6.3). It is centered around $\Omega_\mu/2\pi = 13.455$ GHz and reaches a loss rate of $\kappa_\mu/2\pi = 7.2$ MHz ($\kappa_{\mu,\mathrm{c}}/2\pi = 2.8$ MHz, $\kappa_{\mu,\mathrm{i}}/2\pi = 4.4$ MHz), which corresponds to a quality factor of $Q_\mu = 1870$ ($Q_{\mu,\mathrm{c}} = 4800$, $Q_{\mu,\mathrm{i}} = 3060$).

Similar to the x-cut quartz control experiment, we begin with stimulated Brillouin scattering measurement using a lock-in detection scheme (figure 5.6a) at cryogenic temperature (6 K), where we detect the response from photoelastically driven phonons (figure 6.4a-b). Within the Brillouin bandwidth, we find signals with frequency spac-

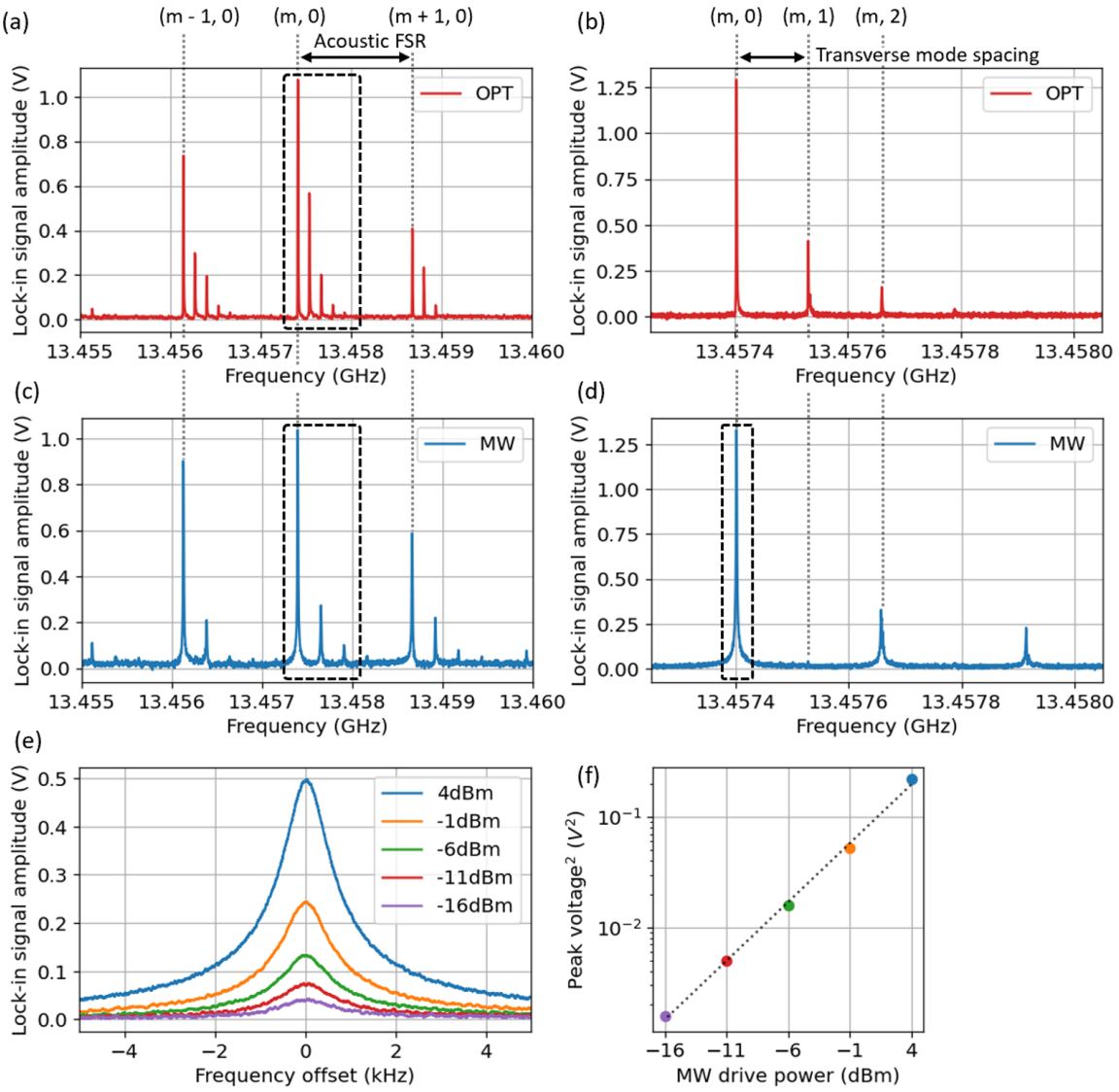

Figure 6.4: **Single-pass phonon spectroscopy of CaF_2 measured with a lock-in amplifier at 6 K temperature (a)** Response from stimulated Brillouin scattering. The Brillouin frequency is set to match the mth longitudinal phonon mode frequency ($\Omega_B = \Omega_m = 13.457$ GHz), such that the three families of resonances within the bandwidth are maximized (m-1th, mth, and m+1th longitudinal modes). Phonon mode numbers of the response peaks are indicated as (longitudinal mode number, transverse mode number). Label 'OPT' indicates signals from optically driven phonons. Observed acoustic FSR (Δ_m) is 1.3 MHz, which is consistent with substrate thickness (L_m) of 3 mm. The observed acoustic linewidth (Γ) is 1.7 kHz. The center family of modes (mth longitudinal mode) within the dashed box is zoomed in and plotted in (b). **(b)** Finer transverse mode structures are indicated up to the 3rd transverse mode, with transverse mode spacing of 130 kHz. **(c)** Brillouin scatter response from piezoelectric phonons. **(Caption continued in next page)**

Figure 6.4: **(Caption continued from last page)** Label 'MW' indicates signals from microwave-driven phonons. Features closely resemble those in (a) with identical acoustic FSRs and linewidths. Longitudinal modes matching with those in (a) are compared with dotted lines. The center family of modes (m^{th} longitudinal mode) within the dashed box is zoomed in and plotted in (d). **(d)** Features closely resemble those in (b) with identical acoustic transverse mode spacing. Higher-order transverse modes matching with those in (b) are compared with dotted lines. Due to the symmetry existing in microwave mode, we drive every other transverse mode. (m,0)-th acoustic mode, marked with a dashed box, is further zoomed and shown in (e). **(e)** The zoomed-in spectrum of (m,0)-th acoustic response with varying microwave input power. In the legend is the microwave drive power in dBm. **(f)** Peak signal amplitudes from (e) are squared and plotted against the microwave drive power. The color of each datapoint matches that of (e). The dashed black line is a linear fit, indicating a linear relation between microwave drive power and detected signal power (slope of 1.06±0.03 when y-axis is plotted in dB).

ings matching the predicted values for acoustic FSR ($\Delta_m = 1.3$ MHz) and transverse mode spacing (130 kHz). We also check that the signals disappear as we intentionally mismatch the pump/probe polarizations to confirm that we are indeed detecting a phonon response. Linewidths of the phonon modes are 1.7 kHz, corresponding to a reasonable surface roughness of 2.3 nm. Furthermore, the single-photon optomechanical coupling rate obtained from the signal is $g'_{om,0}/2\pi = 26$ Hz $\pm 50\%$, which is close to the theoretical value of 29 Hz based on equation 2.26. We expect minor optical misalignment and pump/probe polarization mismatch possibly explain the slightly lower observed optomechanical coupling rate compared to theory.

Finally, we switch the apparatus to the piezoelectric drive configuration and look for any phonon response caused by a microwave drive at the Brillouin frequency. The results are presented in figure 6.4(c-d), where we clearly see microwave-driven motion, indicating a measurable electro-mechanical coupling. The detected signal only exists at the Brillouin frequency and has features such as acoustic FSRs and transverse mode spacings, indicating that it is indeed a mechanical response. This rules out the possibility that the response is originating from an unexpected electro-optical coupling. Note that we only observe every other transverse mode. This is because

the symmetry of microwave drive prohibits coupling to odd transverse modes, which follows the Hermite-Gaussian bases [53]. This feature is absent in x-cut quartz data (figure 6.2), since the x-cut quartz device was not as cylindrically symmetric as the CaF_2 device, leading to microwave excitation of odd transverse acoustic modes in x-cut quartz. As shown in figure 6.4(e-f), we also observe the linear dependence of signal power to microwave drive power. This means that what drives phonons in our system is a linear electromechanical coupling. We refer to this coupling as anomalous piezoelectricity, although the innate mechanisms to such effect are uncertain (e.g. charged surfaces and crystal defects).

Calculating the coupling rate of the electromechanical interaction as we did in the previous section on x-cut quartz, we get a small value of $g_{\mathrm{em}}/2\pi = 2.8$ Hz. Following equation 3.6, we can correlate the coupling rate with an effective piezoelectric constant assuming for both bulk and surface piezoelectricity. For bulk piezoelectricity, this corresponds to a piezoelectric constant of $d_{33} = 1.47$ fm/V, which is much weaker compared to that of nominal piezoelectric materials. On the other hand, we can assume that the piezoelectricity is concentrated within a 1 nm surface layer. In such a case, the surface piezoelectric region requires a piezoelectric constant of 43 pm/V, which is rather unreasonable since such a strong piezoelectricity, if it exists, would have already been easily detected through other conventional means.

Therefore, our observations of anomalous piezoelectricity in CaF_2 indicate an effective piezoelectric coefficient between 1.47 fm/V and 43 pm/V, depending on how the phonon emitting sites are distributed, with a heavy bias towards bulk piezoelectricity with a value closer to the lower 1.47 fm/V. For detailed parameter values for the measurements done in this section, see appendix A.

6.2.3 Anomalous piezo-measurement 2: Finding bounds in Si anomalous piezoelectricity

Now that we have demonstrated the detection of anomalous piezoelectricity in CaF_2, a nominally non-piezoelectric material, we are ready to test our primary substrates of interest, Si. Si is a widely used substrate for integrated circuits and is also commonly used as a qubit substrate. Although it is an inversion symmetric crystal with no piezoelectricity, it is of interest to look for the existence of anomalous piezoelectricity since even weak piezoelectricity can lead to qubit decoherence as discussed in chapter 3.

The Brillouin frequency of Si is $\sim$ 37.7 GHz. Our single-pass measurement configuration (figure 5.6) is minimally modified to operate at such a high frequency. Signal generator #2 (SIG2) now generates a $\sim$ 18.8 GHz tone, and we use the second overtone generated by the phase modulator (PM) to create a probe/LO tone $\sim$ 37.7 GHz away from the pump. A microwave doubler is also added in front of the microwave cavity such that the $\sim$ 18.8 GHz tone from SIG2 can be doubled to $\sim$ 37.7 GHz to correctly excite Brillouin-active phonons.

Then, we proceed to characterize the cavities and the interactions through the system. For the microwave component, we use a TE130 mode of an OFHC copper rectangular cavity (figure 5.1b). Microwave cavity of the system exhibit $\kappa_{\mu,\mathrm{i}} = 144$ MHz ($Q_{\mu,\mathrm{i}} = 260$) and $\kappa_{\mu,\mathrm{c}} = 70$ MHz ($Q_{\mu,\mathrm{c}} = 540$). The relatively low Q-factor stems from the challenge of designing a high-frequency microwave cavity. Due to the reduced dimensions required to create high-frequency modes, sections contributing to the loss (such as seam, metal oxide, etc) have higher participation than standard $<$ 10 GHz designs.

Through all-optical stimulated Brillouin scattering, we identify the acoustic properties of the system. With a plano-convex HBAR fabricated on a 1 mm thick (L_m) float-zone high resistivity (R $>$ 10,000 Ω·cm) Si, we observe Γ of 45 kHz (figure 6.5a).

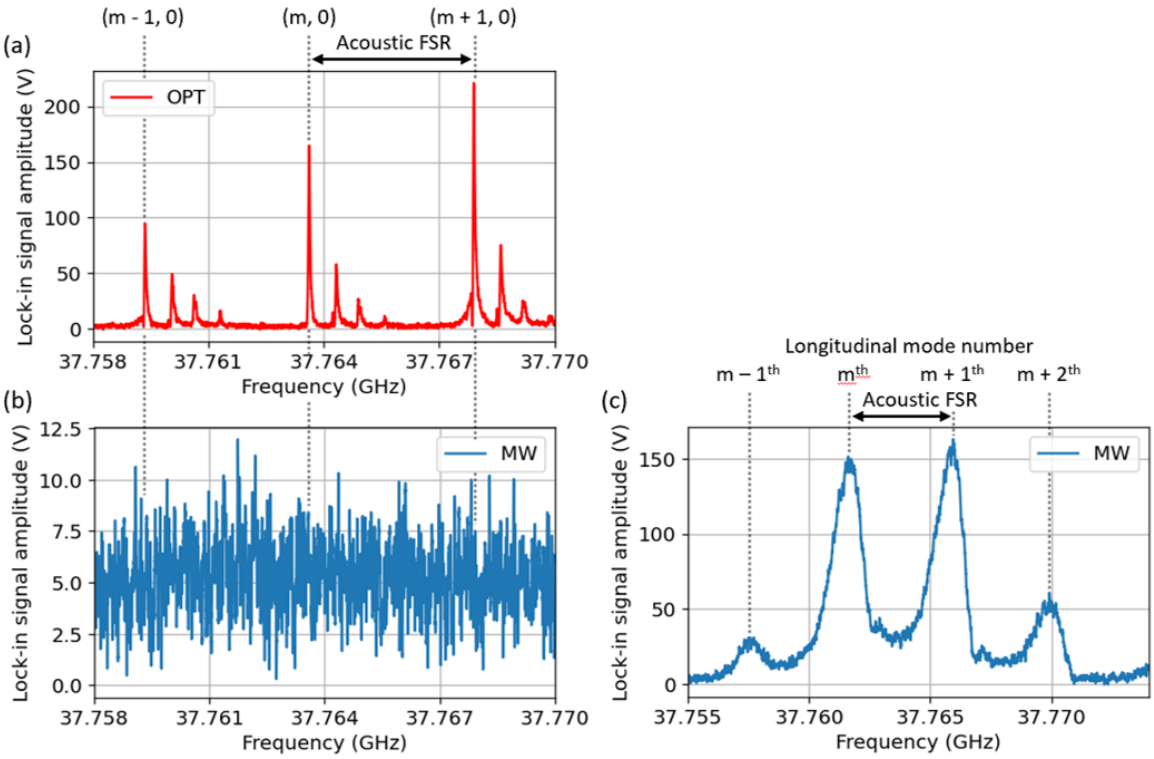

Figure 6.5: **Single-pass phonon spectroscopy of Si measured with a lock-in amplifier at 10 K temperature (a)** Response from stimulated Brillouin scattering in plano-convex Si HBAR. The Brillouin frequency is set to match the m^{th} longitudinal phonon mode frequency ($\Omega_B = \Omega_m = 37.764$ GHz), such that the three families of resonances within the bandwidth are maximized (m-1^{th}, m^{th}, and m+1^{th} longitudinal modes). Phonon mode numbers of the response peaks are indicated as (longitudinal mode number, transverse mode number). Label 'OPT' indicates signals from optically driven phonons. Observed acoustic FSR (Δ_m) is 4 MHz, which is consistent with substrate thickness (L_m) of 1 mm. The observed acoustic linewidth (Γ) is 45 kHz. **(b)** Brillouin scatter response from the same substrate as in (a) when microwave drive is present. Label 'MW' indicates microwave driven is on. we do not see any phonon response here. With the noise floor, we can calculate a bound in anomalous piezoelectricity in Si, which corresponds to $d_{33} = 1.2$ fm/V assuming bulk piezoelectricity and $d_{33} = 6$ pm/V assuming surface piezoelectricity ($t_{pz} = 1$ nm). **(c)** Brillouin scatter response from piezoelectric phonons in flat-flat Si HBAR with 150 nm AlN layer. Observed acoustic FSR is 4 MHz, consistent with 1 mm substrate thickness. Observed acoustic linewidth is $\sim$ 1.5 MHz. The signal can be converted into a piezoelectric constant of $\sim$ 1 pm/V, which is close to the literature value of the AlN piezoelectric constant, 5.1 pm/V.

Moreover, the response can be correlated with an optomechanical coupling rate of $g'_{\mathrm{om}}/2\pi = 37$ Hz $\pm 50\%$, close to the theoretically calculated (equation 2.26) 42 kHz.

Switching the setup to allow a microwave drive tone to enter the cavity, we search for any Brillouin optomechanical response from piezoelectrically driven phonons. Figure 6.5(b) presents our efforts in searching for such a signal. Unfortunately, (or fortunately from the perspective of a qubit) we did not observe any noticeable signal. To confirm that the null response of figure 6.5(b) is indeed valid, we made a measurement with an AlN on Si flat-flat HBAR (figure 6.5c), where a 150 nm piezoelectric AlN layer drives 37 GHz Brillouin active phonons in Si (AlN film thickness measured using ellipsometry). Here we obtain an electromechanical coupling rate of $g_{\mathrm{em}}/2\pi = 2$ kHz, corresponding to 1 pm/V of piezoelectricity. This lower detected value of piezoelectricity compared to the literature value of 5.1 pm/V is most likely a result of poor AlN layer quality, as we are able to visibly notice grains on the surface of AlN through a microscope.

Returning to the anomalous piezoelectricity measurement in Si, we are still able to calculate an upper bound in Si anomalous piezoelectricity based on the noise recorded. Using the theoretical value of optomechanical coupling rate ($g'_{\mathrm{om}}/2\pi = 42$ kHz), we calculate a bound in electromechanical coupling rate, $g_{\mathrm{em}}/2\pi = 3.5$ Hz, from the noise. From equation 3.6, this electromechanical coupling rate corresponds to either a bulk piezoelectric value of 1.2 fm/V or a surface piezoelectric value of 6 pm/V across a 1 nm thin surface. With the literature material properties of Si, we then follow the work laid out in 3.5.2 to obtain the qubit T_1 correlated with the piezoelectricity values. In the case of bulk piezoelectricity, this results in a qubit T_1 bound of 290 ms, whereas the surface (1 nm thick) piezoelectricity case gives a bound of 4 ms. Note that the surface piezo-limited bound of qubit T_1 is only an order of magnitude higher than the current limit in qubit T_1 of ~ 0.3 ms [79]. With weak photoelastic properties of Si limiting the piezo-detection sensitivity of the device, we

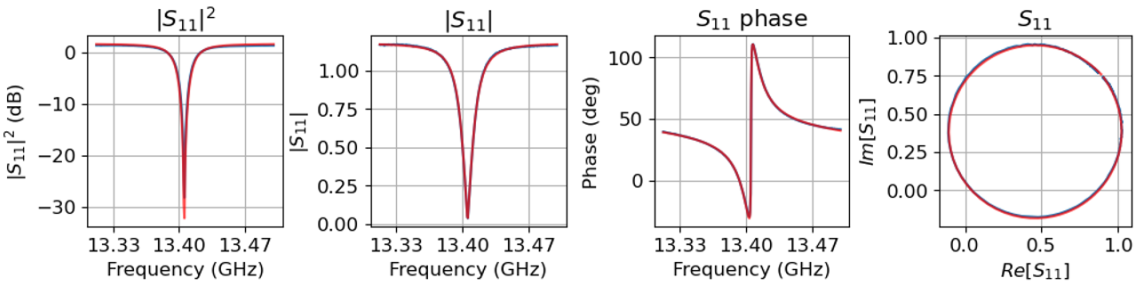

Figure 6.6: **Microwave cavity characterization for optical cavity-enhanced CaF_2 experiment** S_{11} spectrum of the microwave cavity (coaxial design) used for optical cavity-enhanced CaF_2 experiment at cryogenic temperature (8.7 K). Blue is the measured data and red is the fit based on equation 5.3. The fit values are: $\Omega_\mu/2\pi$ = 13.405 GHz, $\kappa_\mu/2\pi$ = 22.4 MHz, Q_μ = 600, $\kappa_{\mu,\mathrm{c}}/2\pi$ = 10.9 MHz, $Q_{\mu,\mathrm{c}}$ = 1230, $\kappa_{\mu,\mathrm{i}}/2\pi$ = 11.5 MHz, $Q_{\mu,\mathrm{i}}$ = 1160.

seek to improve our platform for higher sensitivity such that it can give a high enough bound in anomalous piezoelectricity limited qubit T_1 to not realistically impact any of the qubit devices in the future. This motivates us to incorporate an optical cavity to take advantage of resonant enhancement, as discussed in section 5.3.1. For detailed parameter values for the measurements done in this section, see appendix A.

6.2.4 Anomalous piezo-measurement 3: CaF_2 in optical cavity enhanced setup

Resonant enhancement enabled by integrating an optical cavity into the setup allows for detections with higher sensitivity compared to the single-pass case. With an optical cavity added to the setup, it is more intuitive and convenient for us to perform direct measurement of signal, following the apparatus shown in figure 5.7. The design of the hybrid cavity assembly is shown in figure 5.1(d), where an acoustic substrate is placed above the pin of a coaxial microwave resonator and between a Fabry-Pérot optical cavity. We demonstrate the detection of anomalous piezoelectricity in CaF_2 to compare with the previous single-pass measurements.

We begin the experiment by characterizing the resonator components of the hybrid

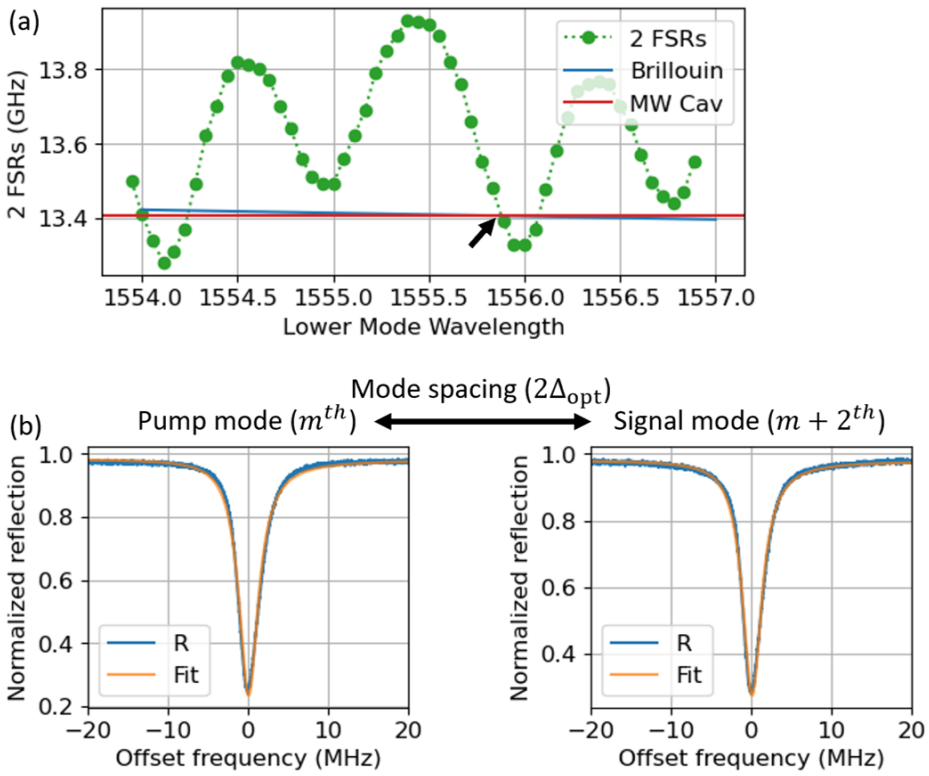

Figure 6.7: **Optical cavity characterization for optical cavity-enhanced CaF_2 experiment at 8.7 K temperature** (a) The plot of optical mode spacing ($2\Delta_{opt}$) versus the lower frequency of the optical mode pair (green), expected Brillouin frequency of CaF_2 (blue), and microwave cavity resonant frequency (red). Optical mode spacing is obtained between a pair of resonances that are 2 modes apart. The dotted green line is a guide to the eye highlighting the range at which optical mode spacings vary. Optical cavity mode spacings can be further fine-tuned using a piezo-actuator installed between the optical cavity. We choose to operate where the Brillouin frequency, microwave cavity resonance, and optical mode spacings intersect, marked with a black arrow. (b) The normalized reflection spectrum of the optical cavity. Pump/signal modes are chosen to be the mode pair indicated with a black arrow in (a), whose mode spacing $2\Delta_{opt}$ matches with the Brillouin spacing and microwave cavity resonance. Blue is the reflection data and orange is the fit obtained through the input-output relation of a Fabry-Pérot cavity (See footnote). Fit values are: $\kappa_{opt}/2\pi$ = 2.1 MHz, $\kappa_{opt,c}/2\pi$ = 0.6 MHz, $\mathcal{F}$ = 3200.

cavity. First, the coaxial microwave cavity is made out of OFHC copper, and its S_{11} reflection spectrum at cryogenic temperature (8.7 K) is given in figure 6.6. Note that it is vital to tune the cavity frequency to match the resonances of other cavities as explained in section 5.2.2. We change the length of the center pin of the coaxial cavity to optimize the microwave cavity frequency.

Then we have the acoustic cavity element - HBAR. Unlike in the previous section, we use a CaF_2 HBAR with flat-flat geometry. This results in an acoustic lifetime that is diffraction limited. Techniques to integrate a plano-convex HBAR within an optical cavity are currently being pursued in the lab, but are not implemented in this experiment. However, if we can reach high detection sensitivity without requiring plano-convex fabrication, flat-flat geometry has several added benefits such as material choice flexibility and simplified assembly. Characterization of acoustic linewidth is done through OMIT measurement (figure 6.8) which is further discussed in the following paragraphs.

The last cavity component requiring characterization is the Fabry-Pérot optical cavity (figure 6.7). It is composed of two mirrors - one flat and one concave - both with 99.9% reflectivities. The expected value of finesse is 3140 from equation 5.7, meanwhile we obtain $\mathcal{F} = 3200$ from measurement[1]. As explained in chapter 5, we have to find a pair of modes with frequency spacing matching the Brillouin frequency. This is readily achieved through the vacuum/dielectric composition of the optical cavity in addition to a piezo-actuator controlling the optical cavity length (see figure 5.4). Applying this to the current experiment, figure 6.8(a) well illustrates this process of finding the optimal optical cavity mode pair. We also notice from data that shrinkage of cavity geometry at cryogenic temperature has minimal effect on optical cavity dissipation.

With the microwave/acoustic/optical cavity components in place, we characterize the optomechanical interaction through OMIT. We have previously introduced ways to understand an OMIT spectrum in section 2.4.1. We fit the data in figure 6.8, to equation 2.34, from which we obtain respectable optomechanical cooperativity of $C_{\mathrm{om}} = 0.705$ and optomechanical coupling rate of $g_{\mathrm{om}}/2\pi = 385$ kHz at a moderate optical

1. Finesse can be obtained by fitting the reflection and transmission spectrum of a Fabry-Pérot cavity mode, given via input-output formalism as [55],
$R(\omega) = \left|\frac{i(\omega-\omega_{\mathrm{opt}})-\kappa_{\mathrm{opt}}/2+\kappa_{\mathrm{opt,c}}}{\kappa_{\mathrm{opt}}/2-i(\omega-\omega_{\mathrm{opt}})}\right|^2$, $T(\omega) = \left|\frac{\kappa_{\mathrm{opt,c}}}{\kappa_{\mathrm{opt}}/2-i(\omega-\omega_{\mathrm{opt}})}\right|^2$.

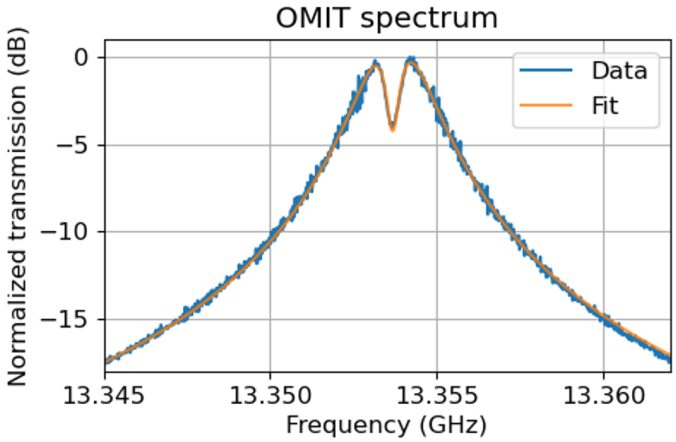

Figure 6.8: **OMIT spectrum with CaF_2 at 8.7 K temperature** Data is shown in blue and fit is shown in orange. Fit values are: $\Omega_m/2\pi$ = 13.354 GHz, $2\Delta_{opt}/2\pi$ = 13.354 GHz, $\Gamma/2\pi$ = 400 kHz, $\kappa_{opt}/2\pi$ = 2.1 MHz, $\mathcal{F}$ = 3200. $g_{om}/2\pi$ = 385 kHz, C_{om} = 0.705. This OMIT data is for microwave-driven motion measurement, taken with P_p (optical pump power) = 23 mW.

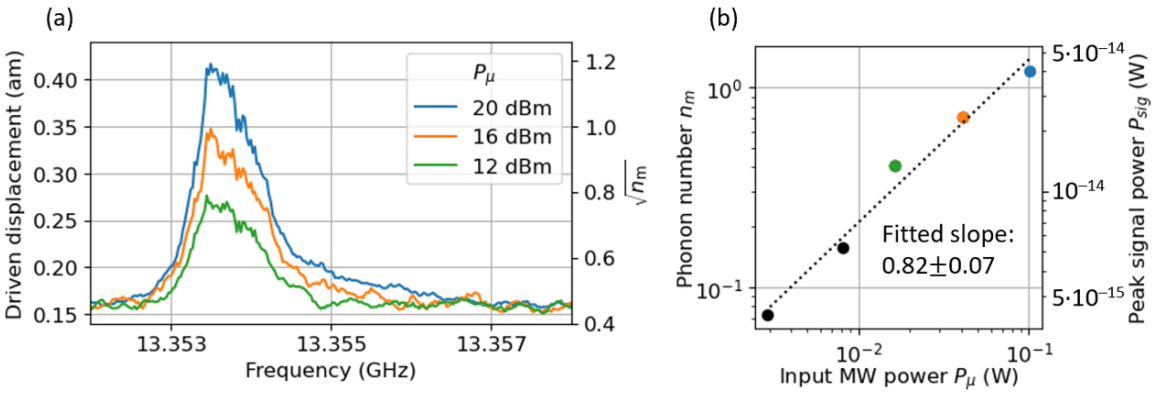

Figure 6.9: **Spectroscopy of anomalous piezoelectricity in CaF_2** (a) Coherent, cavity-enhanced optical spectroscopy of microwave-driven motion in CaF_2 at 8.7K temperature. The amplitude of driven motion (characterized by displacement and $\sqrt{n_m}$) is calculated from the detected optical signal. Legend indicates microwave power launched into the system. (b) Relation between the peak-driven motion and microwave power. The driven motion is represented in units of phonon number and signal power. To obtain the driven motion, background noise is subtracted from the peak signal in (a). The color of each datapoint matches that of the main graph. Black points are not plotted in (a). The black dashed line is a fit, giving a power relation, $n_m \propto P_\mu^{0.82\pm0.07}$. Adapted from Ref. [57].

pump power $P_{\mathrm{p}} = 23$ mW. Additionally, we find acoustic linewidth of $\Gamma/2\pi = 400$ kHz, which corresponds to a diffraction-limited linewidth as expected from a flat-flat HBAR.

After characterizing the cavity components and the optomechanical coupling, we apply a microwave drive at the CaF_2 Brillouin frequency and look for an optical response scattered via phonons. The results of this experiment are shown in figure 6.9(a), where we clearly see non-zero microwave-driven motion, indicating a measurable electro-mechanical coupling. Optical signals from driven motions are converted to displacements and phonon numbers through equation 5.15. Similar to the previous observations from CaF_2 single-pass experiment, the detected signal only exists at the Brillouin frequency, indicating that it is indeed a mechanical response. This rules out the possibility that the response is coming from another source such as electro-optical coupling. Looking at the phonon response in relation to input microwave power (figure 6.9b), we notice a power relation of $n_{\mathrm{m}} \propto P_{\mu}^{0.82\pm0.07}$. Although this is fairly close to a linear relation ($n_{\mathrm{m}} \propto P_{\mu}$) expected from a piezoelectric response, the minor deviation can be attributed to unaccounted noises raising the noise floor and contributions from unaccounted weaker lower order effects since we expect the anomalous piezoelectric effect to be extremely weak. Subtracting background noise (consisting of shot noise and detector noise) and thermal noise from the response shown in figure 6.10, we detect coherent acoustic response corresponding to n_{m}=1.2, or a peak displacement for our acoustic standing wave of 0.25 am. This corresponds to an extremely small effective electromechanical coupling rate of $g_{\mathrm{em}}^{\mathrm{CaF_2}}/2\pi = 0.03$ Hz.

This effective piezoelectricity could be attributed to imperfections distributed in the bulk or concentrated at the surface. If the acoustic response was derived from a piezoelectric coupling across a thin surface layer of 1 nm, it would correspond to an effective piezoelectric constant of $d_{33} = 2.44$ pm/V (comparable to common piezoelectric materials). However, such a large piezoelectric coefficient would be inconsis-

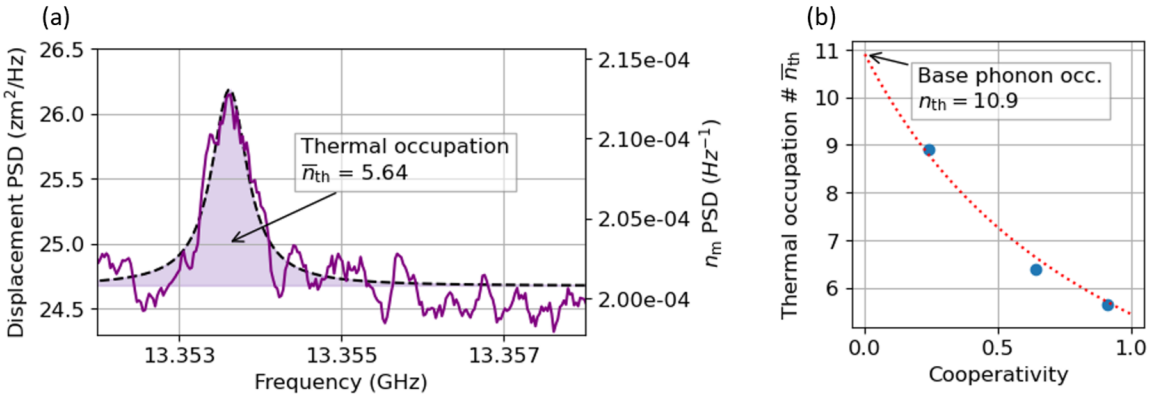

Figure 6.10: **Effective thermal phonon occupation in CaF_2 at 8.7 K temperature** PSD: power spectral density. (a) Amplitude spectral density of spontaneous (thermal) motion in CaF_2 at 8.7 K temperature. The maximum optical pump power used in the measurement is 30.1 mW, corresponding to cooperativity of $C_{om} = 0.914$. The response is fitted with a Lorentzian (dashed black line) with 535 kHz linewidth and the shaded area under the curve is integrated to obtain an effective thermal occupation of $\bar{n}_{th} = 5.64$. The peak of the Lorentzian fit indicates the detection sensitivity, corresponding to 2.13×10^{-4} phonons/Hz (b) Effective thermal occupation at multiple optomechanical cooperativities (blue) is fitted with a phonon cooling expression in equation 6.1 (red). The base thermal phonon number at C_{om} is $n_{th} = 10.9$. Adapted from Ref. [57].

tent with other investigations into CaF_2 [35], and quantitative interferometric-based piezo force microscopy (IDS-PFM) [118, 119] measurements conducted on this sample (which revealed no signal, see section 6.3). Alternatively, if it is derived from a uniform piezoelectric coupling distributed through the bulk of the crystal [35–37], it would correspond to a weak effective d_{33} of 83 am/V, which would be consistent with the previously mentioned null results from IDS-PFM (given measurement noise floor of 55 fm/V). To explain this effective bulk property, one might consider an ensemble of polar defects, which effectively act as piezoelectric emitters. Such a mechanism could be intrinsically linked to dielectric loss, motivating further study, particularly in the context of solid-state qubit decoherence.

The fundamental noise floor of this technique is ultimately limited by the thermal noise of the acoustic resonator, which we can detect in the absence of the microwave drive (see figure 6.10). The effective thermal motion we detect corresponds to an

average occupation of $n_{\mathrm{th}} = 5.64$ at $C_{\mathrm{om}} = 0.914$. Since the optomechanical cooperativity of the system is fairly large ($C_{\mathrm{om}} \sim O(0.1)$), we observe laser cooling of the thermal population. Fitting the effective thermal phonon data to the expression for laser-cooled thermal phonon occupancy [4],

$$\bar{n}_{\mathrm{th}} = n_{\mathrm{th}} \frac{1}{1 + C_{\mathrm{om}}}, \tag{6.1}$$

we obtain a base thermal phonon number of $n_{\mathrm{th}} = 10.9$ at $C_{\mathrm{om}} = 0$ (see figure 6.10b). At the temperature of the cryostat (8.7 K), this value should be equal to 13 ($n_{\mathrm{th}} = (e^{\hbar\Omega_{\mathrm{m}}/k_{\mathrm{B}}T} - 1)^{-1}$). The observed thermal phonon number is slightly lower than the expected value because of the location of the thermometer. We clamped the thermometer at the hottest surface of the hybrid cavity to avoid underestimating the system temperature. As a result, the acoustic substrate is highly likely to be sitting at a slightly lower temperature than what we read from the thermometer, explaining the slightly lower thermal occupation than theory. Note that we observe no significant heating despite $>$ 10mW of input pump power, highlighting the good thermal anchoring and minimal absorption in this bulk platform. On resonance, this thermal-limited noise floor is 162 zm (i.e. noise floor of 5.12 zm$\cdot$Hz$^{-1/2}$ or 0.21 phonons) in the 1kHz bandwidth of our driven measurement, which corresponds to a piezoelectric coefficient sensitivity of 7 am/V, or 2.2 am/V at a bandwidth of 100 Hz, in the case of an evenly distributed bulk piezoelectricity. This compares favorably to existing techniques for probing piezoelectricity, such as resonant piezoelectric spectroscopy (RPS), resonant ultrasound spectroscopy (RUS) [35], and PFM [118,119]. Critically, our technique extends this sensitivity to GHz frequencies and cryogenic temperatures. Applying this new materials analysis tool to materials like silicon, sapphire, and diamond can be of immediate relevance to quantum technologies [32,34,38,39,120].

To conclude, the hybrid piezo-Brillouin platform is a sensitive tool to detect piezo-

electricity at cryogenic temperatures in GHz frequency regime, especially when the resonant enhancement of signal is in place. We demonstrate this by observing a linear electromechanical coupling in CaF_2, which is most likely caused by an anomalous piezoelectric effect. The electromechanical coupling we detect corresponds to an effective bulk piezoelectric constant of 83 am/V. Notice that this value is different from the result in section 6.2.2. Since we used different CaF_2 substrates from separate vendors in these experiments, the difference in piezoelectricity implies that there are variations even within the same type of substrate if they are prepared and processed differently, further consolidating the anomalous nature of piezoelectricity we are detecting in our demonstrations. For detailed parameter values for the measurements done in this section, see appendix A.

6.3 Alternative measurement: Piezoresponse Force Microscopy (PFM)

Piezoresponse Force Microscopy (PFM) is a method of detecting piezoelectricity in $\sim$ 100 nm depth [118, 119, 121]. The substrate is put under an AC electric field (usually in the range of $\sim$100 kHz), which leads to a piezoelectric deformation due to the converse piezoelectric effect. This deformation is mapped with a probe cantilever across the substrate. Recently an interferometric displacement sensing approach to PFM (IDS-PFM) has been developed which allows quantitative determination of out-of-plane electromechanical responses [118, 119]. This method removes many of the artifacts that plague traditional PFM, and is made inherently quantitative via the interferometric readout. Collaborating with Oak Ridge National Lab (ORNL), we had a chance to perform IDS-PFM measurement on a CaF_2 substrate.

We put the same CaF_2 that we study in section 6.2.4 under an IDS-PFM as a way to alternatively detect piezoelectricity (see Figure 6.11). The frequency of the

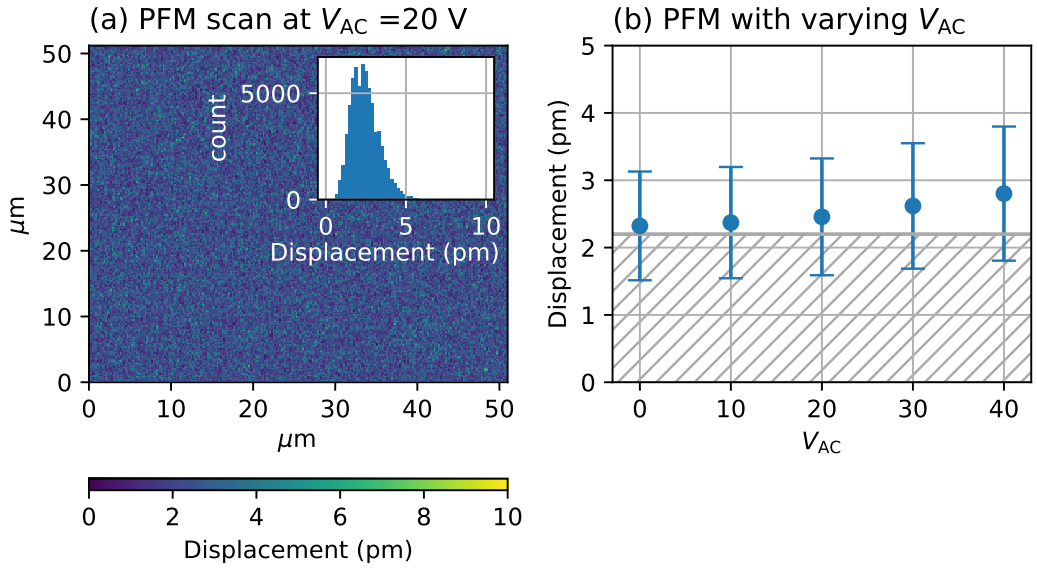

Figure 6.11: **PFM scan of CaF_2** PFM scan is performed across a 50 um×50 um surface of CaF_2. CaF_2 used here is the same substrate used in section 6.2.4. (a) Example measurement at $V_{AC} = 20$ V. Histogram of detected displacement is shown in the inset. (b) The average of displacement data is plotted with its standard deviation at various V_{AC}. The displacement noise floor of ∼2.2 pm is indicated in dashed grey. Minimal variability in detected displacement indicates piezoelectricity smaller than the device's detection sensitivity. Adapted from Ref. [57].

AC field is ∼100 kHz. We measure a white noise floor of ∼70 fm/$\sqrt{\text{Hz}}$, which is equivalent to a displacement noise floor of ∼2.2 pm in an imaging bandwidth of 1kHz. For a 1 V drive amplitude, this yields a minimum detectable piezo-sensitivity of $d_{\text{eff}} = 2.2$ pm/V. Minimum detectable piezo-sensitivity can be lowered by simply applying a larger drive voltage which was allowable in the case of CaF_2, unlike thin films or materials having low dielectric breakdown potentials. For a maximum applied voltage of 40 V, this implies a minimal detectable d_{eff} of 55 fm/V. From the data, we barely see any deviation from the ∼2.2 pm background. Even though the data may appear to have a non-zero slope (14 ± 40 fm/V), it is inconclusive that we detect any piezoelectricity since all data are within the standard deviation/error bar. We attribute the smaller but finite slope of 14 fm/V to the influence of electrostatic forces. At high voltage especially, we can expect non-negligible electrostatic forces and force gradients to act between the AFM tip and sample, which may lead to a

small but finite displacement of the tip position, even for the case of IDS-PFM (which is largely insensitive to cantilever-sample electrostatic effects [118, 119]). We further note that using softer (3 nN) cantilevers than the one used in Figure 6.11 ($\sim$42 nN) leads to a clear enlargement of the measured displacement (slope of 290 ± 80 fm/V) as would be expected for an electrostatic effect.

Therefore, we observe no detectable piezoelectricity though IDS-PFM, meaning that parasitic piezoelectricity in CaF_2 is smaller than the detection limit of 55 fm/V. These results indicate the unlikelihood of the parasitic piezoelectricity coming from an intrinsic surface layer, which requires piezoelectricity to be $\gtrsim 1$ pm/V. Instead, it is more likely that the parasitic piezoelectricity detected in CaF_2 is originated from the bulk of the crystal.

6.4 Outlook/conclusion

In this chapter, we have shown an application of our hybrid piezo-Brillouin platform as a highly sensitive piezo-sensor. We demonstrate that the device correctly predicts the piezoelectricity of x-cut quartz and of the damaged layer of AlN.

Extending the investigation to materials that are nominally non-piezoelectric, we discover anomalous piezoelectricity in CaF_2. Especially in the resonantly enhanced detection, we are able to conduct precision spectroscopy of GHz motion with sub-quanta sensitivity (i.e. a noise floor of 5.12 zm$\cdot$Hz$^{-1/2}$), allowing piezo-coefficient sensitivity of 2.2 am/V (at 100 Hz bandwidth), and spontaneous detection of thermal phonons at a cryogenic temperature. Depending on the CaF_2 substrate, we measure electromechanical couplings ranging from 2.8 Hz to 0.03 Hz, which correspond to minute bulk piezoelectric strengths of 1.47 fm/V and 83 am/V, respectively, indicating that there exists variation in anomalous piezoelectricity in separate samples. Comparing the results with the measurements from IDS-PFM, a well-established piezo measurement

technique with 55 fm/V sensitivity, that does not show any notable response, highlights the strength of our platform.

We then attempt to detect anomalous piezoelectricity in high-purity Si, which is of interest as it may inform us about possible limitations in qubit lifetimes due to anomalous piezoelectric coupling. From the measurement, we are able to provide an upper bound in piezoelectricity, corresponding to a bound in qubit lifetime of 4 ms. This is only an order of magnitude higher than the current state-of-the-art qubit [79], motivating us to further the bound by repeating piezoelectricity measurements on Si with the resonantly enhanced setup in the future.

The development of a novel material characterization tool such as our hybrid piezo-Brillouin opens the door to further evaluation of substrate purity and surface treatments, which is of critical importance in quantum technologies. The dual microwave/optical functionality may also be useful for investigating strain-active solid-state defects. Specifically, the resonant piezoelectric drive presents a mechanism for rapidly actuating strain fields, and the optical cavity offers the possibility of Purcell-enhanced photon collection.

Chapter 7

Microwave-to-optical transduction with a bulk acoustic resonator

7.1 Introduction

Recently with the advance of quantum information science, realizing efficient quantum state conversion is of critical importance for optically linking superconducting quantum devices, and remains an outstanding goal for the field. Electro-optomechanical devices have been widely studied in the context of microwave-to-optical quantum transduction. Various forms of mechanical systems, including membranes [15–17], OMCs [18–20], and thin film acoustic resonators [21, 22] have been explored to realize a electro-optomechanical transducer. Notably, the highest transduction efficiency of 47% among all platforms of microwave-to-optical transduction is achieved in a mechanical membrane-based system. Separately in OMC-based systems, added noise of less than a quantum of photon has been realized.

However, these devices also come with certain limitations. These include the complexity of device fabrication, leading to low yield of devices and limited tunability of device parameters post-fabrication. Also, most of them are microscopic structures,

with high surface-to-volume ratios. This inevitably makes the device susceptible to heating and added thermal noise caused by even a moderate optical pump. Certain devices rely on the use of a superconductive microwave component, which can be challenging to control in the presence of optical power. Additionally, efficient coupling of a transduced optical signal into a fiber can be an issue in chip-based systems.

Several advantages of our piezo-Brillouin hybrid cavity platform make it an appealing candidate to explore as a microwave-to-optical transducer. Its modular design allows flexible integration of highly coherent and highly tunable cavities that can be separately characterized and tuned. Moreover, in an HBAR-based Brillouin system, we observe strong optomechanical interactions (characterized by cooperativity exceeding unity), even reaching strong coupling [55]. Along with competitive coupling efficiencies nearing unity and robust thermal properties, these features reveal the potential of this hybrid platform for microwave-optical transduction with quantum applications [6, 14, 26]. In this chapter, we present bidirectional conversion with transduction efficiency comparable to other developing piezo-optomechanical platforms [18–20, 22, 122–124], with feasible improvement paths towards unity transduction.

7.2 Figures of merit

The figures of merit for efficient microwave-to-optical transduction in an electro-optomechanical platform are determined by the expression derived back in chapter 5 (equation 5.33),

$$\eta = \eta_{\text{opt}}\eta_{\mu}\frac{4C_{\text{em}}C_{\text{om}}}{(C_{\text{em}} + C_{\text{om}} + 1)^2}. \tag{7.1}$$

Here, we first see that a system needs to have efficient optical and microwave couplings, as $\eta \propto \eta_{\text{opt}}$ and $\eta \propto \eta_{\mu}$. Oftentimes, this can be a major bottleneck in achieving high transduction efficiency since efficiently interfacing a fiber with the

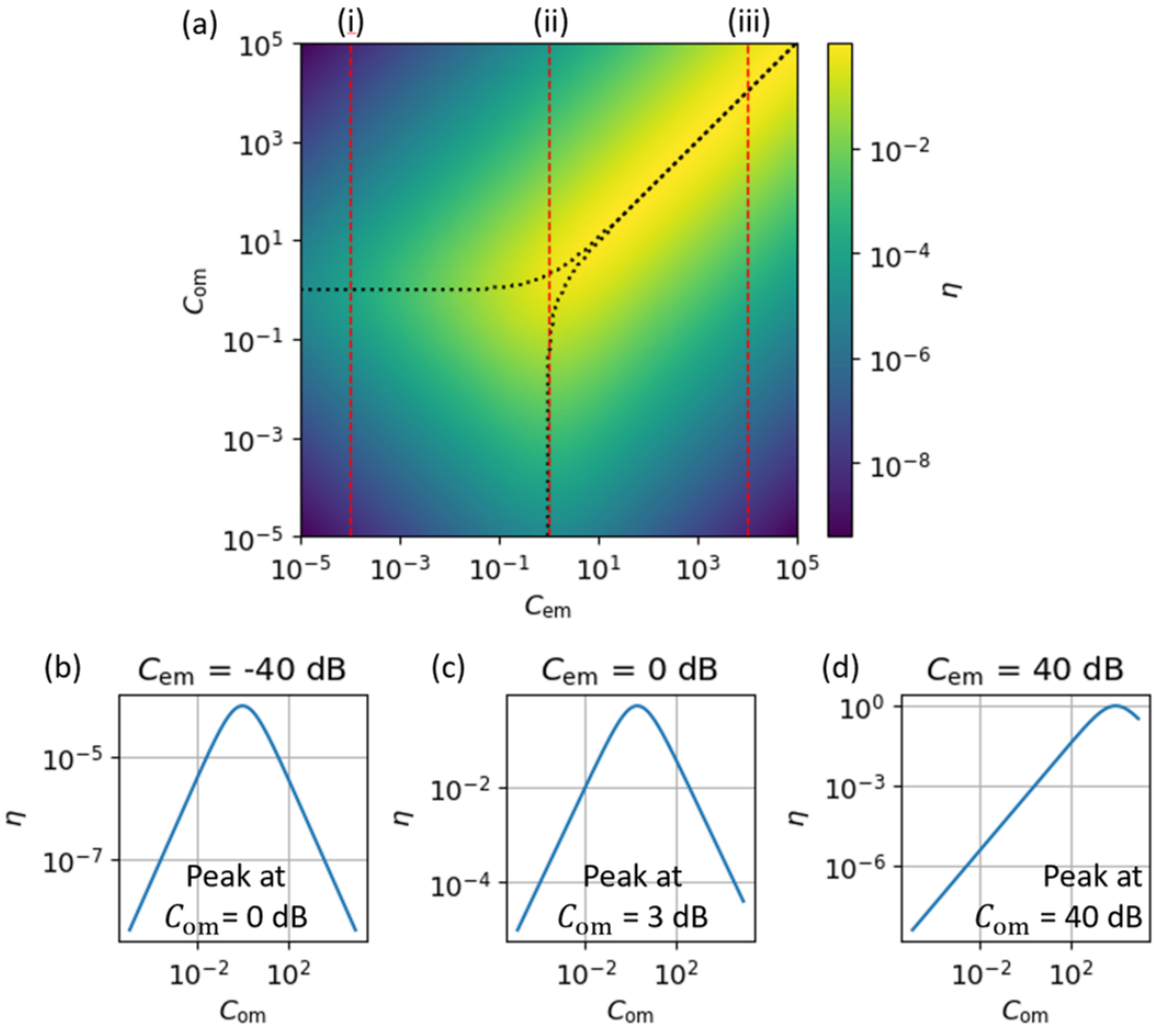

Figure 7.1: **Microwave-to-optical transduction efficiency across a range of electromechanical and optomechanical cooperativities** (a) A colorplot of microwave-to-optical transduction efficiency following equation 7.1 assuming $\eta_{\text{opt}} = 1$ and $\eta_\mu = 1$. The black dotted line marks the position of the peak transduction efficiency along both the C_{em} and C_{om} axes. Linecuts along red dashed lines are indicated as i, ii, and iii are shown in (b), (c), and (d), respectively. (b) Linecut along C_{em} = -40 dB. We observe peak transduction at $C_{\text{om}} = 0$ dB and reduced transduction when $C_{\text{om}} > 0$ dB. (c) Linecut along $C_{\text{em}} = 0$ dB. We observe peak transduction at $C_{\text{om}} =$ 3 dB. (d) Linecut along $C_{\text{em}} = 40$ dB. We observe peak transduction at $C_{\text{om}} = 40$ dB. Note that the transduction efficiency peaks as $C_{\text{om}} = C_{\text{em}}$ and decreases afterwards.

transducer can be challenging. In our platform, we have already achieved $\eta_{\mathrm{opt}}, \eta_{\mu} \sim 0.5$ in devices presented in chapter 6. In fact, we can readily reach optical and microwave coupling efficiencies above 0.5 by using an asymmetric optical cavity and by over-coupling to the microwave cavity.

The electromechanical and optomechanical cooperativities should be considered in three separate regimes. In the ideal regime, where both $C_{\mathrm{em}} \gg 1$ and $C_{\mathrm{om}} \gg 1$, we desire C_{em} and C_{om} to be as high as possible and to be equal to each other (see figure 7.1d). Similarly, in the regime where both $C_{\mathrm{em}} \ll 1$ and $C_{\mathrm{om}} \ll 1$, we want C_{em} and C_{om} to be their maximum possible values. Lastly when $C_{\mathrm{em}} \ll 1$ and $C_{\mathrm{om}} \sim 1$ ($C_{\mathrm{em}} \sim 1$ and $C_{\mathrm{om}} \ll 1$), we need C_{em} (C_{om}) to be maximal and C_{om} (C_{om}) to be equal to 1 (see figure 7.1b).

7.3 Experimental data

7.3.1 Cavity characterization

To demonstrate microwave-to-optical transduction using a hybrid electro-optomechanical setup through piezo-Brillouin interaction, we first need to characterize its components. The hybrid cavity design is illustrated in figure 5.1d, where we use a coaxial microwave cavity, flat-flat x-cut quartz HBAR, and an optical Fabry-Pérot cavity, while the measurement scheme is described in figure 5.7.

The coaxial microwave cavity is made out of OFHC copper, where the central pin is adjustable for wide-range frequency tuning. Its S_{11} reflection spectrum at cryogenic temperature (9 K) is given in figure 7.2. The seam loss between the copper body and the brass center pin results in a rather modest microwave Q-factor in this design. From data, we observe microwave coupling efficiency, $\eta_{\mu} = \kappa_{\mu,\mathrm{c}}/\kappa_{\mu}$, of 0.43. In the future, we eventually want to further over-couple to the microwave cavity to bring the microwave coupling efficiency even higher.

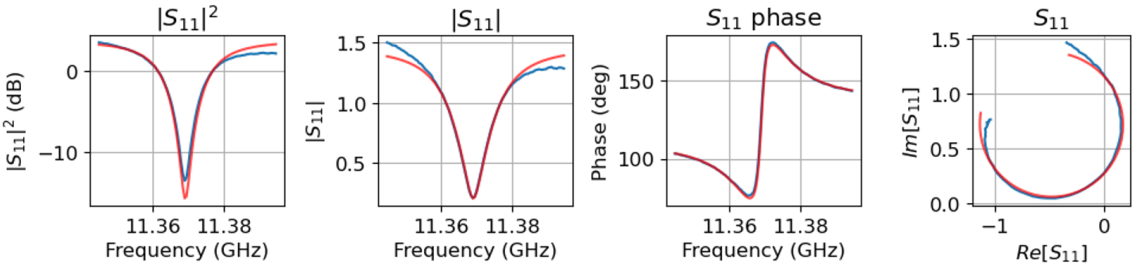

Figure 7.2: **Microwave cavity characterization for microwave-to-optical transduction with x-cut quartz** S_{11} spectrum of the microwave cavity (coaxial design) used for microwave-to-optical transduction with x-cut quartz at cryogenic temperature (9 K). Blue is the measured data and red is the fit based on equation 5.3. The fit values are: $\Omega_\mu/2\pi = 11.369$ GHz, $\kappa_\mu/2\pi = 17.1$ MHz, $Q_\mu = 662$, $\kappa_{\mu,\mathrm{c}}/2\pi = 7.33$ MHz, $Q_{\mu,\mathrm{c}} = 1550$, $\kappa_{\mu,\mathrm{i}}/2\pi = 9.79$ MHz, $Q_{\mu,\mathrm{i}} = 1160$.

For the acoustic cavity component, we use an HBAR with flat-flat geometry made out of x-cut quartz. Quartz is a well-understood material that we have previously used in section 6.2.1 and in other works [52–56]. It is important to note that people have reported a reduction of piezoelectric properties in x-cut quartz at cryogenic temperatures (5 K), thus here we follow the reduced piezoelectric constant of ~ 0.95 pm/V as reported in reference [117] and as measured in section 6.2.1, instead of the nominal value of 2.3 pm/V. Flat-flat geometry of an HBAR leads to a diffraction-limited acoustic lifetime in the order of ∼100 kHz. Although this is worse compared to our best plano-convex devices with $\Gamma < 1$ kHz (see chapter 4 and 6), such a wide linewidth has an advantage in terms of transduction bandwidth. Also, with a cavity-enhanced coupling rate, we expect our device to readily reach above optomechanical cooperativity of 1, even with the diffraction-limited acoustic linewidth.

The Fabry-Perot optical cavity used in our platform consists of two dielectric mirrors with 99.9% reflectivity and a dielectric substrate in the middle. Figures 7.3(b-c) show normalized reflection measurements for the two optical cavity modes used as pump and signal mode. We use optical sidebands to calibrate a linear frequency sweep over the modes, from which we can extract their linewidths. Measurements of the resonant transmission and reflection are used to extract the relative loss rates

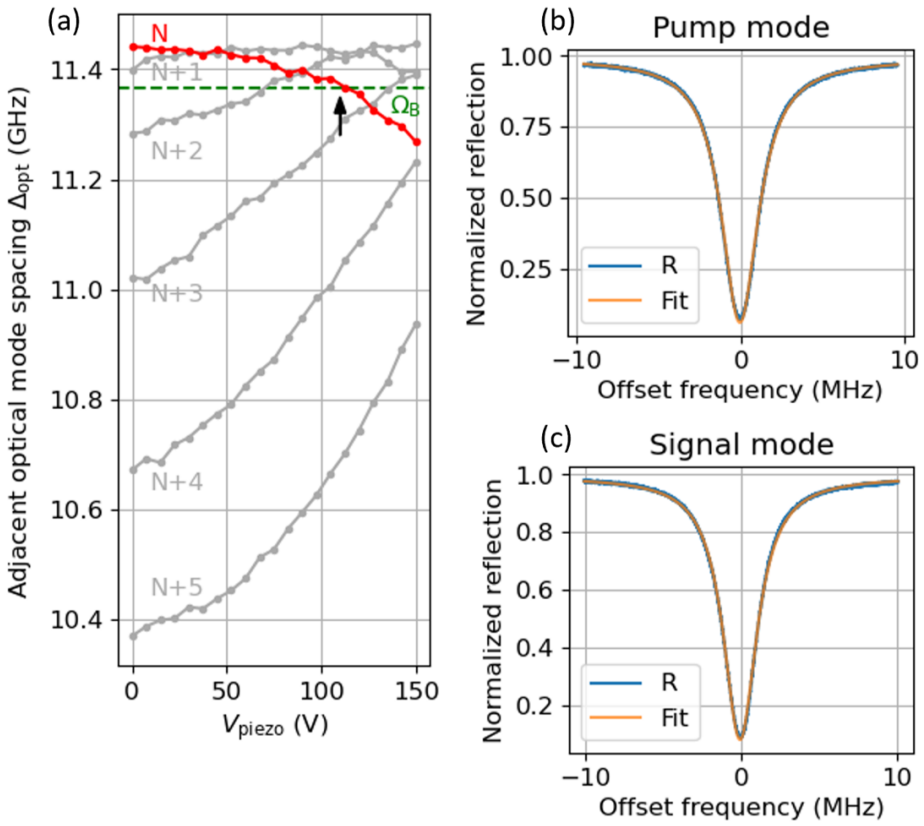

Figure 7.3: **Optical cavity characterization for microwave-to-optical transduction with x-cut quartz at 9 K temperature** (a) Optical mode spacing tunability. We find 6 mode pairs (labeled by lower longitudinal mode index N through N+5) for λ_{opt} between 1545.8-1546.3 nm, with spacings from 10.4 GHz to 11.5 GHz. V_{piezo} indicates the voltage applied to a piezo-actuator controlling the optical cavity length. By increasing V_{piezo} (thus changing cavity length), individual mode spacings can be varied by up to 500 MHz, allowing the mode pairs to match the Brillouin frequency, Ω_B (green dashed line). We choose to operate at N^{th} optical cavity mode pair, and at $V_{piezo} \sim 110$ V piezo-actuator setting, marked with a black arrow. (b-c) The normalized reflection spectrum of the optical cavity. Pump/signal modes for N^{th} optical cavity mode pair indicated with a black arrow in (a). Blue is the reflection data and orange is the fit. Fit values are: $\kappa_{opt}/2\pi = 2.2$ MHz, (coupling rate through the left port) $\kappa_{opt,cL}/2\pi = 0.7$ MHz, (coupling rate through the right port) $\kappa_{opt,cR}/2\pi = 1.2$ MHz, $\mathcal{F} = 5170$. Adapted from Ref. [57].

through each mirror, as well as the internal loss. Due to the dielectric interface within the cavity, it is possible to have asymmetric cavity loss rates through the two mirrors, even though they have nominally identical reflectivities. From the measurement, we can obtain the coupling efficiency, $\eta_{\mathrm{opt}} = \kappa_{\mathrm{opt,c}}/\kappa_{\mathrm{opt}}$, of 0.53. We consider coupling through the right port $\kappa_{\mathrm{opt,c}} = \kappa_{\mathrm{opt,cR}}$, as it is the port through which optical light exits.

The non-zero reflection of optical mode at the boundary of the dielectric media produces an intrinsic modulation of optical mode spacing. We use a broad, calibrated wavelength scan to identify the mode spacing. For the cavity geometry used here (11 mm vacuum, 0.5 mm quartz), we find modulation by $\pm$ 0.5 GHz around a mean mode spacing of 10.9 GHz. This variation allows us to find a mode spacing that approximately matches the Brillouin frequency. Here, we pump the lower-frequency mode, using the upper-frequency mode to resonantly match the anti-Stokes sideband. Since the mode spacing variation is larger than the optical cavity linewidth, the other (Stokes) process is strongly suppressed. *In situ* fine-tuning of optical cavity mode spacing at cryogenic temperatures is achieved through the use of a piezo-actuator that allows translation of one mirror position. With this, we can fine-tune the optical mode spacing to well match the acoustic mode frequency ($\Delta_{\mathrm{opt}} \approx \Omega_{\mathrm{m}}$). This optical frequency tuning range is shown in Figure 7.3(a), where we clearly see greater than 10% ($>$ 1 GHz) intrinsic variation, plus fine-tuning via the piezo-actuator voltage (0V $\sim$ 150V) to match the optical mode spacing with the acoustic mode (green dashed line).

7.3.2 Optomechanical response: OMIT

Matching of the optical mode spacing to the mechanical frequency enables strong optomechanical interactions. We lock a laser to the lower frequency (pump) mode and sweep a sideband over the higher frequency (signal) mode. When $\Delta_{\mathrm{opt}} \neq \Omega_{\mathrm{m}}$, this

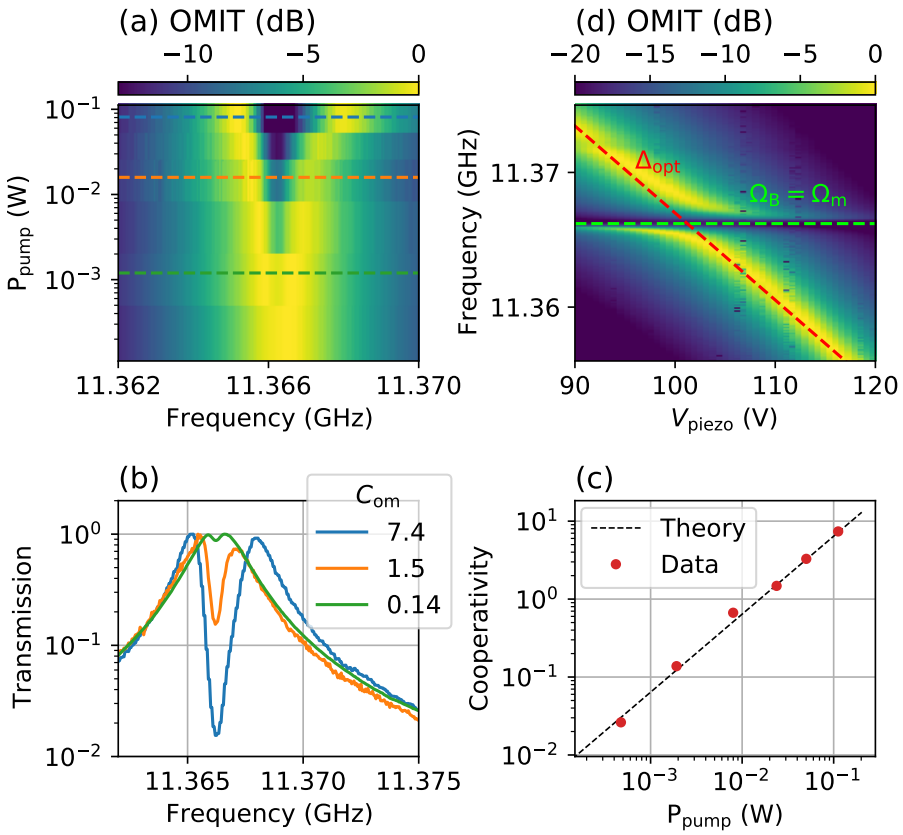

Figure 7.4: **OMIT spectrum of a hybrid cavity with x-cut quartz** (a) Normalized OMIT spectra with varying optical pump power. Clear splitting of the optomechanical response indicates strong coupling. Linecuts across blue, orange, and green dashed lines are shown in (b) in the same color. (b) OMIT spectra with fitted cooperativities ranging from $C_{\mathrm{om}} = 7.4 \sim 0.14$. (c) Cooperativity fitted from data in (a) versus optical pump power. Cooperativity from data (red) agrees well with the theoretical value (dotted black), indicating a linear relationship. (d) Normalized OMIT Spectra, as Δ_{opt} is tuned through Ω_{B}, using the piezo actuator. When $\Delta_{\mathrm{opt}} = \Omega_{\mathrm{B}}$, an anti-crossing is observed, with a splitting that exceeds the cavity linewidth, indicating the onset of strong coupling. Adapted from Ref. [57].

swept probe simply shows the optical response of the signal mode. Applying a voltage to the piezo actuator, we can smoothly vary the optical mode spacing from 11.355 GHz to 11.375 GHz (red dashed line in figure 7.4d), revealing an avoided crossing when $\Delta_{\mathrm{opt}} = \Omega_{\mathrm{m}}$. This is the result of an optical interference with a photoelastically-driven motional sideband [72], also known as OMIT. For more details on OMIT, refer back to section 2.4.1.

Measurements of OMIT in our device are shown in figure 7.4. From figure 7.4(a), we observe that this system approaches the optomechanical strong coupling regime ($2g_{\mathrm{om}} > \kappa_{\mathrm{opt}}, \Gamma$), visible as the emergence of normal-mode splitting [55]. Such strong coupling can be of value in hybrid quantum systems, for rapid manipulation of intra-cavity states. Fitting the spectrum across a range of pump powers to equation 2.34, we can directly extract optomechanical coupling rates and cooperativities of our device (figure 7.4b). The large visibility in OMIT dip here indicates high optomechanical cooperativity ($C_{\mathrm{om}} > 1$). The resulting cooperativities scale linearly with intra-cavity power, as expected from $C_{\mathrm{om}} \propto N_{\mathrm{p}} \propto P_{\mathrm{p}}$, reaching $C_{\mathrm{om}} = 7$ ($g_{\mathrm{om}} = 1.4$ MHz) at a pump power of 110 mW (figure 7.4c).

7.3.3 Bi-directional microwave-to-optical transduction

In characterizing our hybrid cavity as a piezo-Brillouin platform, we identify high coupling efficiencies of $\eta_{\mathrm{opt}}, \eta_{\mu} \sim 0.5$ and high optomechanical cooperativity of $C_{\mathrm{om}} > 1$. This already satisfies most of the requirements for efficient microwave-to-optical transduction from the expression of η given in equation 7.1. Hence, in this section we evaluate the performance of our piezo-Brillouin platform from the perspective of quantum transduction, quantifying the efficiency with which it converts microwave photons to optical photons.

In our hybrid cavity, we reach coupling efficiencies of $\eta_{\mu} = 0.43$ and $\eta_{\mathrm{opt}} = 0.53$. Higher coupling efficiencies (i.e. over-coupled resonators) are possible by adjusting the microwave coupling pin and using optical mirrors with imbalanced reflectivities. We note that the modes of Gaussian optical resonators easily achieve high fiber-coupling efficiency, which is a key challenge for low-loss integration.

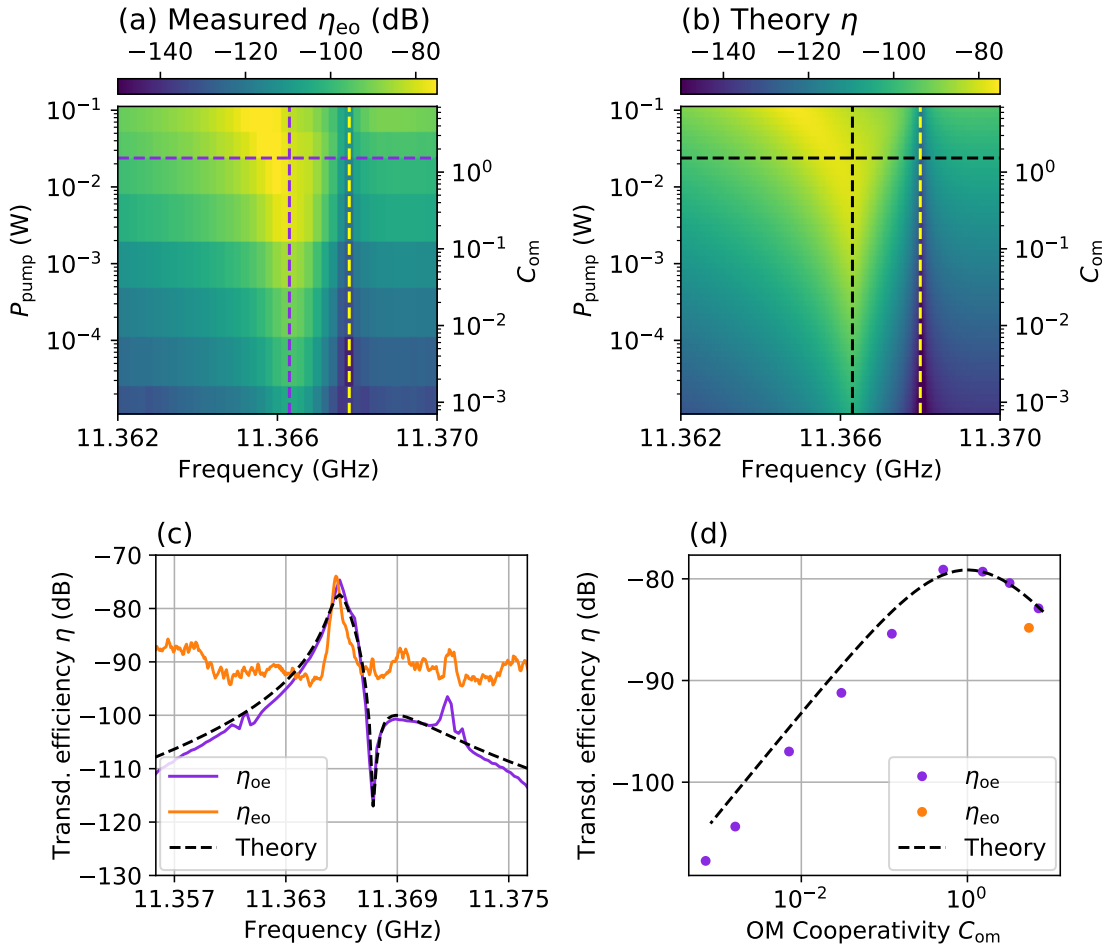

Figure 7.5: **Bi-directional microwave-to-optical transduction spectrum** (a) Measured microwave-to-optical conversion at varying pump power. Cooperativity on the right axis is calculated from the theory shown in figure 7.4(c). The shifting of the transduction peak to the left is clearly visible, indicating we are reaching $C_{om} > 1$. Electro-optic (EO) effect-induced dip on the right side of the transduction peak (indicated in yellow dashed line) is visible (further discussion in section 7.4). The dashed line in purple is the cross section along which data in (c-d) are plotted. (b) Expected transduction spectrum closely following the measurement. Colorscale is set to be identical to (a). The dashed line in black is the cross section along which black dashed lines in (c-d) are plotted. (c) Transduction spectra, for both microwave-to-optical (η_{oe}, purple, $C_{om} = 1.5$) and optical-to-microwave (η_{eo}, orange, $C_{om} = 5.5$). The dashed black line is a theoretical prediction of the transduction spectra. The elevated noise floor in the η_{eo} is set by the room temperature amplifiers/detectors. (b) Transduction efficiency at phonon frequency ($\Omega_m/2\pi = 11.3663$GHz) in relation to the optomechanical cooperativity controlled via optical pump power. Purple dots are microwave-to-optical data. The orange dot is an optical-to-microwave measurement. Both data are expected to follow the black dashed theory line. Adapted from Ref. [57].

Microwave-to-optical transduction

Microwave-to-optical conversion (η_{oe}) is measured by detecting the number of scattered optical photons exiting the Fabry-Perot cavity per microwave photon entering through the coupling pin. The measurement data is shown in figure 7.5(a) and (c) where we clearly see a peak in the response on the resonance ($\Omega_{\mathrm{m}}/2\pi = 11.366$ GHz). In fact, we even observe splitting of the peak at high pump powers, which indicates optomechanical mode splitting due to high cooperativities ($C_{\mathrm{om}} > 1$). Additionally, we observe a significant Fano dip near the transduction peak, indicated in the yellow dashed line in the figure. This is a result of a residual Pockels-type electro-optic (EO) coupling in quartz [125], which destructively interferes with the piezo-optomechanical signal. This Fano shape also results in a slightly higher response on the left side of the peak. The relative contribution of the EO effect to the piezo-Brillouin interaction can be reduced by increasing g_{em} or decreasing Γ. Alternatively, this effect could be intentionally amplified in a device focused on electro-optic interactions. Because of this EO effect, the state space model discussed in section 5.3.2 does not fully explain the spectrum in figure 7.5(a). Instead, we use a modified model incorporating the EO interaction (see section 7.4 for details) to fully explain our spectral response as illustrated in figure 7.5(b).

Figure 7.5(d) zooms into the response along the resonance, where we verify that the transduction efficiency scales as predicted with optical cooperativity. The experimental data (purple points) well-describe the theoretical curve (black dashed line) following Eq. 7.1, assuming $C_{\mathrm{em}} = 5.6 \times 10^{-8}$. In particular, we confirm that the transduction is maximized for $C_{\mathrm{om}} = 1$, implying that our optomechanical subsystem is sufficiently strongly coupled to saturate the transduction efficiency. Further increased C_{om} damps the acoustic resonance, reducing the overall efficiency. Note that the model is well-matched to the data for $g_{\mathrm{em}}/2\pi = 347$ Hz ($C_{\mathrm{em}} = 5.6\times10^{-8}$), instead of the simulated $g_{\mathrm{em}}/2\pi = 298$ Hz ($C_{\mathrm{em}} = 4.18 \times 10^{-8}$). This may be attributable to

a discrepancy between the HFSS-simulated microwave resonator and the assembled device.

The added noise floor of this transduction would be set by the thermal noise of the acoustic resonator, with an expected 16 phonons at 9K temperature. Characterization of the thermal noise in this quartz system was not carried out, but similar measurements on CaF_2 confirm good thermalization (see chapter 6), consistent with past works [55].

Thus, we can identify the current performance of this device achieving a maximum conversion of $\eta = 1.2^{+1.0}_{-0.6} \times 10^{-8}$, with a bandwidth of 500 kHz. The uncertainty here comes from detector and cable loss calibrations. With coupling efficiencies exceeding 10^{-1} and optomechanical cooperativity exceeding 1, the performance is currently limited by low electromechanical cooperativity ($C_{\text{em}} = 5.6 \times 10^{-8}$).

Optical-to-microwave transduction

Alternatively, we can repeat the measurement in the opposite direction to characterize the optical-to-microwave transduction (η_{eo}) through our system, where we count the number of microwave photons out per optical photon in. This detection is done by injecting an optical sideband into the optical cavity signal mode without any microwave drive, and directly measuring the microwave output through the coupling pin. The resulting spectral response is shown in figure 7.5(c). One aspect of η_{eo} that immediately stands out is its high noise floor. This noise floor is a combination of the Johnson noise of the room-temperature microwave detector, microwave amplifier noise, and detector noise. Since microwave photons have lower energy than optical photons, these noises are relatively higher when detecting a microwave response compared to detecting an optical response.

Even with limited SNR, demonstration of optical-to-microwave transduction response that well matches with theory shows the bi-directionality of our piezo-Brillouin

device as a transducer between microwave and optical domain. For detailed parameter values for the measurements done in this section, see appendix A.

7.3.4 Resonant enhancement of electro-optomechanical signal

Microwave-to-optical transduction with our hybrid cavity can be done in both resonant configuration and single-pass configuration. However, we choose to focus on the fully resonant operation that includes an optical cavity, rather than the single-pass operation lacking the optical cavity component. This is because we can expect a significant enhancement of response, following the work done in section 5.3.1. Specifically, the enhancement we expect from the fully resonant operation is given in equation 5.16, as $\frac{16}{\pi^2}\eta_{\mathrm{opt}}^2\mathcal{F}^2$. In this section, we explicitly show this improvement with our transduction experimental setup, by comparing the responses in the presence and in the absence of an optical cavity, while everything else is kept more or less unchanged.

To begin, we measure a wide piezo-Brillouin spectrum spanning across multiple acoustic FSRs with an x-cut quartz substrate, identical to the response in section 7.3.3 (purple data in figure 7.6). Then we remove the optical cavity in the apparatus while trying to keep everything else the same and measure the single-pass response (green data in figure 7.6). In both cases, we do direct measurements (figure 5.6) where phonon-scattered sideband power at the swept microwave drive frequency is measured via heterodyne with the optical pump in 1 kHz resolution bandwidth. Here, we focus on the central, phased-matched peak ($\Omega_{\mathrm{m}}/2\pi = 11.366$ GHz), corresponding to the m^{th} longitudinal acoustic mode. Comparing the experimental peak responses, we observe ~ 57 dB improvement from the single-pass signal to the cavity-enhanced signal, proportional to the optical cavity finesse squared as expected. The deviation of the enhancement factor from the expression in equation 5.16 comes from variations in experimental conditions including optical powers, microwave powers, and microwave

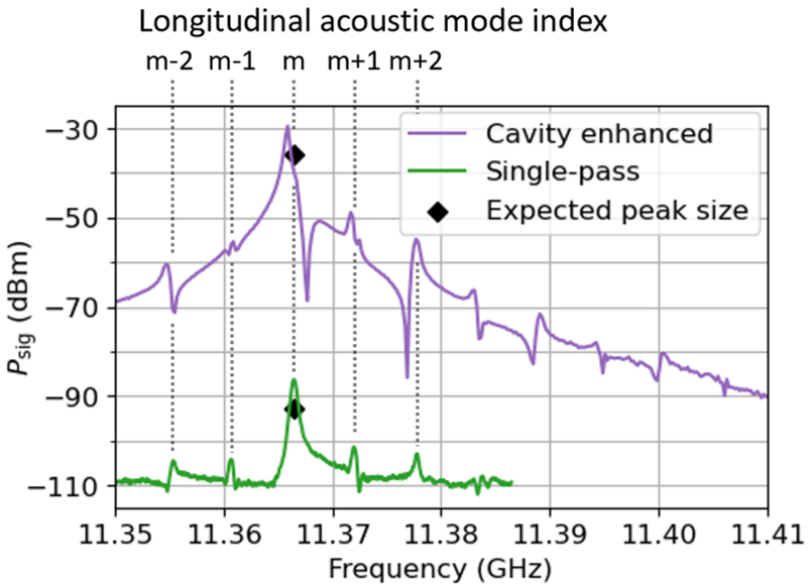

Figure 7.6: **Single-pass and cavity-enhanced piezo-Brillouin spectroscopy** Here, we demonstrate the resonant enhancement of the piezo-Brillouin signal in the presence of an optical cavity. The spectrum in purple is the data from the resonantly enhanced configuration of the hybrid cavity with an optical cavity of $\mathcal{F} \sim 5000$. It is identical to the response shown in figure 7.5(c). The spectrum in green is the data from the single-pass configuration of the hybrid cavity without an optical cavity. The main phonon mode of interest is labeled as the m^{th} longitudinal mode. Both measurements are done through direct measurement following figure 5.7. Predicted peak amplitudes calculated from theory (equation 5.10 5.15) and known material constants are shown as black dots To facilitate comparison more easily, the green data has been shifted down in frequency by 9 FSRs to compensate for a $\sim 0.5\%$ shift of microwave resonance frequency between cooldowns and between apparatus changes. Adapted from Ref. [57].

resonances. Note that one side of the Fabry-Pérot optical cavity lives inside the microwave cavity due to design constraints (see figure 5.1d). Thus, removing this dielectric mirror inside a microwave cavity results in having to re-adjust the microwave cavity, leading to imperfections in matching the initial conditions for the comparison experiments. Taking into account the variation in experimental conditions, we can theoretically predict the response amplitudes that well-match with the experiment and confirms the $\sim$ 57 dB signal enhancement, as shown in the black dots in the figure.

Observing the broad spectrum of x-cut quartz in the figure, there are several

prominent features worth pointing out, that are consistent with the underlying coupling mechanisms. On the tails of the central peak, we see the other longitudinal modes, whose motion coherently interferes to yield Fano lineshapes. The apparent coupling rates of these modes are suppressed according to the optical phase-matching condition ($\mathrm{sinc}^2\left[(\Omega-\Omega_\mathrm{B})/4\Delta_\mathrm{m}\right]$), as well as the piezoelectric mode-overlap (which suppresses coupling to even-index modes, i.e. m-1$^{\mathrm{th}}$, m+1$^{\mathrm{th}}$, ...). Away from the central mode, the piezo-Brillouin spectrum is further suppressed by the optical and microwave cavity susceptibilities. Also, each of the electro-optomechanical signal peaks is associated with a Fano lineshape. This is a result of interference with the EO effect in quartz, which we discuss further in the following section 7.4.

7.4 Modified theory accounting for electro-optic (EO) effect

In the state space model laid out in section 5.3.2, we only considered the electromechanical and optomechanical interactions in our platform. In reality, the crystal geometry of x-cut quartz leads to the emergence of Pockels EO effect, with a constant characterized as $r_{13} = 0.45$ pm/V [125].

The expression of EO coupling (Pockels effect) in materials is studied in various sources [126–129]. The single-photon EO coupling rate between an optical pump, optical signal, and microwave can be written as:

$$\begin{aligned}\hbar g_{\mathrm{eo},0} &= \epsilon_0 \int_{\mathrm{eo}} dV \epsilon_1 E_\mathrm{p} \epsilon_1 E_\mathrm{s} r_{13} E_\mu \\ &= \epsilon_0 \epsilon_1^2 r_{13} E_{\mathrm{p},0} E_{\mathrm{s},0} E_{\mu,0} \int_{\mathrm{eo}} dV e^{-\frac{r^2}{r_{\mathrm{opt}}^2}} e^{-\frac{r^2}{r_{\mathrm{opt}}^2}} \sin(k_\mathrm{p} z) \sin(k_\mathrm{s} z),\end{aligned} \tag{7.2}$$

where r_{13} is the relevant linear electro-optic coefficient component. Electric fields of optical pump (E_p) and optical signal (E_s) have corresponding normalization factors of

$E_{\mathrm{p},0} = \sqrt{2\hbar\omega_{\mathrm{p}}/\epsilon_0\epsilon_1 A_{\mathrm{opt}} L_{\mathrm{opt}}}$ and $E_{\mathrm{s},0} = \sqrt{2\hbar\omega_{\mathrm{s}}/\epsilon_0\epsilon_1 A_{\mathrm{opt}} L_{\mathrm{opt}}}$. While microwave ($E_\mu$) electric field has a zero-point field ($E_{\mu,0}$) obtained through HFSS, uniform along the interaction region. Assuming identical optical pump and signal mode profiles in both transverse and longitudinal directions, the above expression simplifies into,

$$g_{\mathrm{eo},0} = \frac{1}{4}\epsilon_1 r_{13} E_{\mathrm{sim}} \omega_{\mathrm{p}} \frac{L_{\mathrm{m}}}{L_{\mathrm{opt}}}. \tag{7.3}$$

EO coefficient in quartz is $r_{13} = 0.45$ pm/V from crystal symmetry [125]. The resulting single photon EO coupling rate in quartz is $g_{\mathrm{eo},0}/2\pi = 1.05$ mHz. Inside an optical cavity, this coupling rate is parametrically enhanced by the intercavity photon number ($g_{\mathrm{eo}} = \sqrt{N_{\mathrm{p}}} g_{\mathrm{eo},0}$), reaching $g_{\mathrm{eo}}/2\pi = 137$ Hz.

Incorporating this EO coupling rate into the state space model, we now have a full theoretical model to predict our transduction spectrum. The effective Hamiltonian describing the system, initially given in equation 5.20, now includes the EO coupling as,

$$H_{\mathrm{eff}}/\hbar = \Delta_{\mathrm{opt}} a^\dagger a + \Omega_{\mathrm{m}} b^\dagger b + \Omega_\mu c^\dagger c + (g_{\mathrm{om}} a^\dagger b + g_{\mathrm{em}} b^\dagger c + g_{\mathrm{eo}} a^\dagger c + \mathrm{H.c.}). \tag{7.4}$$

subsequently, we make the following adjustments to the A matrix, originally given in equation 5.26,

$$A = \begin{pmatrix} -i\Delta_{\mathrm{opt}} - \frac{\kappa_{\mathrm{opt}}}{2} & ig_{\mathrm{eo}} & ig_{\mathrm{om}} \\ ig_{\mathrm{eo}} & -i\Omega_\mu - \frac{\kappa_\mu}{2} & ig_{\mathrm{em}} \\ ig_{\mathrm{om}} & ig_{\mathrm{em}} & -i\Omega_{\mathrm{m}} - \frac{\kappa_{\mathrm{m}}}{2} \end{pmatrix} \tag{7.5}$$

Based on the changes made, we solve for the transduction expression in equation 5.30 ($\eta(\omega) = |S_{\mathrm{oe}}(\omega)|^2 = |S_{\mathrm{eo}}(\omega)|^2$), which gives the final expression of,

$$\eta = \eta_{\mathrm{opt}}\eta_\mu \frac{4(C_{\mathrm{em}}C_{\mathrm{om}} + C_{\mathrm{eo}}^2)}{4C_{\mathrm{em}}C_{\mathrm{om}}C_{\mathrm{eo}} + (C_{\mathrm{em}} + C_{\mathrm{om}} + C_{\mathrm{eo}} + 1)^2}, \tag{7.6}$$

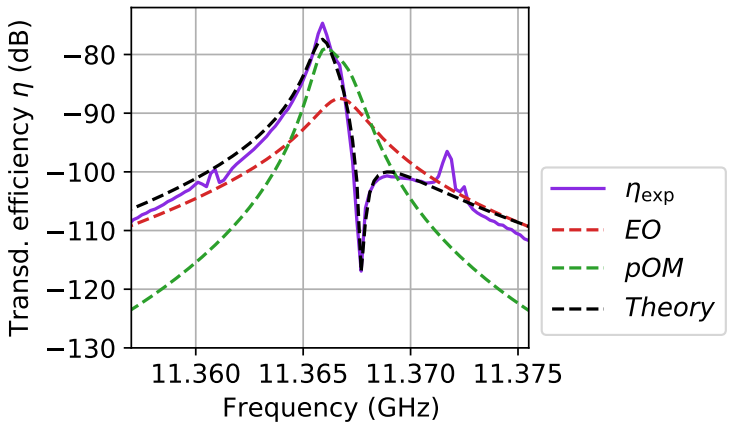

Figure 7.7: **Theoretical model predicting the transduction spectrum** The transduction spectrum from the experiment is shown in purple (identical to figure 7.5c). Using a modified state space model accounting for both the piezo-optomechanical (pOM) effect (shown in green dashed line) and the electro-optic (EO) effect (shown in dashed red line), we can correctly fit the transduction spectrum (shown in dashed black line), which includes the Fano feature resulting from the interference between the effects. Fitted values of the coupling rates are $g_{em}/2\pi = 347$ Hz (theory value 298 Hz) and $g_{eo}/2\pi = 162$ Hz (theory value 137 Hz). Adapted from Ref. [57].

as the microwave-to-optical transduction including electromechanical, optomechanical, and electro-optic interactions. Note that if we assume no EO effect ($C_{eo} = 0$), the expression reduces to the original electro-optomechanical relation given in equation 5.33.

Using the modified state-space model, we can fit the transduction spectrum from the experiment to our model. In fact, we can even observe individual contributions from piezoelectric coupling and EO coupling to the net transduction. In Figure 7.7, transduction from piezoelectricity is in dashed green and that from EO is in dashed red. The combined net transduction in dashed black can be fitted to the experimental data in purple, showing good agreement. The optomechanical coupling rate used in the fit is obtained through OMIT measurement ($g_{om}/2\pi = 643$ kHz and $C_{om} = 1.48$ at $P_p = 23.8$ mW). The fitted parameters are $g_{em}/2\pi = 347$ Hz (theory value is 298 Hz) and $g_{eo}/2\pi = 162$ Hz (theory value is 137 Hz). Such difference can be attributed

to a discrepancy between the simulated microwave cavity and the assembled device, and to the variation in material parameters at cryogenic temperatures.

The apparent interference between piezoelectric and EO effects near the center peak is because of similar EM and EO cooperativities. In the relatively lossy acoustic cavity regime that we are operating, we can still reach $C_{\mathrm{om}} > 1$. However, we have relatively low $C_{\mathrm{em}} = 5.6 \times 10^{-8}$, which is greater than $C_{\mathrm{eo}} = 2.8 \times 10^{-9}$ only by an order of magnitude. This is also observed in Figure 7.7, where the peak of theoretical EO transduction and that of theoretical piezo-optomechanical (pOM) transduction are separated only by ~ 10 dB. As a result, we observe a Fano interference in the transduction spectrum where the pOM response crosses through the EO response. This destructive interference is visible only on one side due to the phase relation between the pOM and EO interactions - constructive interference occurs on the other side.

One of the future paths to improve transduction, which is further discussed in section 7.5, is using an acoustic cavity with a better Q-factor. Integration of a high-Q HBAR will bring about a significant increase in C_{em}, while keeping C_{eo} constant, thus suppressing the formation of such Fano-like feature in future implementations of this design.

7.5 Outlook: Towards unity conversion efficiency

Recalling the expression for transduction efficiency in equation 7.1, efficient transduction requires maximixing the values for η_{opt}, η_{μ}, C_{om}, and C_{em}. In our system, we can readily reach C_{om} of 1 and η_{opt} (η_{μ}) of 0.53 (0.43). Although these are already relatively high values compared to other transducer devices, we can reach unity coupling efficiencies with ease by adjusting the microwave coupling pin to be over-coupled to the microwave cavity, and by having asymmetric optical cavity mirrors (i.e. creating

Suggested improvements	$g_{\mathrm{em}}/2\pi$	C_{em}	$\eta_{\mathrm{opt}}(\eta_\mu)$	η
Current experiment	347 Hz	5.6×10^{-8}	0.53 (0.43)	1.2×10^{-8}
Optimized coupling efficiencies	-	-	$\sim$1 ($\sim$1)	$\uparrow 4\times$
X-cut quartz $\rightarrow$ Z-cut LiNbO3	$\uparrow 7.3\times$	$\uparrow 50\times$	-	$\uparrow 50\times$
Optimized acoustic mode geometry	$\uparrow 9\times$	$\uparrow 80\times$	-	$\uparrow 80\times$
Re-entrant cavity	$\uparrow 3\times$	$\uparrow 10\times$	-	$\uparrow 10\times$
Superconducting cavity	-	$\uparrow 10^2\times$	-	$\uparrow 10^2\times$
Plano-convex hBAR	-	$\uparrow 10^3\times$	-	$\uparrow 10^3\times$
Total improve factors	$\uparrow\sim 200\times$	$\uparrow\sim 4 \cdot 10^9\times$	$\uparrow 2\times$ ($\uparrow 2\times$)	$\uparrow\sim 10^8\times$*
Total improve values	$\sim$68 kHz	$\sim$224	$\sim$1 ($\sim$1)	$\sim$0.9*

Table 7.1: **Electromechanical cooperativity improvements** * are calculated assuming $C_{\mathrm{om}} = C_{\mathrm{em}} = 10$ is reached. Adapted from Ref. [57].

a single-sided cavity). Also, note that the Gaussian optical cavity mode is well-suited for achieving high fiber-coupling efficiency, a key challenge for low loss integration of a transducer. Results from transduced signals in section 7.3.3 point at a low electromechanical cooperativity of $C_{\mathrm{em}} = 5.6 \times 10^{-8}$. In the limit of $\eta_{\mathrm{opt}} \approx \eta_\mu \approx 1$, $C_{\mathrm{om}} = 1$, and $C_{\mathrm{em}} \ll 1$, expression for transduction simplifies into,

$$\begin{aligned} \eta &\approx C_{\mathrm{em}} \\ &= \frac{4g_{\mathrm{em}}^2}{\kappa_\mu \Gamma}. \end{aligned} \tag{7.7}$$

Thus, improving the transduction efficiency boils down to improving C_{em} up to and above unity.

Among the approaches that we can take to enhance C_{em}, one obvious choice is to achieve stronger g_{em} as it is quadratically related to C_{em} ($C_{\mathrm{em}} \propto g_{\mathrm{em}}^2$). As laid out in table 7.1, one way we can improve g_{em} is through choosing a stronger piezoelectric material ($g_{\mathrm{em}} \propto d_{33}$), such as $LiNbO_3$ or $BaTiO_3$, instead of quartz. In the case of Z-cut $LiNbO_3$, piezoelectric tensor component increases from $d_{33} = 2.3$ pm/V of x-cut quartz to $d_{33} = 16.2$ pm/V of Z-cut $LiNbO_3$, and stiffness tensor component from

c_{33} = 86.6 GPa to c_{33} = 244 GPa. Even taking into account the impact from the change in density (ρ = 2650 kg/m^3 to ρ = 4630 kg/m^3), Brillouin frequency (Ω_m = 11.4 GHz to Ω_m = 21.0 GHz), and E_0 ($\frac{0.80}{\sqrt{2}} \times 10^{-3}$ V/m to $\frac{0.53}{\sqrt{2}} \times 10^{-3}$ V/m) due to higher relative permittivity, we can expect a higher g_em (C_em) by 7.3× (50×). Moreover, we can use a piezoelectric stack, consisting of alternating piezoelectric and non-piezoelectric layers with half acoustic wavelength thick, in order to maximize piezoelectric coupling to the acoustic substrate.

Another factor that influences g_em is the acoustic mode geometry. Referring back to equation 3.6, increasing the acoustic mode waist allows us to achieve better mode matching between acoustic and microwave modes, while thinner substrate thickness allows for lower mass acoustic mode (with larger zero-point motion) while maintaining same acoustic-microwave mode overlap. Reasonable modifications can be made to the acoustic waist from 50 um to 200 um and to the substrate thickness (L_m) from 500 um to 100 um. This result in a higher g_em (C_em) by 9× (80×). Note that reducing the substrate thickness will decrease the g_om, however, it will not deter our ability to exceed unity optomechanical cooperativity ($C_\mathrm{om} > 1$) as the current setup reaches $C_\mathrm{om} \sim 10$ with relative ease.

Similarly, we can also improve the microwave and acoustic mode-matching by making modifications to the microwave cavity. In doing so, we will be optimizing E_0, the remaining term in g_em. In order to reduce the microwave mode volume and concentrate the electric field, we can explore using a smaller coaxial microwave cavity or different cavity geometries such as a re-entrant cavity and other 2-D designs. Simulating a re-entrant cavity, we obtain approximately 3× stronger electric field compared to the coaxial design ($\frac{0.53}{\sqrt{2}} \times 10^{-3}$ V/m $\rightarrow \frac{1.8}{\sqrt{2}} \times 10^{-3}$ V/m), resulting in a higher g_em (C_em) by 3× (10×).

Besides optimizing g_em, we can also improve on other factors in C_em; namely, κ_μ and Γ. This demonstration uses a non-superconducting cooper microwave cavity, with

a modest Q $\sim 10^3$. With superconducting materials, both post and re-entrant cavities can readily reach Q $> 10^8$. Hence, in an ideal circumstance, κ_μ can be boosted by $> 10^5\times$. While co-integrating superconducting resonators with optics is a known technical challenge [20], this macroscopic, 3D platform may offer increased robustness of the superconducting resonator [130]. In appendix C, we discuss the measurements of $Q_{\mu,\mathrm{i}}$ of a superconducting niobium cavity at ~ 7 K, when optical light with greater than 100 mW of power is shined upon. From this measurement, we discover that the superconducting niobium cavity can still maintain $Q_{\mu,\mathrm{i}} \approx 10^6$ at 7 K ($\sim 10^3$ improvement from the copper microwave cavities used for transduction demonstration), even under 100 mW of optical light, which is higher than the required optical pump power to reach C_{om} of 1. Note that the measurement with superconducting niobium cavity is done at 7K, meaning that the microwave performance can be much better at lower (< 1 K) temperatures. In the table of improvements (table 7.1), we consider a conservative enhancement in κ_μ by $> 10^2\times$.

Diffractive loss in the acoustic cavity can be mitigated via shaping a concave surface on one side of the cavity through reactive-ion-etching. Doing so will allow the acoustic cavity to form stable resonances with Q up to $\sim 2.8 \times 10^7$ [53] from the current 2.3×10^4, allowing us a $\times 10^3$ improvement in Γ at a cost in transduction bandwidth. Implementation of an acoustic resonator with better Q also allows us to reach $C_{\mathrm{om}} > 1$ with weaker pump power (e.g. with $Q_{\mathrm{m}} = 10^7$, $C_{\mathrm{om}} = 1$ only requires $P_{\mathrm{p}} \approx 1\mu$W), increasing compatibility with mK cryogenic systems.

Together, these improvements highlight a feasible path from the $\eta = 1.2 \times 10^{-8}$ demonstrated here towards bidirectional transduction with near unity efficiency.

7.6 Conclusion

In conclusion, we put together resonant piezoelectric and Brillouin optomechanical interaction in an HBAR to create a platform for a bi-directional microwave-to-optical quantum transducer. Several advantages of our resonant piezo-Brillouin platform, including high coupling efficiencies ($\eta_{\text{opt}}, \eta_{\mu} \sim 0.5$), the ability to reach high optomechanical cooperativities ($C_{\text{om}} > 1$), modular design with wide frequency tunability, and robust thermal properties make it an appealing candidate to explore as a microwave-to-optical transducer.

We demonstrate a transduction efficiency of $\eta = 1.2^{+1.0}_{-0.6} \times 10^{-8}$, comparable to other developing piezo-optomechanical platforms [18–20, 22, 122–124], with a bandwidth of 500 kHz, and a bi-directional operation. We also present a model that accurately predicts the spectral response of transduction. Currently, the performance of our device is limited by low electromechanical cooperativity ($C_{\text{em}} = 5.6 \times 10^{-8}$). We provide multiple feasible paths to improve the electromechanical cooperativity, eventually leading toward unity conversion efficiency.

Within the landscape of transduction platforms, piezo-Brillouin systems presented in this chapter have a unique set of advantages and constraints and can be improved over many orders of magnitude. Combining all these highlights the potential of a hybrid piezo-Brillouin platform for microwave-optical transduction with quantum applications [6, 14, 26].

Chapter 8

Conclusion and outlook

In this dissertation, we present a novel strategy for realizing an electro-optomechanical platform, by harnessing Brillouin and piezoelectric interactions to simultaneously access phonons within bulk acoustic wave resonators. We explore the theoretical background and experimental implementations of the key ingredients of this design, that enable optimal simultaneous integration of both electromechanical and optomechanical interactions in a single platform. Furthermore, we demonstrate successful applications of this system as a precision material spectroscopy tool and a bi-directional microwave-to-optical quantum transducer.

Expanding on the prior works done [53], we design and fabricate HBARs that house Gaussian acoustic modes with long lifetimes at cryogenic temperatures ($<$ 10 K). In the process, we discuss observations on sample treatments and storage conditions that influence the sample performance. It is of interest to further the study of HBARs to areas of quantum information, where there are efforts to utilize them as quantum resources [7, 11] and to understand the dynamics of interactions between a qubit and an HBAR [33].

We exploit resonantly enhanced Brillouin optomechanical interaction between a Fabry-Pérot optical cavity and an HBAR, which allows optomechanical strong cou-

pling [55]. Comparing the optomechanical response of a non-resonantly enhanced signal to that of a resonantly enhanced signal, we analytically and experimentally achieve a significant improvement ($\propto \mathcal{F}^2$) that highlights the strength of such a system. Separately, an HBAR is interfaced with a highly tunable microwave cavity via piezoelectric interaction.

Combining Brillouin optomechanical interactions with piezoelectric electromechanical interactions mediated via an HBAR opens the door to a new type of an electro-optomechanical platform, which we call as a piezo-Brillouin platform. The complexity of integrating microwave/acoustic/optical components that other electro-optomechanical devices suffer from is overcome by a versatile modular design, allowing precise tuning and characterization of individual components required for a fully resonant operation. Along with high optomechanical cooperativity, competitive coupling efficiencies nearing unity, and robust thermal properties, these properties make our piezo-Brillouin system appealing for a range of applications.

Applying this work to areas of practical interest, we approach it from the perspective of a precision material spectroscopy technique. Its modular assembly allows efficient access to phonons within a variety of bulk crystalline materials. As a demonstration, we present measurements from piezoelectric x-cut quartz, non-piezoelectric CaF_2, and Si. In particular, with sub-quanta phonon sensitivities, we achieve piezo-detection sensitivity of 2.2 am/V (at 100 Hz bandwidth) in CaF_2 and reveal insight into possible anomalous piezoelectricity in CaF_2 of 83 am/V. From measurements on Si, we are able to provide a bound in anomalous piezoelectricity, which corresponds to a piezo-limited qubit lifetime of 4 ms based on a model we provide. This is only an order of magnitude higher than the current state-of-the-art qubit [79], motivating us to implement further improvements in the future to push this bound to a range that does not realistically impact qubit performances. Thus, the development of such a sensitive material characterization tool operating at GHz frequencies and at cryo-

genic temperatures is of importance in material studies that are critical to quantum technologies and beyond.

Finally, realizing efficient quantum state conversion is of critical importance for optically linking superconducting quantum devices, and remains an outstanding goal for the field. In this work, we describe the performance of our piezo-Brillouin platform as a microwave-to-optical transducer. Along with a theoretical model to predict the transduction spectrum, we present a transduction efficiency of $\eta = 1.2^{+1.0}_{-0.6} \times 10^{-8}$, comparable to other developing piezo-optomechanical platforms, with a bandwidth of 500 kHz, and a bi-directional operation. Although the current performance of the device is limited by low electromechanical cooperativity ($C_{\mathrm{em}} = 5.6 \times 10^{-8}$), we provide several feasible paths and our current efforts towards achieving unity transduction efficiency. Piezo-Brillouin system has a unique set of advantages and constraints and can be improved over many orders of magnitude, which highlights its potential for microwave-optical transduction with quantum applications and merits further investigation for quantum applications.

Appendix A

Experimental parameters

A.1 Parameters for x-cut quartz single-pass measurement (section 6.2.1)

Note that all crystal axis indices are assumed to be in the reference frame of the substrate, x-cut quartz.

Symbol	Meaning	Value	Units
S	Lock-in scale factor	100 (2000)	V/V_{rms}
G_{tz}	Photodetector trans-impedance gain	1000	Ω
R	Photodetector responsivity	1	A/W
ρ	Substrate density	2648	kg/m^3
n	Index of refraction	1.544	-
p_{13}	Photoelastic constant	0.29	-
c_{33}	Elastic stiffness tensor component	87	GPa
d_{33}	Piezoelectric constant (theory [117])	0.95	pm/V
$\omega_{opt}/2\pi$	Optical pump frequency	193535.55	GHz
P_p	Optical pump power	187 (180)	mW
P_s	Optical probe (Stokes) power	0 (77.8)	mW
P_{LO}	Optical LO power at photodetector	1.1 (0.558)	mW
η_{det}	Optical loss through apparatus	0.09 (0.0076)	-
$\Omega_m/2\pi$	Acoustic mode frequency	11.349	GHz
L_m	Acoustic substrate length	0.5	mm
A_m	Acoustic mode area	$\pi \times (50)^2$	μm^2
$\Gamma/2\pi$	Acoustic dissipation rate	1.3	kHz
$\Omega_\mu/2\pi$	Microwave cavity resonant frequency	11.35	GHz

$\kappa_{\mu,\mathrm{i}}/2\pi$	Microwave cavity internal loss rate	4.2	MHz
$\kappa_{\mu,\mathrm{c}}/2\pi$	Microwave cavity coupling rate	4.5	MHz
P_μ	Input microwave power at cavity	-27	dBm
E_0	Simulated electric field for single-photon excitation	5.5×10^{-3}	V/m
$g'_{\mathrm{om},0}/2\pi$	Single-photon optomechanical coupling rate (theory)	158	Hz
$g'_{\mathrm{om},0}/2\pi$	Single-photon optomechanical coupling rate (experiment)	130	Hz
G	Scattered signal (Stokes) power per pump power per phonon	6.54×10^{-18}	-
$g_{\mathrm{em}}/2\pi$	Electromechanical coupling rate (experiment)	2.85	kHz
d_{33}	Piezoelectric constant (experiment)	0.94	pm/V

Table A.1: **Experimental parameters single-pass measurements on x-cut quartz** Parameters for piezoelectrically driven phonons measurement in x-cut quartz are given, and in parenthesis are the parameters for optically driven phonons measurements (SBS).

A.2 Parameters for CaF_2 single-pass measurement (section 6.2.2)

Note that all crystal axis indices are assumed to be in the reference frame of the substrate, x-cut CaF_2.

Symbol	Meaning	Value	Units
S	Lock-in scale factor	10000 (1000)	$\mathrm{V/V_{rms}}$
G_{tz}	Photodetector trans-impedance gain	1000	Ω
R	Photodetector responsivity	1	A/W
ρ	Substrate density	3180	$\mathrm{kg/m^3}$
n	Index of refraction	1.426	-
p_{13}	Photoelastic constant	0.198	-
c_{33}	Elastic stiffness tensor component	165	GPa
d_{33}	Piezoelectric constant (theory)	0	pm/V
$\omega_{\mathrm{opt}}/2\pi$	Optical pump frequency	193535.55	GHz
P_{p}	Optical pump power	122.5 (116)	mW
P_{s}	Optical probe (Stokes) power	0 (50)	mW
P_{LO}	Optical LO power at photodetector	0.32 (0.664)	mW

η_{det}	Optical loss through apparatus	0.076 (0.013)	-
$\Omega_{\mathrm{m}}/2\pi$	Acoustic mode frequency	13.4574	GHz
L_{m}	Acoustic substrate length	3	mm
A_{m}	Acoustic mode area	$\pi \times (50)^2$	$\mu\mathrm{m}^2$
$\Gamma/2\pi$	Acoustic dissipation rate	1.7	kHz
$\Omega_{\mu}/2\pi$	Microwave cavity resonant frequency	13.455	GHz
$\kappa_{\mu,\mathrm{i}}/2\pi$	Microwave cavity internal loss rate	4.41	MHz
$\kappa_{\mu,\mathrm{c}}/2\pi$	Microwave cavity coupling rate	2.83	MHz
P_{μ}	Input microwave power at cavity	4	dBm
E_0	Simulated electric field for single-photon excitation	5.3×10^{-3}	V/m
$g'_{\mathrm{om},0}/2\pi$	Single-photon optomechanical coupling rate (theory)	29	Hz
$g'_{\mathrm{om},0}/2\pi$	Single-photon optomechanical coupling rate (experiment)	26	Hz
G	Scattered signal (Stokes) power per pump power per phonon	6.80×10^{-18}	-
$g_{\mathrm{em}}/2\pi$	Electromechanical coupling rate (experiment)	2.8	Hz
d_{33}	Bulk piezoelectric constant (experiment)	1.47	fm/V
d_{33}	Surface piezoelectric constant assuming 1 nm layer (experiment)	43	pm/V

Table A.2: **Experimental parameters single-pass measurements on CaF_2** Parameters for piezoelectrically driven phonons measurement in CaF_2 are given, and in parenthesis are the parameters for optically driven phonons measurements (SBS).

A.3 Parameters for Si single-pass measurement (section 6.2.3)

Note that all crystal axis indices are assumed to be in the reference frame of the substrate, x-cut Si.

Symbol	Meaning	Value	Units
S	Lock-in scale factor	50000 (10000)	$\mathrm{V/V_{rms}}$
G_{tz}	Photodetector trans-impedance gain	1000	Ω
R	Photodetector responsivity	1	A/W
ρ	Substrate density	2328	$\mathrm{kg/m^3}$
n	Index of refraction	3.45	-

p_{13}	Photoelastic constant	0.017	-
c_{33}	Elastic stiffness tensor component	165	GPa
d_{33}	Piezoelectric constant (theory)	0	pm/V
$\omega_{\mathrm{opt}}/2\pi$	Optical pump frequency	193535.55	GHz
P_{p}	Optical pump power	106.5 (98.4)	mW
P_{s}	Optical probe (Stokes) power	0 (20.5)	mW
P_{LO}	Optical LO power at photodetector	0.96 (0.8)	mW
η_{det}	Optical loss through apparatus	0.14 (0.049)	-
$\Omega_{\mathrm{m}}/2\pi$	Acoustic mode frequency	37.765	GHz
L_{m}	Acoustic substrate length	1	mm
A_{m}	Acoustic mode area	$\pi \times (50)^2$	$\mu\mathrm{m}^2$
$\Gamma/2\pi$	Acoustic dissipation rate	45	kHz
$\Omega_{\mu}/2\pi$	Microwave cavity resonant frequency	37.81	GHz
$\kappa_{\mu,\mathrm{i}}/2\pi$	Microwave cavity internal loss rate	144	MHz
$\kappa_{\mu,\mathrm{c}}/2\pi$	Microwave cavity coupling rate	70	MHz
P_{μ}	Input microwave power at cavity	9	dBm
E_0	Simulated electric field for single-photon excitation	7×10^{-3}	V/m
$g'_{\mathrm{om},0}/2\pi$	Single-photon optomechanical coupling rate (theory)	42.7	Hz
$g'_{\mathrm{om},0}/2\pi$	Single-photon optomechanical coupling rate (experiment)	37	Hz
G	Scattered signal (Stokes) power per pump power per phonon	9.54×10^{-18}	-
$g_{\mathrm{em}}/2\pi$	Upper bound in electromechanical coupling rate (experiment)	3.5	Hz
d_{33}	Upper bound in bulk piezoelectric constant (experiment)	1.2	fm/V
d_{33}	Upper bound in surface piezoelectric constant assuming 1 nm layer (experiment)	6	pm/V
T_1	Bound in piezo-limited qubit lifetime assuming bulk piezoelectricity	290	ms
T_1	Bound in piezo-limited qubit lifetime assuming surface piezoelectricity	4	ms

Table A.3: **Experimental parameters single-pass measurements on Si** Parameters for microwave-driven optical readout measurement in Si are given, and in parenthesis are the parameters for optically driven phonons measurements (SBS).

Symbol	Meaning	Value	Units
S	Lock-in scale factor	30000	$\mathrm{V/V_{rms}}$
G_{tz}	Photodetector trans-impedance gain	1000	Ω
R	Photodetector responsivity	1	A/W
ρ	Substrate density	2328	$\mathrm{kg/m^3}$
n	Index of refraction	3.45	-

p_{13}	Photoelastic constant	0.017	-
c_{33}	Elastic stiffness tensor component	165	GPa
d_{33}	AlN piezoelectric constant (theory)	5.1	pm/V
v_{AlN}	AlN acoustic velocity	10127	m/s
$\omega_{\mathrm{opt}}/2\pi$	Optical pump frequency	193535.55	GHz
P_{p}	Optical pump power	5.745	mW
P_{LO}	Optical LO power at photodetector	0.96	mW
η_{det}	Optical loss through apparatus	0.103	-
$\Omega_{\mathrm{m}}/2\pi$	Acoustic mode frequency	37.765	GHz
L_{m}	Acoustic substrate length	1	mm
A_{m}	Acoustic mode area	$\pi \times (50)^2$	$\mu\mathrm{m}^2$
$\Gamma/2\pi$	Acoustic dissipation rate	45	kHz
$\Omega_{\mu}/2\pi$	Microwave cavity resonant frequency	37.80	GHz
$\kappa_{\mu,\mathrm{i}}/2\pi$	Microwave cavity internal loss rate	89	MHz
$\kappa_{\mu,\mathrm{c}}/2\pi$	Microwave cavity coupling rate	105	MHz
P_{μ}	Input microwave power at cavity	9	dBm
E_0	Simulated electric field for single-photon excitation	7×10^{-3}	V/m
$g'_{\mathrm{om},0}/2\pi$	Single-photon optomechanical coupling rate	42.7	Hz
G	Scattered signal (Stokes) power per pump power per phonon	9.54×10^{-18}	-
$g_{\mathrm{em}}/2\pi$	Upper bound in electromechanical coupling rate (experiment)	2	kHz
d_{33}	Surface piezoelectric constant in 150 nm layer (experiment)	1	pm/V

Table A.4: **Experimental parameters for piezoelectrically driven phonons measurement on AlN on Si**

A.4 Parameters for CaF_2 resonantly enhanced measurement (section 6.2.4)

Note that all crystal axis indices are assumed to be in the reference frame of the substrate, x-cut CaF_2.

Symbol	Meaning	Value	Units
G_{tz}	Photodetector trans-impedance gain	500	Ω

R	Photodetector responsivity	0.88	A/W
ρ	Substrate density	3180	kg/m^3
n	Index of refraction	1.426	-
p_{13}	Photoelastic constant	0.198	-
c_{33}	Elastic stiffness tensor component	165	GPa
d_{33}	Piezoelectric constant (theory)	0	pm/V
$\omega_{\mathrm{opt}}/2\pi$	Optical pump frequency	192610	GHz
κ_{opt}	Optical cavity loss rate	2.1	MHz
$\kappa_{\mathrm{opt,cR}}$	Optical cavity coupling rate (right mirror, exiting port)	0.6	MHz
$\kappa_{\mathrm{opt,cL}}$	Optical cavity coupling rate (left mirror, entering port)	0.93	MHz
$\mathcal{F}$	Optical cavity finesse	3200	-
L_{opt}	Optical cavity length	22	mm
P_{p}	Optical pump power**	23 (30.1)	mW
P_{LO}	Optical LO power at photodetector	0.95	mW
η_{det}	Optical loss through apparatus	0.083	-
$\Omega_{\mathrm{m}}/2\pi$	Acoustic mode frequency	13.354	GHz
L_{m}	Acoustic substrate length	0.5	mm
A_{m}	Acoustic mode area	$\pi \times (64)^2$	μm^2
$\Gamma/2\pi$	Acoustic dissipation rate	400	kHz
$\Omega_{\mu}/2\pi$	Microwave cavity resonant frequency	13.367	GHz
$\kappa_{\mu,\mathrm{i}}/2\pi$	Microwave cavity internal loss rate	11.5	MHz
$\kappa_{\mu,\mathrm{c}}/2\pi$	Microwave cavity coupling rate	10.9	MHz
P_{μ}	Input microwave power at cavity	4.68 - 20	dBm
E_0	Simulated electric field for single-photon excitation	$\frac{5.1}{\sqrt{2}} \times 10^{-4}$	V/m
P_{cal}	Detector calibration term*	0.74	dB
η_{opt}	Optical coupling efficiency	0.29	-
η_{μ}	Microwave coupling efficiency	0.49	-
$g_{\mathrm{om}}/2\pi$	Optomechanical coupling rate (from OMIT)	385	kHz
C_{om}	Optomechanical cooperativity (from OMIT)**	0.705 (0.914)	-
$g_{\mathrm{em}}/2\pi$	Electromechanical coupling rate (experiment)	0.034	Hz
d_{33}	Bulk piezoelectric constant (experiment)	83	am/V
d_{33}	Surface piezoelectric constant assuming 1 nm layer (experiment)	2.44	pm/V

Table A.5: **Experimental parameters for piezoelectrically driven phonons measurement on CaF_2** *Detector calibration term includes the responses from a photodetector, spectrum analyzer, and microwave amplifier. **Values in parenthesis are the values for spontaneous measurement detecting thermal phonons.

A.5 Parameters for microwave-to-optical transduction with x-cut quartz (section 7.3.3)

Note that all crystal axis indices are assumed to be in the reference frame of the substrate, x-cut quartz.

Symbol	Meaning	Value	Units
G_{tz}	Photodetector trans-impedance gain	500	Ω
R	Photodetector responsivity	0.88	A/W
ρ	Substrate density	2648	kg/m^3
n	Index of refraction	1.544	-
p_{13}	Photoelastic constant	0.29	-
c_{33}	Elastic stiffness tensor component	87	GPa
d_{33}	Piezoelectric constant (theory [117])	0.95	pm/V
r_{13}	Electro-optic coefficient [125]	0.45	pm/V
$\omega_{\mathrm{opt}}/2\pi$	Optical pump frequency	194000	GHz
κ_{opt}	Optical cavity loss rate	2.2	MHz
$\kappa_{\mathrm{opt,cR}}$	Optical cavity coupling rate (right mirror, exiting port)	1.2	MHz
$\kappa_{\mathrm{opt,cL}}$	Optical cavity coupling rate (left mirror, entering port)	0.7	MHz
$\mathcal{F}$	Optical cavity finesse	5170	-
L_{opt}	Optical cavity length	11.8	mm
P_{p}	Optical pump power	0.47 - 112	mW
P_{LO}	Optical LO power at photodetector**	0.153	mW
η_{det}	Optical loss through apparatus**	0.01	-
$\Omega_{\mathrm{m}}/2\pi$	Acoustic mode frequency	11.366	GHz
L_{m}	Acoustic substrate length	0.5	mm
A_{m}	Acoustic mode area	$\pi \times (50)^2$	μm^2
$\Gamma/2\pi$	Acoustic dissipation rate	500	kHz
$\Omega_{\mu}/2\pi$	Microwave cavity resonant frequency	11.369	GHz
$\kappa_{\mu,\mathrm{i}}/2\pi$	Microwave cavity internal loss rate	9.79	MHz
$\kappa_{\mu,\mathrm{c}}/2\pi$	Microwave cavity coupling rate	7.33	MHz
P_{μ}	Input microwave power at cavity	0	dBm
E_0	Simulated electric field for single-photon excitation	$\frac{8}{\sqrt{2}} \times 10^{-4}$	V/m
P_{cal}	Detector calibration term*	12.75	dB
η_{opt}	Optical coupling efficiency	0.53	-
η_{μ}	Microwave coupling efficiency	0.43	-
$g_{\mathrm{om}}/2\pi$	Optomechanical coupling rate (from OMIT)	86 - 1400	kHz
C_{om}	Optomechanical cooperativity (from OMIT)	0.026 - 7.37	-
$g_{\mathrm{em}}/2\pi$	Electromechanical coupling rate (theory)	298	Hz

$g_{\mathrm{em}}/2\pi$	Electromechanical coupling rate (experiment)	347	Hz
C_{em}	Electromechanical cooperativity (theory)	4.18×10^{-8}	-
C_{em}	Electromechanical cooperativity (experiment)	5.6×10^{-8}	-
g_{eo}	Electro-optic coupling rate (theory)	137	Hz
g_{eo}	Electro-optic coupling rate (fitted)	162	Hz
C_{eo}	Electro-optic cooperativity (fitted)	2.8×10^{-9}	-
η	Transduction efficiency from experiment	$1.2^{+1.0}_{-0.6} \times 10^{-8}$	-

Table A.6: **Experimental parameters for microwave-to-optical transduction on x-cut quartz** *Detector calibration term includes the responses from a photodetector, spectrum analyzer, and microwave amplifier. **Note that the optical LO power and loss through apparatus vary depending on the optical pump power used. Here we provide the value for $P_{\mathrm{p}} = 23.8$ mW, presented in figure 7.5 (c).

Appendix B

Issues with clamping

Integration of a Fabry-Pérot optical cavity in our piezo-Brillouin platform is done only with a coaxial microwave cavity in this dissertation. This is because we experience issues with clamping acoustic substrates in other types of microwave cavities. As discussed in the main text, we experience a challenge in optimally matching the optical modes of a Fabry-Pérot cavity and the acoustic modes of an HBAR. As a result, we choose to work with flat-flat HBARs. The downsides of a flat-flat HBAR not only include diffraction-limited acoustic linewidth, but also the fragility of its stability, which improper clamping can easily disturb.

Acoustic responses of flat-flat HBARs when clamped inside different microwave cavity designs are shown in figure B.1. When a re-entrant cavity is used (figure B.1c), we clearly observe spurious phonon modes with varying and unpredictable quality, indicating the formation of unstable modes due to clamping. A COMSOL simulation with simplified clamping conditions at cryogenic temperature (10K) is shown in the inset of figure B.1(c). Even while assuming idealized clamping conditions, we observe that there are deformations and built-in stress within the substrate, which may lead to perturbations in phonon modes within the substrate. As a comparison, acoustic characterizations of a much more stable plano-convex HBAR inside the same

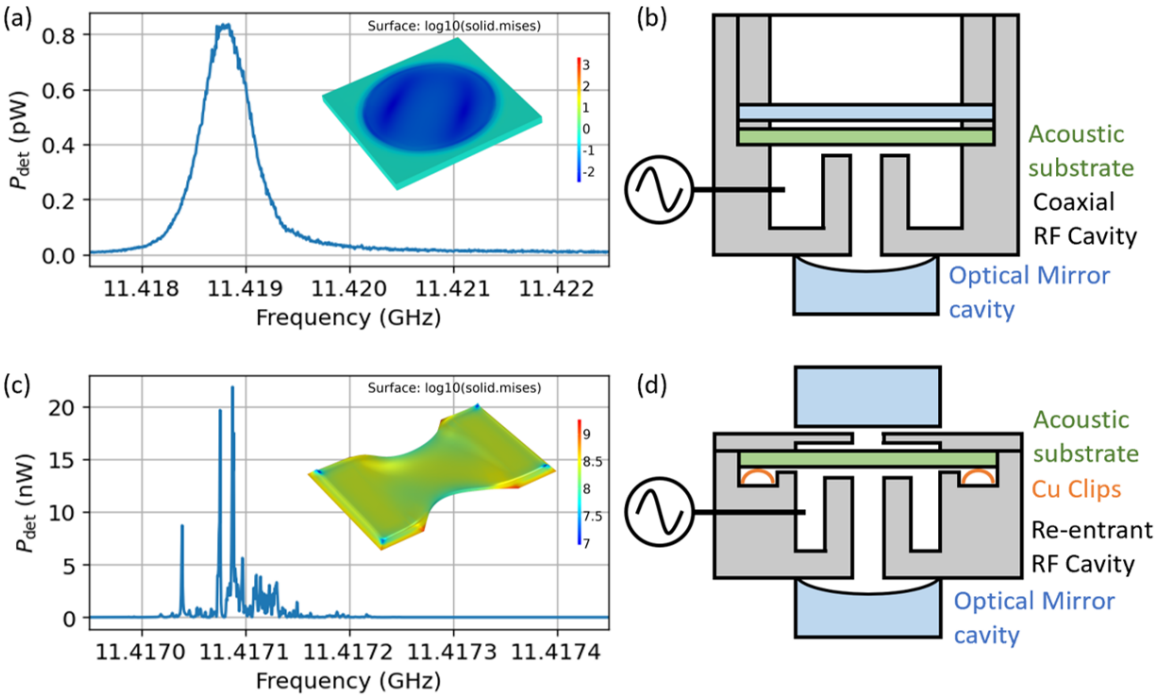

Figure B.1: **Acoustic responses from flat-flat HBARs clamped under different conditions** (a) Phonon signal peak of x-cut quartz flat-flat HBAR inside a coaxial microwave cavity. We do not observe any spurious peaks and the spectrum well matches our expectations. Inset shows a COMSOL simulation on an x-cut quartz substrate at cryogenic temperature (10K) with simplified clamping conditions to visualize the effects of clamping. The clamping pressure is normalized to 1N/m^2. The surface plot denotes the Von Mises stress in log10 unit. Deformation of the substrate is exaggerated by a factor of 200. (b) Sketch of a device with a coaxial microwave cavity integrated with a flat-flat HBAR and an optical Fabry-Pérot cavity. (c) Phonon signal peak of x-cut quartz flat-flat HBAR inside a re-entrant microwave cavity. Spurious peaks with narrow linewidths were observed, implying perturbations in phonon modes mode likely due to clamping. The spectrum here does not match our predictions. Inset shows a COMSOL simulation on an x-cut quartz substrate at cryogenic temperature (10K) with simplified clamping conditions to visualize the effects of clamping. The clamping pressure is normalized to 1N/m^2. The surface plot denotes the Von Mises stress in log10 unit. Deformation of the substrate is exaggerated by a factor of 200. (d) Sketch of a device with a re-entrant microwave cavity integrated with a flat-flat HBAR and an optical Fabry-Pérot cavity. Notice that the acoustic substrate has to be pushed to the lid with beryllium copper clips because we need the acoustic substrate to be as parallel as possible to the flat mirror on the other side of the lid for optimal optomechanical mode matching.

re-entrant cavity with identical clamping yielded predictable responses with narrow linewidths without spurious modes (figure 6.2 and 6.4).

Using a coaxial microwave cavity, we are able to come up with a design with an even and symmetrical clamping of the acoustic substrate (figure B.1a) We no longer see spurious, randomly spaced modes, the signal amplitude well matches to theory, and the linewidth matches closely to our diffraction-limited acoustic linewidth estimations.

Hence, although the type of usable microwave cavity is not technically restricted when using a highly stable, plano-convex HBAR, clamping properties of microwave cavities do limit us to using a coaxial microwave cavity design when integrating a not as stable, flat-flat HBAR.

Appendix C

Superconducting niobium cavity characterization under optical illumination

In this dissertation, all microwave cavities are made with OFHC copper. One way to improve the device performance, as suggested in section 7.5, is to use superconducting microwave cavities instead of copper cavities. Combining superconducting elements with optical elements, however, is a known challenge. When a superconducting material absorbs energy larger than the superconducting gap ($> 2\Delta_{\mathrm{SC}}$, where $\Delta_{\mathrm{SC}} \approx 1.764 k_{\mathrm{B}} T_{\mathrm{C}}$), Cooper pairs can be broken, generating quasiparticles [131]. This can lead to poor superconductor performance such as microwave decoherence. A list of superconducting energy gaps for a few example materials is given below in table C.1 Notice from table C.1 that the superconducting energy gaps are of much lower energy than optical photons, thus being a major hurdle in integrating a superconducting component with an optical component.

In order to check how our hybrid cavity devices will perform when using a superconducting microwave cavity, we did a simple experiment of illuminating a su-

Material	T_C (K)	Δ_{SC} (μeV)	$2\Delta_{SC}$ (GHz)
Al	1.11	168	80
Ta	4.4	667	300
Nb	9.2	1395	700
NbTiN	14.5	2200	1000

Table C.1: **Superconducting energy gaps of example superconducting materials**

perconducting microwave cavity with optical light (figure C.1a). Since our He-4 flow cryostat can cool down only to 4 K, we chose Nb, a material with relatively high T_C at 9.2 K, as the cavity material. At 6.5 K, which is the coldest temperature we could reach at the time of the experiment, we observe cavity internal Q-factor $> 10^6$. Note that this is not the peak Q-factor value for a Nb superconducting cavity since cavity internal-Q usually plateaus at $T = 0.1T_C$. In fact, there is a study showing superconducting Nb coaxial cavities with similar designs reaching internal Q-factors greater than 10^9 [132].

We track the Q-factor of the microwave cavity during cooldown (figure C.1b-c) to confirm that it has transitioned into a superconducting state. Once it reaches the coolest state allowed by the cryostat, we start illuminating 1550 nm wavelength laser at the tip of the coax, where we simulate the current flow density as the highest. The optical waist of the laser is approximately 70 μm. As light touches the microwave cavity, we observe a minor shift in Q-factor of $10 \sim 20\%$ (from 1.1×10^6 to 9×10^5) and a shift in cavity temperature of $20 \sim 200$ mK. Plotting the internal microwave Q in terms of the heated temperature of the cavity, we notice that the drift in Q matches the drift in temperature (figure C.1b-c), indicating that the shift in Q stems from cavity heating, while other effects, such as quasiparticle generation, are minimal. Although the data from laser illumination does closely follow the cooldown data, we observe that the illumination data is slightly lower in Q compared to the cooldown data. This is most likely because the temperature inside the cavity is slightly higher

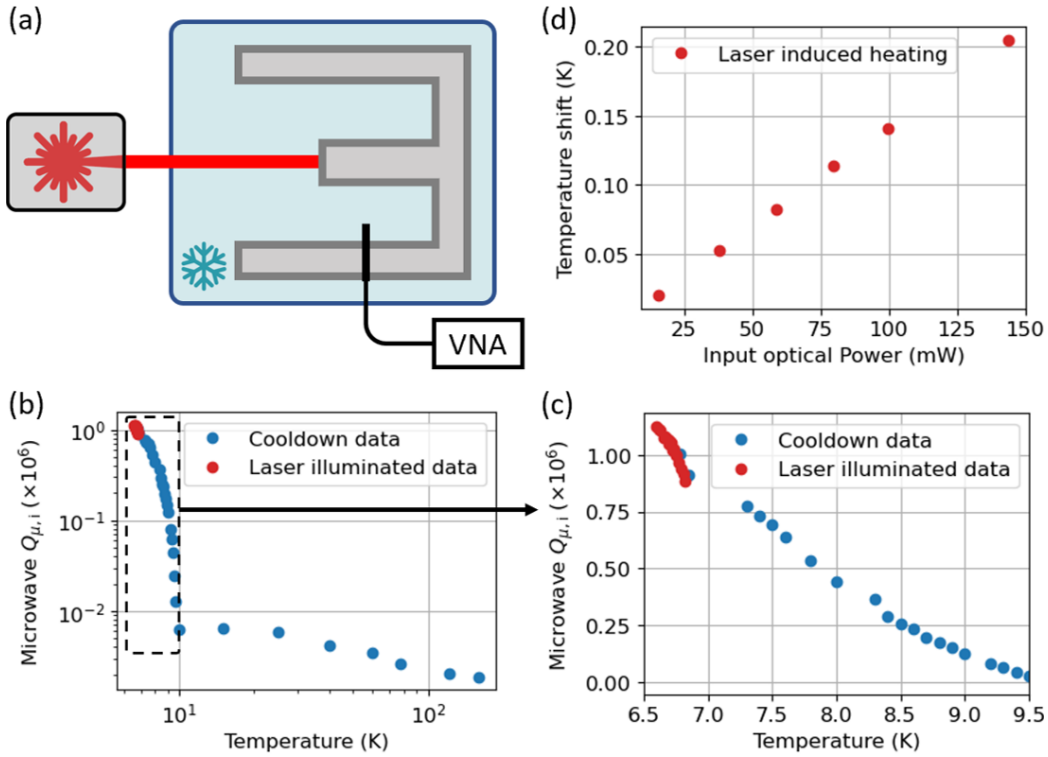

Figure C.1: **Laser illumination experiment on superconducting Nb cavity** (a) Measurement setup for observing the effects of laser illumination on superconducting Nb microwave cavity. A coaxial Nb microwave cavity is brought down below its critical temperature, then a laser with 1550 nm wavelength is illuminated at the tip of the coax. (b) Tracking internal microwave Q-factor as a function of temperature. Blue data is taken as the cavity is cooled down (no light illumination) and red data is the measurement when the laser is illuminated. (c) Zoom-in figure from temperature 6.5 K to 9.5 K, indicated in the dashed box in (b). (d) When 1550 nm laser is illuminated, we observe a shift in cavity temperature. The heating of cavity temperature as a function of input optical power is presented.

than the temperature read off from the sensor. The temperature sensor is installed on the outside wall of the microwave cavity, which is a few cm away from the light illumination spot. Along with the position of the temperature sensor, poor thermal conduction properties of a superconductor can lead to a higher local temperature at the light illumination spot compared to the temperature we read off from the sensor.

In this test, we shinned light up to 150 mW in power. Even then, we observe a minimal shift in microwave Q, still maintaining $Q_{\mu,\mathrm{i}} > 9 \times 10^5$. In the current piezo-Brillouin experiment, it requires $\sim$ 10 mW of optical pump light to reach $C_{\mathrm{om}} >$

1. From the test with a Nb cavity, this value corresponds to < 20 mK of heat-up, and $Q_{\mu,\mathrm{i}} > 10^6$. It is important to note that this is a conservative estimate since with a more optimal design, we can utilize an asymmetric optical cavity that minimally leaks optical light (leaking less than <1 %) into the microwave cavity. Hence, with a superconducting Nb cavity, we can expect microwave Q of $\sim 10^6$ at $\sim$ 6.5 K temperature, even when there is moderate optical light (< 100 mW). Compared with the current microwave Q of 1000, this is a significant improvement. Frequency tuning of these kinds of superconducting microwave cavities can be done using a dielectric rod, similar to the design in [78]. Additionally, combining a superconducting microwave cavity in our piezo-Brillouin platform can provide ways to independently characterize the electromechanical cooperativity through electromagnetically induced transparency (EIT) prior to the all-combined electro-optomechanical experiment.

Bibliography

[1] Braginsky, V. B., Vorontsov, Y. I. & Thorne, K. S. Quantum Nondemolition Measurements. *Science* **209**, 547–557 (1980). URL https://www.science.org/doi/10.1126/science.209.4456.547. Publisher: American Association for the Advancement of Science.

[2] Caves, C. M., Thorne, K. S., Drever, R. W. P., Sandberg, V. D. & Zimmermann, M. On the measurement of a weak classical force coupled to a quantum-mechanical oscillator. I. Issues of principle. *Reviews of Modern Physics* **52**, 341–392 (1980). URL https://link.aps.org/doi/10.1103/RevModPhys.52.341. Publisher: American Physical Society.

[3] Teufel, J. D. *et al.* Sideband cooling of micromechanical motion to the quantum ground state. *Nature* **475**, 359–363 (2011). URL https://www.nature.com/articles/nature10261. Number: 7356 Publisher: Nature Publishing Group.

[4] Chan, J. *et al.* Laser cooling of a nanomechanical oscillator into its quantum ground state. *Nature* **478**, 89–92 (2011). URL https://www.nature.com/articles/nature10461. Number: 7367 Publisher: Nature Publishing Group.

[5] O'Connell, A. D. *et al.* Quantum ground state and single-phonon control of a mechanical resonator. *Nature* **464**, 697–703 (2010). URL

https://www.nature.com/articles/nature08967. Number: 7289 Publisher: Nature Publishing Group.

[6] Chu, Y. & Gröblacher, S. A perspective on hybrid quantum opto- and electromechanical systems. *Applied Physics Letters* **117**, 150503 (2020). URL https://aip.scitation.org/doi/10.1063/5.0021088.

[7] Chu, Y. *et al.* Creation and control of multi-phonon Fock states in a bulk acoustic-wave resonator. *Nature* **563**, 666–670 (2018). URL https://www.nature.com/articles/s41586-018-0717-7.

[8] Satzinger, K. J. *et al.* Quantum control of surface acoustic-wave phonons. *Nature* **563**, 661–665 (2018). URL https://www.nature.com/articles/s41586-018-0719-5. Number: 7733 Publisher: Nature Publishing Group.

[9] Arrangoiz-Arriola, P. *et al.* Resolving the energy levels of a nanomechanical oscillator. *Nature* **571**, 537–540 (2019). URL https://www.nature.com/articles/s41586-019-1386-x. Number: 7766 Publisher: Nature Publishing Group.

[10] Wallucks, A., Marinković, I., Hensen, B., Stockill, R. & Gröblacher, S. A quantum memory at telecom wavelengths. *Nature Physics* **16**, 772–777 (2020). URL https://www.nature.com/articles/s41567-020-0891-z. Number: 7 Publisher: Nature Publishing Group.

[11] Hann, C. T. *et al.* Hardware-Efficient Quantum Random Access Memory with Hybrid Quantum Acoustic Systems. *Physical Review Letters* **123**, 250501 (2019). URL https://link.aps.org/doi/10.1103/PhysRevLett.123.250501. Publisher: American Physical Society.

[12] MacCabe, G. S. *et al.* Nano-acoustic resonator with ultra-long phonon lifetime. *Science* **370**, 840–843 (2020). URL https://www.science.org/doi/10.1126/science.abc7312.

[13] Beccari, A. *et al.* Strained crystalline nanomechanical resonators with quality factors above 10 billion. *Nature Physics* **18**, 436–441 (2022). URL https://www.nature.com/articles/s41567-021-01498-4.

[14] Zeuthen, E., Schliesser, A., Sørensen, A. S. & Taylor, J. M. Figures of merit for quantum transducers. *Quantum Science and Technology* **5**, 034009 (2020). URL https://doi.org/10.1088/2058-9565/ab8962.

[15] Andrews, R. W. *et al.* Bidirectional and efficient conversion between microwave and optical light. *Nature Physics* **10**, 321–326 (2014). URL https://www.nature.com/articles/nphys2911.

[16] Delaney, R. D. *et al.* Superconducting-qubit readout via low-backaction electro-optic transduction. *Nature* **606**, 489–493 (2022). URL https://www.nature.com/articles/s41586-022-04720-2.

[17] Brubaker, B. *et al.* Optomechanical Ground-State Cooling in a Continuous and Efficient Electro-Optic Transducer. *Physical Review X* **12**, 021062 (2022). URL https://link.aps.org/doi/10.1103/PhysRevX.12.021062. Publisher: American Physical Society.

[18] Vainsencher, A., Satzinger, K. J., Peairs, G. A. & Cleland, A. N. Bi-directional conversion between microwave and optical frequencies in a piezoelectric optomechanical device. *Applied Physics Letters* **109**, 033107 (2016). URL https://aip.scitation.org/doi/10.1063/1.4955408.

[19] Jiang, W. *et al.* Efficient bidirectional piezo-optomechanical transduction between microwave and optical frequency. *Nature Communications* **11**, 1166 (2020). URL https://www.nature.com/articles/s41467-020-14863-3.

[20] Mirhosseini, M., Sipahigil, A., Kalaee, M. & Painter, O. Superconducting qubit to optical photon transduction. *Nature* **588**, 599–603 (2020). URL https://www.nature.com/articles/s41586-020-3038-6.

[21] Shao, L. *et al.* Microwave-to-optical conversion using lithium niobate thin-film acoustic resonators. *Optica* **6**, 1498–1505 (2019). URL https://opg.optica.org/optica/abstract.cfm?uri=optica-6-12-1498.

[22] Han, X. *et al.* Cavity piezo-mechanics for superconducting-nanophotonic quantum interface. *Nature Communications* **11**, 3237 (2020). URL https://www.nature.com/articles/s41467-020-17053-3.

[23] Valle, S. & Balram, K. C. Cryogenic operation of MEMS-based suspended high overtone bulk acoustic wave resonators for microwave to optical signal transduction (2021). URL http://arxiv.org/abs/2109.11838.

[24] Han, X., Fu, W., Zou, C.-L., Jiang, L. & Tang, H. X. Microwave-optical quantum frequency conversion. *Optica* **8**, 1050–1064 (2021). URL https://opg.optica.org/optica/abstract.cfm?uri=optica-8-8-1050. Publisher: Optica Publishing Group.

[25] Lambert, N. J., Rueda, A., Sedlmeir, F. & Schwefel, H. G. L. Coherent Conversion Between Microwave and Optical Photons—An Overview of Physical Implementations. *Advanced Quantum Technologies* **3**, 1900077 (2020). URL https://onlinelibrary.wiley.com/doi/abs/10.1002/qute.201900077. _eprint: https://onlinelibrary.wiley.com/doi/pdf/10.1002/qute.201900077.

[26] Lauk, N. *et al.* Perspectives on quantum transduction. *Quantum Science and Technology* **5**, 020501 (2020). URL https://dx.doi.org/10.1088/2058-9565/ab788a. Publisher: IOP Publishing.

[27] Wollack, E. A. *et al.* Quantum state preparation and tomography of entangled mechanical resonators. *Nature* **604**, 463–467 (2022). URL https://www.nature.com/articles/s41586-022-04500-y. Number: 7906 Publisher: Nature Publishing Group.

[28] Andersson, G. *et al.* Squeezing and Multimode Entanglement of Surface Acoustic Wave Phonons. *PRX Quantum* **3**, 010312 (2022). URL https://link.aps.org/doi/10.1103/PRXQuantum.3.010312. Publisher: American Physical Society.

[29] Kervinen, M., Välimaa, A., Ramírez-Muñoz, J. E. & Sillanpää, M. A. Sideband Control of a Multimode Quantum Bulk Acoustic System. *Physical Review Applied* **14**, 054023 (2020). URL https://link.aps.org/doi/10.1103/PhysRevApplied.14.054023. Publisher: American Physical Society.

[30] von Lüpke, U. *et al.* Parity measurement in the strong dispersive regime of circuit quantum acoustodynamics. *Nature Physics* **18**, 794–799 (2022). URL https://www.nature.com/articles/s41567-022-01591-2. Number: 7 Publisher: Nature Publishing Group.

[31] Chu, Y. *et al.* Quantum acoustics with superconducting qubits. *Science* **358**, 199–202 (2017). URL https://www.science.org/doi/10.1126/science.aao1511.

[32] Scigliuzzo, M. *et al.* Phononic loss in superconducting resonators on piezoelectric substrates. *New Journal of Physics* **22**, 053027 (2020). URL https://doi.org/10.1088/1367-2630/ab8044.

[33] Jain, V. *et al.* Acoustic radiation from a superconducting qubit: From spontaneous emission to Rabi oscillations (2022). URL http://arxiv.org/abs/2211.07475. ArXiv:2211.07475 [cond-mat, physics:quant-ph].

[34] Georgescu, A. B. & Ismail-Beigi, S. Surface Piezoelectricity of (0001) Sapphire. *Physical Review Applied* **11**, 064065 (2019). URL https://link.aps.org/doi/10.1103/PhysRevApplied.11.064065.

[35] Aktas, O. *et al.* Piezoelectricity in nominally centrosymmetric phases. *Physical Review Research* **3**, 043221 (2021). URL https://link.aps.org/doi/10.1103/PhysRevResearch.3.043221.

[36] Robinson, W. H., Glover, A. J. & Wolfenden, A. Electrical-mechanical coupling of dislocations in KCl, NaCl, LiF, and CaF2. *physica status solidi (a)* **48**, 155–163 (1978). URL https://onlinelibrary.wiley.com/doi/abs/10.1002/pssa.2210480120.

[37] Sharma, N. D., Maranganti, R. & Sharma, P. On the possibility of piezoelectric nanocomposites without using piezoelectric materials. *Journal of the Mechanics and Physics of Solids* **55**, 2328–2350 (2007). URL https://www.sciencedirect.com/science/article/pii/S0022509607000816.

[38] Ioffe, L. B., Geshkenbein, V. B., Helm, C. & Blatter, G. Decoherence in Superconducting Quantum Bits by Phonon Radiation. *Physical Review Letters* **93**, 057001 (2004). URL https://link.aps.org/doi/10.1103/PhysRevLett.93.057001.

[39] Diniz, I. & de Sousa, R. Intrinsic Photon Loss at the Interface of Superconducting Devices. *Physical Review Letters* **125**, 147702 (2020). URL https://link.aps.org/doi/10.1103/PhysRevLett.125.147702.

[40] Braginsky, V. B., Manukin, A. B. & Keiser, G. M. Measurement of Weak Forces in Physics Experiments. *American Journal of Physics* **46**, 195–196 (1978). URL https://aapt.scitation.org/doi/abs/10.1119/1.11161. Publisher: American Association of Physics Teachers.

[41] Jensen, K., Kim, K. & Zettl, A. An atomic-resolution nanomechanical mass sensor. *Nature Nanotechnology* **3**, 533–537 (2008). URL https://www.nature.com/articles/nnano.2008.200. Number: 9 Publisher: Nature Publishing Group.

[42] Rugar, D., Budakian, R., Mamin, H. J. & Chui, B. W. Single spin detection by magnetic resonance force microscopy. *Nature* **430**, 329–332 (2004). URL https://www.nature.com/articles/nature02658. Number: 6997 Publisher: Nature Publishing Group.

[43] Brillouin, L. Scattering of light rays in a transparent homogeneous body: influence of thermal agitation. *Annales de Physique* **9**, 88–122 (1922). URL https://www.annphys.org/articles/anphys/abs/1922/17/anphys19220917p88/anphys1
Number: 17 Publisher: EDP Sciences.

[44] Maiman, T. H. Stimulated Optical Radiation in Ruby. *Nature* **187**, 493–494 (1960). URL https://www.nature.com/articles/187493a0. Number: 4736 Publisher: Nature Publishing Group.

[45] Otterstrom, N. T. *et al.* Resonantly enhanced nonreciprocal silicon Brillouin amplifier. *Optica* **6**, 1117–1123 (2019). URL

https://opg.optica.org/optica/abstract.cfm?uri=optica-6-9-1117. Publisher: Optica Publishing Group.

[46] Otterstrom, N. T., Behunin, R. O., Kittlaus, E. A., Wang, Z. & Rakich, P. T. A silicon Brillouin laser. *Science* **360**, 1113–1116 (2018). URL https://www.science.org/doi/10.1126/science.aar6113. Publisher: American Association for the Advancement of Science.

[47] Gross, E. Change of Wave-length of Light due to Elastic Heat Waves at Scattering in Liquids. *Nature* **126**, 201–202 (1930). URL https://www.nature.com/articles/126201a0. Number: 3171 Publisher: Nature Publishing Group.

[48] Brewer, R. G. & Rieckhoff, K. E. Stimulated Brillouin Scattering in Liquids. *Physical Review Letters* **13**, 334–336 (1964). URL https://link.aps.org/doi/10.1103/PhysRevLett.13.334. Publisher: American Physical Society.

[49] Hagenlocker, E. E. & Rado, W. G. Stimulated Brillouin and Raman scattering in gases. *Applied Physics Letters* **7**, 236–238 (1965). URL https://aip.scitation.org/doi/10.1063/1.1754395. Publisher: American Institute of Physics.

[50] Chiao, R. Y., Townes, C. H. & Stoicheff, B. P. Stimulated Brillouin Scattering and Coherent Generation of Intense Hypersonic Waves. *Physical Review Letters* **12**, 592–595 (1964). URL https://link.aps.org/doi/10.1103/PhysRevLett.12.592. Publisher: American Physical Society.

[51] Ippen, E. & Stolen, R. Stimulated Brillouin scattering in optical fibers. *Applied Physics Letters* **21**, 539–541 (1972). URL

https://aip.scitation.org/doi/10.1063/1.1654249. Publisher: American Institute of Physics.

[52] Renninger, W. H., Kharel, P., Behunin, R. O. & Rakich, P. T. Bulk crystalline optomechanics. *Nature Physics* **14**, 601–607 (2018). URL https://www.nature.com/articles/s41567-018-0090-3.

[53] Kharel, P. *et al.* Ultra-high-Q phononic resonators on-chip at cryogenic temperatures. *APL Photonics* **3**, 066101 (2018). URL https://aip.scitation.org/doi/10.1063/1.5026798.

[54] Kharel, P. *et al.* High-frequency cavity optomechanics using bulk acoustic phonons. *Science Advances* **5**, eaav0582 (2019). URL https://www.science.org/doi/10.1126/sciadv.aav0582.

[55] Kharel, P. *et al.* Multimode Strong Coupling in Cavity Optomechanics. *Physical Review Applied* **18**, 024054 (2022). URL https://link.aps.org/doi/10.1103/PhysRevApplied.18.024054. Publisher: American Physical Society.

[56] Galliou, S. *et al.* Extremely Low Loss Phonon-Trapping Cryogenic Acoustic Cavities for Future Physical Experiments. *Scientific Reports* **3**, 2132 (2013). URL https://www.nature.com/articles/srep02132.

[57] Yoon, T. *et al.* Simultaneous Brillouin and piezoelectric coupling to a high-frequency bulk acoustic resonator. *Optica* **10**, 110–117 (2023). URL https://opg.optica.org/optica/abstract.cfm?uri=optica-10-1-110. Publisher: Optica Publishing Group.

[58] Strutt, R. J. Scattering of light by solid substances. *Proceedings of the Royal Society of London. Series A, Containing Papers*

of a Mathematical and Physical Character **95**, 476–479 (1919). URL https://royalsocietypublishing.org/doi/abs/10.1098/rspa.1919.0024. Publisher: Royal Society.

[59] Larmor, J. The Doppler Effect in the Molecular Scattering of Radiation. *Nature* **103**, 165–166 (1919). URL https://www.nature.com/articles/103165c0. Number: 2583 Publisher: Nature Publishing Group.

[60] Raman, C. V. The Doppler Effect in the Molecular Scattering of Radiation. *Nature* **103**, 165–165 (1919). URL https://www.nature.com/articles/103165b0. Number: 2583 Publisher: Nature Publishing Group.

[61] Mandelstam, L. Light scattering by inhomogeneous media. *Zh. Russ. Fiz-Khim. Ova* **58**, 146 (1926).

[62] Smith, R. G. Optical Power Handling Capacity of Low Loss Optical Fibers as Determined by Stimulated Raman and Brillouin Scattering. *Applied Optics* **11**, 2489–2494 (1972). URL https://opg.optica.org/ao/abstract.cfm?uri=ao-11-11-2489. Publisher: Optica Publishing Group.

[63] Aoki, Y., Tajima, K. & Mito, I. Input power limits of single-mode optical fibers due to stimulated Brillouin scattering in optical communication systems. *Journal of Lightwave Technology* **6**, 710–719 (1988). Conference Name: Journal of Lightwave Technology.

[64] Tei, K. & Yamaguchi, S. Suppression of stimulated Brillouin scattering in optical fibers using a stepwise optical frequency pulse train. *Optics Express* **28**, 17793–17800 (2020). URL

https://opg.optica.org/oe/abstract.cfm?uri=oe-28-12-17793. Publisher: Optica Publishing Group.

[65] White, J. O. *et al.* Suppression of stimulated Brillouin scattering in optical fibers using a linearly chirped diode laser. *Optics Express* **20**, 15872–15881 (2012). URL https://opg.optica.org/oe/abstract.cfm?uri=oe-20-14-15872. Publisher: Optica Publishing Group.

[66] Eggleton, B. J., Poulton, C. G., Rakich, P. T., Steel, M. J. & Bahl, G. Brillouin integrated photonics. *Nature Photonics* **13**, 664–677 (2019). URL https://www.nature.com/articles/s41566-019-0498-z. Number: 10 Publisher: Nature Publishing Group.

[67] Gertler, S. *et al.* Narrowband microwave-photonic notch filters using Brillouin-based signal transduction in silicon. *Nature Communications* **13**, 1947 (2022). URL https://www.nature.com/articles/s41467-022-29590-0. Number: 1 Publisher: Nature Publishing Group.

[68] Zhou, Y. *et al.* Intermodal strong coupling and wideband, low-loss isolation in silicon (2022). URL http://arxiv.org/abs/2211.05864. ArXiv:2211.05864 [physics].

[69] Garmire, E. Perspectives on stimulated Brillouin scattering. *New Journal of Physics* **19**, 011003 (2017). URL https://doi.org/10.1088/1367-2630/aa5447. Publisher: IOP Publishing.

[70] Bai, Z. *et al.* Stimulated Brillouin scattering materials, experimental design and applications: A review. *Optical Materials* **75**, 626–645 (2018). URL https://www.sciencedirect.com/science/article/pii/S0925346717306687.

[71] Aspelmeyer, M., Kippenberg, T. J. & Marquardt, F. Cavity optomechanics. *Reviews of Modern Physics* **86**, 1391–1452 (2014). URL https://link.aps.org/doi/10.1103/RevModPhys.86.1391.

[72] Weis, S. *et al.* Optomechanically Induced Transparency. *Science* **330**, 1520–1523 (2010). URL https://www.science.org/doi/10.1126/science.1195596.

[73] Kharel, P., Behunin, R. O., Renninger, W. H. & Rakich, P. T. Noise and dynamics in forward Brillouin interactions. *Physical Review A* **93**, 063806 (2016). URL https://link.aps.org/doi/10.1103/PhysRevA.93.063806. Publisher: American Physical Society.

[74] Sipe, J. E. & Steel, M. J. A Hamiltonian treatment of stimulated Brillouin scattering in nanoscale integrated waveguides. *New Journal of Physics* **18**, 045004 (2016). URL https://dx.doi.org/10.1088/1367-2630/18/4/045004. Publisher: IOP Publishing.

[75] Paik, H. *et al.* Observation of High Coherence in Josephson Junction Qubits Measured in a Three-Dimensional Circuit QED Architecture. *Physical Review Letters* **107**, 240501 (2011). URL https://link.aps.org/doi/10.1103/PhysRevLett.107.240501. Publisher: American Physical Society.

[76] Reagor, M. *et al.* Quantum memory with millisecond coherence in circuit QED. *Physical Review B* **94**, 014506 (2016). URL https://link.aps.org/doi/10.1103/PhysRevB.94.014506.

[77] Reagor, M. *et al.* Reaching 10 ms single photon lifetimes for superconducting aluminum cavities. *Applied Physics Letters* **102**, 192604 (2013). URL https://aip.scitation.org/doi/full/10.1063/1.4807015.

[78] Read, A. P. *et al.* Precision measurement of the microwave dielectric loss of sapphire in the quantum regime with parts-per-billion sensitivity (2022). URL http://arxiv.org/abs/2206.14334. ArXiv:2206.14334 [cond-mat, physics:quant-ph].

[79] Place, A. P. M. *et al.* New material platform for superconducting transmon qubits with coherence times exceeding 0.3 milliseconds. *Nature Communications* **12**, 1779 (2021). URL https://www.nature.com/articles/s41467-021-22030-5. Number: 1 Publisher: Nature Publishing Group.

[80] Bushev, P. *et al.* Testing the generalized uncertainty principle with macroscopic mechanical oscillators and pendulums. *Physical Review D* **100**, 066020 (2019). URL https://link.aps.org/doi/10.1103/PhysRevD.100.066020. Publisher: American Physical Society.

[81] Lo, A. *et al.* Acoustic Tests of Lorentz Symmetry Using Quartz Oscillators. *Physical Review X* **6**, 011018 (2016). URL https://link.aps.org/doi/10.1103/PhysRevX.6.011018. Publisher: American Physical Society.

[82] Kurizki, G. *et al.* Quantum technologies with hybrid systems. *Proceedings of the National Academy of Sciences* **112**, 3866–3873 (2015). URL https://www.pnas.org/doi/10.1073/pnas.1419326112.

[83] Verhagen, E., Deléglise, S., Weis, S., Schliesser, A. & Kippenberg, T. J. Quantum-coherent coupling of a mechanical oscillator to an optical cavity mode. *Nature* **482**, 63–67 (2012). URL https://www.nature.com/articles/nature10787.

[84] Maity, S. *et al.* Coherent acoustic control of a single silicon vacancy spin in diamond. *Nature Communications* **11**, 193 (2020). URL https://www.nature.com/articles/s41467-019-13822-x.

[85] Whiteley, S. J. *et al.* Spin–phonon interactions in silicon carbide addressed by Gaussian acoustics. *Nature Physics* **15**, 490–495 (2019). URL https://www.nature.com/articles/s41567-019-0420-0.

[86] Liekens, W., Michiels, L. & Bock, A. d. On the attenuation of 9.4 GHz longitudinal hypersonic waves in some trigonal crystals. *Journal of Physics C: Solid State Physics* **4**, 1124–1129 (1971). URL https://doi.org/10.1088/0022-3719/4/10/021.

[87] Thaxter, J. & Tannenwald, P. Phonon Generation, Propagation, and Attenuation at 70 GHz. *IEEE Transactions on Sonics and Ultrasonics* **13**, 61–68 (1966).

[88] Cleland, A. N. Properties of the Phonon Gas. In Cleland, A. N. (ed.) *Foundations of Nanomechanics: From Solid-State Theory to Device Applications*, Advanced Texts in Physics, 87–144 (Springer, Berlin, Heidelberg, 2003). URL https://doi.org/10.1007/978-3-662-05287-7_3.

[89] Hwang, E. & Bhave, S. A. Experimental verification of internal friction at GHZ frequencies in doped single-crystal silicon. In *2011 IEEE 24th International Conference on Micro Electro Mechanical Systems*, 424–427 (2011). ISSN: 1084-6999.

[90] Nowick, A. S. & Berry, B. S. *Anelastic Relaxation in Crystalline Solids* (Academic Press, 1972). Google-Books-ID: bUtRAAAAMAAJ.

[91] Zener, C. *Elasticity and Anelasticity of Metals* (University of Chicago Press, 1948). Google-Books-ID: FKcZAAAAIAAJ.

[92] Mason, W. P. 6 - Effect of Impurities and Phonon Processes on the Ultrasonic Attenuation of Germanium, Crystal Quartz, and Silicon. In Mason, W. P. (ed.) *Physical Acoustics*, vol. 3 of *Lattice Dynamics*, 235–286 (Academic Press, 1965). URL https://www.sciencedirect.com/science/article/pii/B9780123956699500138.

[93] Chester, M. Second Sound in Solids. *Physical Review* **131**, 2013–2015 (1963). URL https://link.aps.org/doi/10.1103/PhysRev.131.2013.

[94] Klemens, P. G. Decay of High-Frequency Longitudinal Phonons. *Journal of Applied Physics* **38**, 4573–4576 (1967). URL https://aip.scitation.org/doi/10.1063/1.1709187. Publisher: American Institute of Physics.

[95] Behunin, R. O. *et al.* Long-lived guided phonons in fiber by manipulating two-level systems (2016). URL http://arxiv.org/abs/1501.04248. ArXiv:1501.04248 [quant-ph].

[96] Phillips, W. A. Two-level states in glasses. *Reports on Progress in Physics* **50**, 1657 (1987). URL https://dx.doi.org/10.1088/0034-4885/50/12/003.

[97] Arcizet, O., Rivière, R., Schliesser, A., Anetsberger, G. & Kippenberg, T. J. Cryogenic properties of optomechanical silica microcavities. *Physical Review A* **80**, 021803 (2009). URL https://link.aps.org/doi/10.1103/PhysRevA.80.021803. Publisher: American Physical Society.

[98] Galliou, S. *et al.* A new method of probing mechanical losses of coatings at cryogenic temperatures. *Review of Scientific Instruments* **87**, 123906 (2016). URL https://aip.scitation.org/doi/full/10.1063/1.4972106. Publisher: American Institute of Physics.

[99] Yamamoto, K. *et al.* Measurement of the mechanical loss of a cooled reflective coating for gravitational wave detection. *Physical Review D* **74**, 022002 (2006). URL https://link.aps.org/doi/10.1103/PhysRevD.74.022002. Publisher: American Physical Society.

[100] Berry, B. S. & Pritchet, W. C. DEFECT STUDIES OF THIN LAYERS BY THE VIBRATING-REED TECHNIQUE. *Le Journal de Physique Colloques* **42**, C5–1122 (1981). URL http://dx.doi.org/10.1051/jphyscol:19815172. Publisher: EDP Sciences.

[101] Jin, N. *et al.* Micro-fabricated mirrors with finesse exceeding one million. *Optica* **9**, 965–970 (2022). URL https://opg.optica.org/optica/abstract.cfm?uri=optica-9-9-965. Publisher: Optica Publishing Group.

[102] Bismayer, U., Brinksmeier, E., Güttler, B., Seibt, H. & Menz, C. Measurement of subsurface damage in silicon wafers. *Precision Engineering* **16**, 139–144 (1994). URL https://www.sciencedirect.com/science/article/pii/0141635994901996.

[103] Martirosyan, V., Despiau-Pujo, E., Dubois, J., Cunge, G. & Joubert, O. Helium plasma modification of Si and Si3N4 thin films for advanced etch processes. *Journal of Vacuum Science & Technology A* **36**, 041301 (2018). URL https://avs.scitation.org/doi/full/10.1116/1.5025152. Publisher: American Vacuum Society.

[104] Humbird, D., Graves, D. B., Stevens, A. a. E. & Kessels, W. M. M. Molecular dynamics simulations of Ar+ bombardment of Si with comparison to experiment. *Journal of Vacuum Science & Technology A* **25**, 1529–1533 (2007). URL

https://avs.scitation.org/doi/10.1116/1.2787713. Publisher: American Vacuum Society.

[105] Stevens, A. a. E., Kessels, W. M. M., van de Sanden, M. C. M. & Beijerinck, H. C. W. Amorphous silicon layer characteristics during 70–2000eV Ar+-ion bombardment of Si(100). *Journal of Vacuum Science & Technology A* **24**, 1933–1940 (2006). URL https://avs.scitation.org/doi/10.1116/1.2244535. Publisher: American Vacuum Society.

[106] Chan, A. C. T. & Wang, G. C. Roughness evolution of Si(111) by low-energy ion bombardment. *Surface Science* **414**, 17–25 (1998). URL https://www.sciencedirect.com/science/article/pii/S0039602898004257.

[107] Koster, M. & Urbassek, H. M. Damage production in a-Si under low-energy self-atom bombardment. *Journal of Applied Physics* **90**, 689–695 (2001). URL https://aip.scitation.org/doi/10.1063/1.1380408. Publisher: American Institute of Physics.

[108] Ludwig, F., Eddy, C. R., Malis, O. & Headrick, R. L. Si(100) surface morphology evolution during normal-incidence sputtering with 100–500 eV Ar+ ions. *Applied Physics Letters* **81**, 2770–2772 (2002). URL https://aip.scitation.org/doi/10.1063/1.1513655. Publisher: American Institute of Physics.

[109] Cerofolini, G. F. *et al.* Hydrogen and helium bubbles in silicon. *Materials Science and Engineering: R: Reports* **27**, 1–52 (2000). URL https://www.sciencedirect.com/science/article/pii/S0927796X00000073.

[110] Borselli, M., Johnson, T. J. & Painter, O. Measuring the role of surface chemistry in silicon microphotonics. *Applied Physics Letters* **88**, 131114

(2006). URL https://aip.scitation.org/doi/full/10.1063/1.2191475. Publisher: American Institute of Physics.

[111] Schnabel, R., Mavalvala, N., McClelland, D. E. & Lam, P. K. Quantum metrology for gravitational wave astronomy. *Nature Communications* **1**, 121 (2010). URL https://www.nature.com/articles/ncomms1122. Number: 1 Publisher: Nature Publishing Group.

[112] Schreppler, S. *et al.* Optically measuring force near the standard quantum limit. *Science* **344**, 1486–1489 (2014). URL https://www.science.org/doi/10.1126/science.1249850. Publisher: American Association for the Advancement of Science.

[113] Hong, S. *et al.* Hanbury Brown and Twiss interferometry of single phonons from an optomechanical resonator. *Science* **358**, 203–206 (2017). URL https://www.science.org/doi/10.1126/science.aan7939. Publisher: American Association for the Advancement of Science.

[114] Wollman, E. E. *et al.* Quantum squeezing of motion in a mechanical resonator. *Science* **349**, 952–955 (2015). URL https://www.science.org/doi/10.1126/science.aac5138. Publisher: American Association for the Advancement of Science.

[115] Riedinger, R. *et al.* Remote quantum entanglement between two micromechanical oscillators. *Nature* **556**, 473–477 (2018). URL https://www.nature.com/articles/s41586-018-0036-z. Number: 7702 Publisher: Nature Publishing Group.

[116] Van Laer, R., Baets, R. & Van Thourhout, D. Unifying Brillouin scattering and cavity optomechanics. *Physical Review A* **93**, 053828 (2016). URL https://link.aps.org/doi/10.1103/PhysRevA.93.053828.

[117] Tarumi, R., Nakamura, K., Ogi, H. & Hirao, M. Complete set of elastic and piezoelectric coefficients of α-quartz at low temperatures. *Journal of Applied Physics* **102**, 113508 (2007). URL https://aip.scitation.org/doi/10.1063/1.2816252.

[118] Labuda, A. & Proksch, R. Quantitative measurements of electromechanical response with a combined optical beam and interferometric atomic force microscope. *Applied Physics Letters* **106**, 253103 (2015). URL https://aip.scitation.org/doi/10.1063/1.4922210.

[119] Collins, L., Liu, Y., Ovchinnikova, O. S. & Proksch, R. Quantitative Electromechanical Atomic Force Microscopy. *ACS Nano* **13**, 8055–8066 (2019). URL https://doi.org/10.1021/acsnano.9b02883.

[120] Maze, J. R. *et al.* Properties of nitrogen-vacancy centers in diamond: the group theoretic approach. *New Journal of Physics* **13**, 025025 (2011). URL https://doi.org/10.1088/1367-2630/13/2/025025.

[121] Kelley, K. P. *et al.* Thickness and strain dependence of piezoelectric coefficient in ${\textbackslashmathrm{BaTiO}}_{3}$ thin films. *Physical Review Materials* **4**, 024407 (2020). URL https://link.aps.org/doi/10.1103/PhysRevMaterials.4.024407.

[122] Blésin, T., Tian, H., Bhave, S. A. & Kippenberg, T. J. Quantum coherent microwave-optical transduction using high-overtone bulk acoustic resonances. *Physical Review A* **104**, 052601 (2021). URL https://link.aps.org/doi/10.1103/PhysRevA.104.052601.

[123] Balram, K. C., Davanço, M. I., Song, J. D. & Srinivasan, K. Coherent coupling between radiofrequency, optical and acoustic waves in piezo-

optomechanical circuits. *Nature Photonics* **10**, 346–352 (2016). URL https://www.nature.com/articles/nphoton.2016.46.

[124] Forsch, M. *et al.* Microwave-to-optics conversion using a mechanical oscillator in its quantum ground state. *Nature Physics* **16**, 69–74 (2020). URL https://www.nature.com/articles/s41567-019-0673-7.

[125] Ivanov, V. Direct electro-optic effect in langasites and α-quartz. *Optical Materials* **79**, 1–7 (2018). URL https://www.sciencedirect.com/science/article/pii/S0925346718301435.

[126] Ilchenko, V. S., Savchenkov, A. A., Matsko, A. B. & Maleki, L. Whispering-gallery-mode electro-optic modulator and photonic microwave receiver. *JOSA B* **20**, 333–342 (2003). URL https://opg.optica.org/josab/abstract.cfm?uri=josab-20-2-333.

[127] Rueda, A. *et al.* Efficient microwave to optical photon conversion: an electro-optical realization. *Optica* **3**, 597–604 (2016). URL https://opg.optica.org/optica/abstract.cfm?uri=optica-3-6-597.

[128] Holzgrafe, J. *et al.* Cavity electro-optics in thin-film lithium niobate for efficient microwave-to-optical transduction. *Optica* **7**, 1714–1720 (2020). URL https://opg.optica.org/optica/abstract.cfm?uri=optica-7-12-1714.

[129] McKenna, T. P. *et al.* Cryogenic microwave-to-optical conversion using a triply resonant lithium-niobate-on-sapphire transducer. *Optica* **7**, 1737–1745 (2020). URL https://opg.optica.org/optica/abstract.cfm?uri=optica-7-12-1737.

[130] Hease, W. *et al.* Bidirectional Electro-Optic Wavelength Conversion in the Quantum Ground State. *PRX Quantum* **1**, 020315 (2020). URL https://link.aps.org/doi/10.1103/PRXQuantum.1.020315.

[131] Diamond, S. *et al.* Distinguishing parity-switching mechanisms in a superconducting qubit (2022). URL `http://arxiv.org/abs/2204.07458`. ArXiv:2204.07458 [cond-mat, physics:quant-ph].

[132] Oriani, A. E. *Multimodal and Ultra High-Q Superconducting Niobium Cavities for Circuit Quantum Electrodynamics*. Ph.D. thesis, The University of Chicago.